

ESTIMATING THE THERMAL PROPERTIES
OF THIN FILM AND MULTILAYER STRUCTURES
USING PHOTOTHERMAL DEFLECTION SPECTROSCOPY

A Dissertation

Presented to the Faculty of the Graduate School

of Cornell University

in Partial Fulfillment of the Requirements for the Degree of

Doctor of Philosophy

by

Michael Shannon Moorhead

January 2009

© 2009 Michael Shannon Moorhead

ESTIMATING THE THERMAL PROPERTIES OF THIN FILM AND
MULTILAYER STRUCTURES USING PHOTOTHERMAL DEFLECTION
SPECTROSCOPY

Michael Shannon Moorhead, Ph.D.

Cornell University 2009

Photothermal deflection spectroscopy (PDS) is an experimental technique which may be used to determine the thermal properties of materials. An intensity modulated heating laser is used to generate periodic thermal waves in the material and the surrounding gas phase. A probe laser is passed through the gas phase above the material and experiences periodic deflections due to the temperature dependence of the refractive index. This is commonly referred to as the mirage effect.

We have developed a model which allows for the calculation of the thermal field in a multilayer structure resulting from periodic laser heating. The model incorporates the effects of anisotropic thermal conductivity, interlayer thermal contact resistance, and volumetric optical-to-thermal energy conversion. The resulting temperature field is used to calculate the optical probe beam deflections.

A maximum *a posteriori* parameter estimation algorithm has been developed which allows for the determination of model parameters from experimental PDS measurements. This algorithm has the capability of accounting for *a priori* parameter information in the event that it may be known from prior measurements. Special attention is paid to the cases where the model may be insensitive to certain parameters or where linear combinations of parameters may exist.

Experiments were performed on bulk NIST standard references materials, including electrolytic iron (SRM8421) and stainless steel (SRM1462). The thermal conductivity of these materials was recovered from the estimation algorithm to within

a reasonable accuracy. This data was also used to extract the thermal conductivity of a “virtual film” atop the otherwise bulk material. We determined that for virtual film thicknesses larger than the thermal penetration depth, the algorithm was successfully able to determine the thermal conductivity. For thicknesses significantly less than the thermal penetration depth, however, the algorithm loses sensitivity to the properties of the film.

Experiments were also performed on a series of W/B₄C multilayer materials used as X-ray monochromator mirrors at Cornell’s High Energy Synchrotron Source (CHESS). Although we were unable to resolve the thermal properties of the individual layers, the effective thermal conductivity of the multilayer was found to be significantly less than either of its constituent bulk materials. We also found that there is a lack of sensitivity to the degree of anisotropy within the multilayer, thus we are only able to quote a cross-plane value for thermal conductivity.

BIOGRAPHICAL SKETCH

Michael Shannon Moorhead was born May 28, 1975 in Canandaigua, NY to Robert and Kathy Moorhead (née Davis). The first twelve years of his life were spent in Lima, NY, where he attended the Honeoye Falls-Lima Central School District. In 1987, his family moved to Herkimer, NY, where Michael graduated valedictorian of Herkimer High School in 1993.

Michael attended the Rochester Institute of Technology (RIT) in Rochester, NY to pursue his B.S. and M.S. degrees in Mechanical Engineering. It was there that he met his future wife, Alisha Shaw, of Farmington, NY. At RIT, Michael was advised by Dr. Satish Kandlikar on a jet impingement boiling heat transfer project, which became the subject of his M.S. thesis. Michael also held co-op appointments at General Electric Power Systems in Schenectady, NY, the Carrier Corporation in Syracuse, NY, and at the Center for Integrated Manufacturing Studies (CIMS) at RIT in Rochester, NY. Michael received highest honors for his B.S. and M.S. degrees, with a concentration in Aerospace Engineering and liberal arts minor in Psychology.

In March 1999, Michael and Alisha moved to Alexandria, VA to work for the Institute for Defense Analyses (IDA). At IDA, Michael worked on a variety of defense related projects, including radar systems, microelectromechanical systems (MEMS), unmanned aerial vehicles (UAVs), and future warfighting simulations.

Michael and Alisha were engaged in December 1998 and married in November 1999. Alisha gave birth to Kaitlyn Marie Moorhead on March 30, 2000 in Alexandria, VA. After leaving IDA in 2001, Michael attended Cornell University in Ithaca, NY to pursue a Ph.D. in Aerospace Engineering. While at Cornell, Alisha gave birth to their second child, Conor Alan Moorhead, on March 24, 2006.

Michael was appointed Assistant Professor of Mechanical Engineering at the Rose-Hulman Institute of Technology in Terre Haute, IN in 2007. He is looking forward to a long and fruitful career in education and hopes to be an inspiration to generations of future students.

*This work is dedicated to my wife and children, without whom I would not have made
it through the hard times*

ACKNOWLEDGEMENTS

I owe a debt of gratitude to all those in the world who have loved me, inspired me, encouraged me, and pushed me through life. I would like to thank the following by name, but there are countless many who equally deserve to be named here. Thank you all!

- My wife, Alisha
- My children, Kaitlyn and Conor
- My parents, Robert and Kathy Moorhead
- My sister, Kari Lynn Moorhead
- My 188 Grumman lab mates and comrades in arms
 - Junho Bae
 - Jason Foley
 - Erik Martens
 - Sungryel Choi
 - Jens Notholt
- My fellow graduate students in MAE, particularly
 - Shan Mohiuddin
 - Armann Gylfason
 - Sathyanaryana Ayallasomyajula
 - Darren Zanon
 - Brett Streetman
 - Veronica Santos
 - Jennifer Edwards
 - Sandra Sattler

- The faculty and staff of MAE, particularly
 - Karen Biesecker
 - Marcia Sawyer
 - Beverly Gedvillas
 - Judy Thoroughman
- My past advisors
 - Prof. Satish Kandlikar (RIT)
 - Prof. Kevin Kochersberger (RIT)
- The members of my committee
 - Prof. C. Thomas Avedisian (chair)
 - Prof. Michel Louge
 - Prof. Nicholas Zabaras
 - Prof. Joel Brock
- Collaborators
 - Alexander Kazimirov (CHESS)
 - Joe Hodges (NIST)
- The teachers who taught me what it meant to teach, particularly
 - Margaret Trefzger (HHS)
 - Lois Miller (HHS)
 - Robert Kaplan (HHS)
 - Prof. Thomas Upson (RIT)
 - Prof. Satish Kandlikar (RIT)
 - Prof. Frank Moore (Cornell)
- Those who helped more than they should have
 - John Sinnott (CCMR)
 - Matt Ulinski (MAE)

- Rick Schmidt (MAE)
- John Orak (MAE)
- The faculty and staff of the Rose-Hulman Institute of Technology
- The staff of the Cornell NanoScale Science and Technology Facility (CNF)
- The American Society for Engineering Education (ASEE) for my National Defense Science & Engineering Graduate (NDSEG) Fellowship

TABLE OF CONTENTS

Biographical Sketch	iii
Dedication	v
Acknowledgements	vi
Table of Contents	ix
List of Figures	xii
List of Tables	xiv
Chapter One: Modeling the temperature field and optical probe beam deflections of a periodically heated multilayer structure	1
Abstract	2
1. Introduction	3
2. Model	7
1.1. Thermal Field	9
1.2. Probe Beam Deflections	13
3. Model Validation	16
3.1. Introduction	16
3.2. Experimental Apparatus	17
3.3. Validation Results	23
3.3.1. Bulk	23
3.3.2. Film on Substrate	24
4. Parametric Investigation	38
5. Summary & Conclusions	50
References	54
Chapter Two: A maximum a posteriori non-linear least squares estimation algorithm for the determination of thermal properties using PDS	59

Appendix I: Photographs of Experimental Apparatus	164
Appendix J: Computer Codes	169

LIST OF FIGURES

1-1: Schematic of transverse PDS	4
1-2: Schematic of multilayer structure	6
1-3: Schematics of probe beam	8
1-4: Schematic of experimental apparatus	18
1-5: Comparison of measurements and model SRM8421	27
1-6: Comparison of measurements and model SRM1462	31
1-7: Virtual film analysis	35
1-8: Sensitivity of probe beam deflections to virtual film thickness	37
1-9: Effect of modulation frequency	40
1-10: Effect of heating beam radius	43
1-11: Effect of anisotropy	45
1-12 : Effect of contact resistance	47
1-13: Temperature field in multilayer stack	51
1-14: Effect of probe beam parameters	52
2-1: Schematic of transverse PDS	62
2-2: Flow chart of estimation algorithm	64
2-3: Phase-nulling operation	75
2-4: Pre phase-nulling at several frequencies	75
2-5: Post phase-nulling at several frequencies	76
2-6: Thermal penetration depth dependence on frequency	78
2-7: Multi-layer film on substrate model	79
2-8: Normalized relative uncertainty	85
2-9: Elements of correlation matrix	85

2-10: Estimation results – cross-plane thermal conductivity	91
2-11: Estimation results – contact resistance	92
2-12: Estimation results – anisotropy	92
2-13: Estimation results – cost function	93
2-14: Estimation results – equivalent resistance	93
2-15: Normalized uncertainty – cross-plane thermal conductivity	100
2-16: Normalized uncertainty – contact resistance	100
2-17: Normalized uncertainty – anisotropy	101
2-18: Cross correlation – thermal conductivity and contact resistance	101
3-1: Equivalent film representation of a film on substrate	112
3-2: Probe beam deflections – sample 2	121
3-3: Probe beam deflections – sample 3	122
3-4: Probe beam deflections – sample 4	123
3-5: Probe beam deflections – Sample 5	124
3-6: Estimation results – cross-plane thermal conductivity	127
3-7: Estimation results – equivalent resistance	128
3-8: Estimation results – thermal diffusivity	129

LIST OF TABLES

1-1: Boundary conditions	10
1-2: Comparison of model parameters and results	26
1-3: Default material properties	39
1-4: Default model parameters	39
2-1: Bulk properties	81
2-2: Relative thermal penetration depth	81
2-3: Normalized relative uncertainty for multi-frequency validation	83
2-4: Correlation matrix for $f = 2.656$ kHz	83
2-5: Correlation matrix for $f = 26.56$ MHz	83
2-6: Correlation matrix for multi-frequency	83
2-7: Eigenvalues and eigenvectors for scaled correlation matrix	86
2-8: Conditions for varying anisotropy ratio and contact resistance	90
2-9: Truth-model – parameter estimates and uncertainty	94
2-10: Truth-model – correlation matrix	96
3-1: W/B4C multilayer specifications	110
3-2: Bulk properties	111
3-3: Equivalent bulk properties of multilayer sample	111
3-4: Summary of fixed and variable parameters	114
3-5: Estimation results – W/B4C sample 2	115
3-6: Estimation results – W/B4C sample 3	116
3-7: Estimation results – W/B4C sample 4	117
3-8: Estimation results – W/B4C sample 5	118

CHAPTER ONE

Modeling the temperature field and optical probe beam deflections of a periodically heated multilayer structure

ABSTRACT

A model has been developed to determine the periodic temperature field caused by modulated laser heating of a multi-layer material system. Using this model, it is possible to determine the periodic deflections of an optical probe beam passing through the air above the material, with direct applications toward photothermal deflection spectroscopy (PDS). The salient features of the model include anisotropic thermal conductivity, interfacial thermal contact resistance, and volumetric optical-to-thermal energy conversion. A solution technique using Hankel and Fourier transform methods has been employed to solve the governing energy equation. The model was validated by comparing experimental measurements of the probe beam deflections with model predictions for a NIST standard reference material (SRM) for which the thermal properties are known. In addition to treating the material as a bulk system, it was modeled as being a “virtual film”, whose properties were determined using a model-based estimation algorithm. A parametric study was also performed in order to determine the effect of model parameters on the temperature field and probe beam deflections.

1. Introduction

Photothermal deflection spectroscopy (PDS) is a laser heating technique which may be used for thermal property measurement. As shown schematically in Figure 1-1, the concept uses an intensity modulated laser to strike the surface of a test material. The effect of this laser is to heat the material and surrounding air, which will cause the refractive index of the air above the sample to vary in a periodic manner. A second laser is passed through the heated air and experiences periodic deflections. This is commonly referred to as the “mirage effect” [1, 2]. A quadrant photodetector is used to measure the deflections of this probe laser, which may then be related to the thermal properties of the sample material.

PDS falls within a broader category of "thermal wave" techniques, which include photoacoustic spectroscopy [3], 3- ω [4], modulated thermal reflectance (MTR) [5], and scanning thermal microscopy (ScThM) [6]. The unifying characteristic of these techniques is their ability to confine thermal penetration in the medium by controlling the frequency of the stimulus which heats the material (e.g. heating beam for PDS). This is important because it allows us to confine the “probe” to an area of interest in order to achieve maximum sensitivity to a particular feature (e.g. the thermal conductivity of a thin film). This feature also allows for profiling features below the surface of a material [7]. We note here that a limiting characteristic of PDS is that the thermal field cannot be substantially smaller than the probe beam. When this condition occurs, the measurements rapidly become insensitive to model parameters.

PDS was initially introduced as a method to measure the optical absorption properties of solids, liquids, gases, and thin films [1, 8-10]. It was later utilized to determine the thermal properties of bulk materials through the use of an *ad hoc* data reduction technique called the “zero-crossing” method [11, 12]. This technique relied

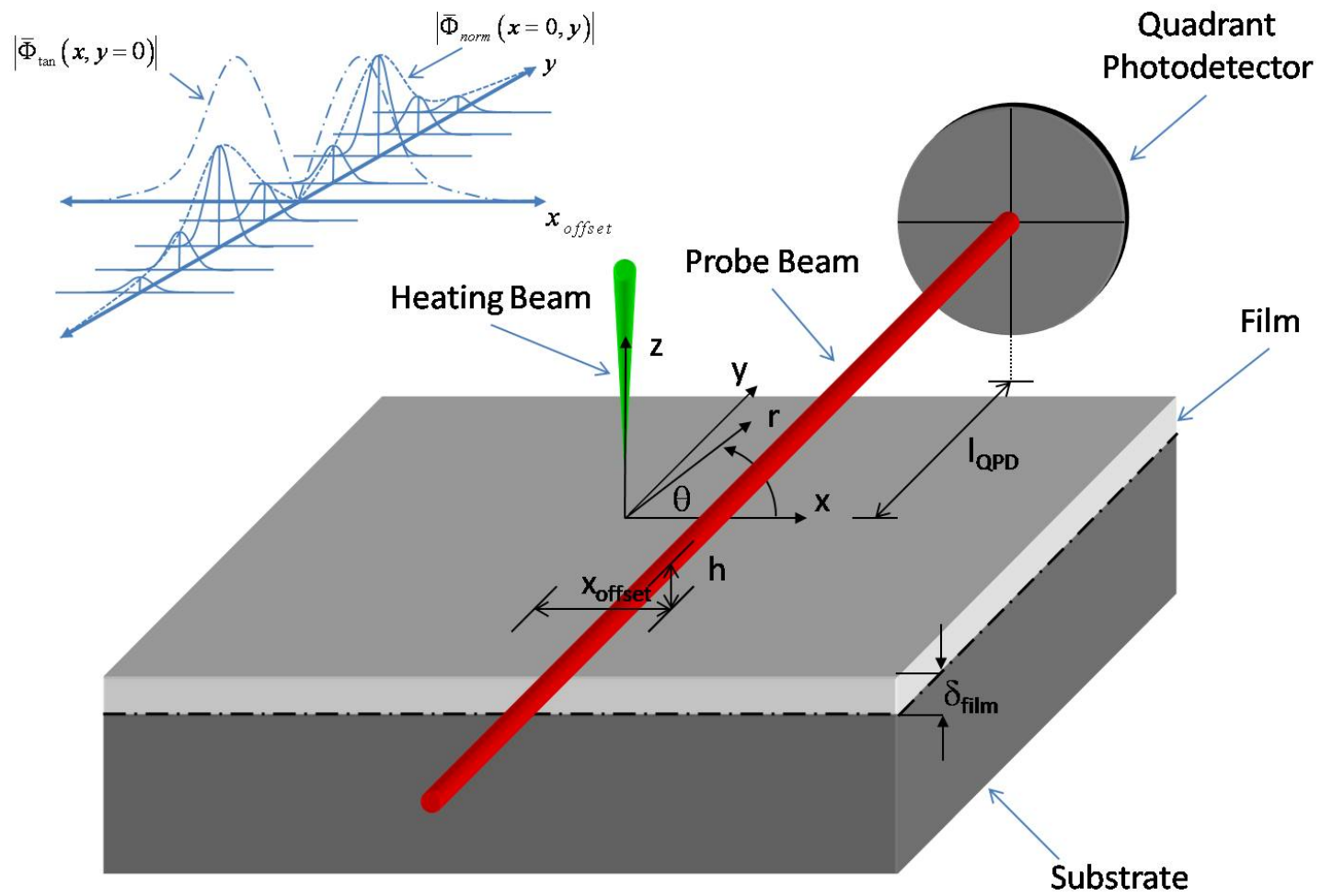


Figure 1-1: Schematic of transverse PDS w/ alignment inset

on the use of linear relationships between the probe beam deflections and the inverse square root of the modulation frequency. It was originally developed for optically and thermally thick samples, but was later adapted to allow for optically and thermally thin samples by solving the problem for a three-domain system (i.e. introduction of a backing layer) [2, 13]. More complete data analysis approaches than zero-crossing consist of multi-parameter least squares curve-fitting algorithms designed to minimize the difference between measured and predicted probe beam deflections [14-18].

In order to use PDS to extract useful information about a material's properties, it is necessary to have a suitable model of heat transfer in the solid and gas phases. Several models have been presented to predict the temperature of a spot-heated material as configured in Figure 1-2. They differ primarily in the assumptions employed, which have included the following: dimensionality (i.e. 1-D, 2-D, axisymmetry), layer structure (i.e. bulk, film-on-substrate, multi-layer), anisotropy of thermal properties, thermal contact resistance, boundary conditions, optical properties, and solution technique. All assume that conduction heat transfer is the dominant form of energy transport in the gas, with negligible convective and radiative transport [19].

Jackson et al. [10] utilized a three-domain system where volumetric optical absorption of the heating beam occurs only in the middle layer. This is appropriate for a single film suspended in air. There was no treatment of anisotropy or thermal boundary resistance, and their probe beam was treated as a single optical ray. Opsal & Rosencwaig [7] extended the theory for photoacoustics to an arbitrary number of layers but used a simplified 1-D geometry with surface absorption of the incident heat flux. McGahan & Cole [20] presented a Green's function solution to the heat equation in a multi-layered structure which incorporates volumetric energy absorption in each layer. Li and Zhang [21] account for the existence of inter-layer thermal boundary resistance and anisotropic thermal conductivity, but allowed for volumetric heat

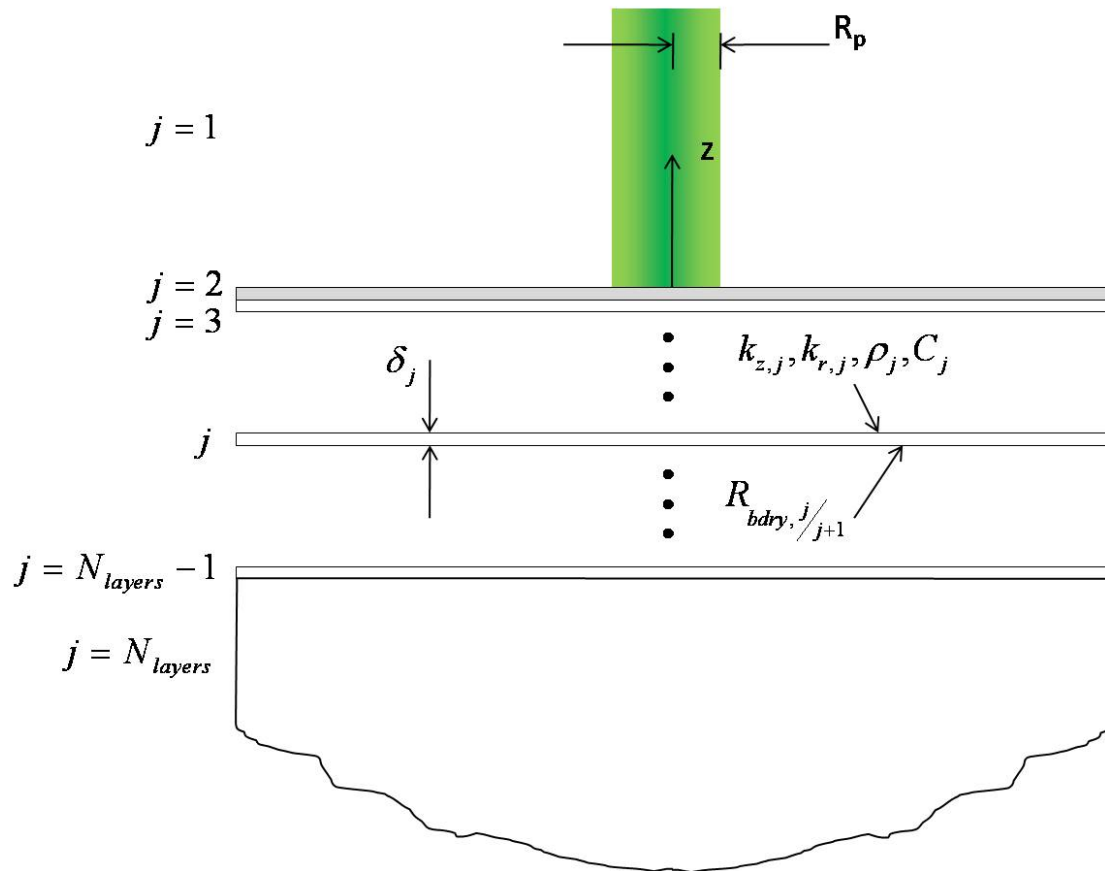


Figure 1-2: Schematic of multilayer structure

generation in only the top-most layer. No single work appears to have incorporated all of the above assumptions concurrently in the context of PDS. A more comprehensive review of PDS and related literature has been performed by our colleague, Dr. Jason Foley [22].

The purpose of this paper is the following: 1) develop a broadly applicable model for the thermal field and optical probe beam deflections caused by spot-heating a multi-layered solid with a modulated laser beam, 2) validate the model by comparisons with probe beam deflection measurements for a NIST standard reference material (SRM), and 3) apply the model to multi-layered systems to show the influence of parameters including modulation frequency, anisotropy, contact resistance, and heating and probe beam characteristics on the temperature field and probe beam deflections.

2. Model

The following assumptions are made in the present study: transverse PDS in a bounced probe beam configuration (Figures 1-1 & 1-3), a multilayered material structure (Figure 1-2), axi-symmetric heat flow, homogeneous density and specific heat within each layer, anisotropic thermal conductivity within each layer, a thermal contact resistance at each interface, temperature invariant properties, volumetric optical-to-thermal energy conversion, periodically modulated heating beam, and Gaussian (TEM_{00}) heating and probe beams.

We further assume that the continuum hypothesis is satisfied. Certainly, at length-scales below the mean free path of the energy carriers (i.e. electrons and phonons) this is not a valid assumption [23]. A continuum model, however, is conventionally applied even when phonon boundary effects are not negligible [24, 25]. This allows us to use corrected properties (i.e. not bulk) which incorporate the

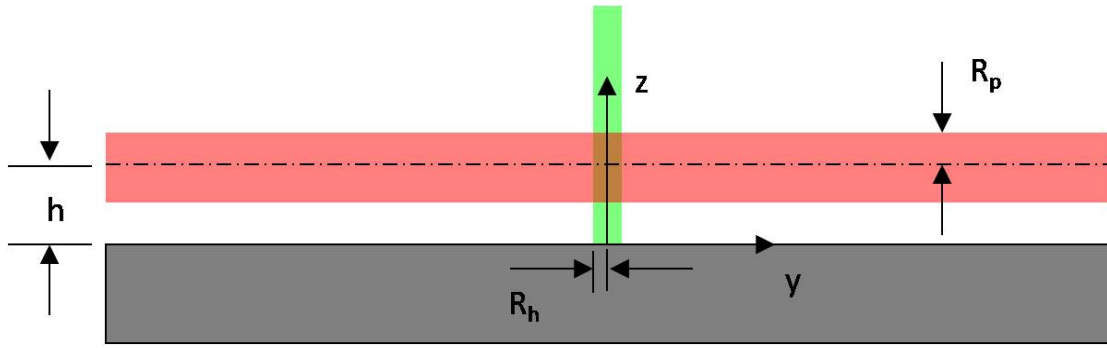


Figure 1-3a: Schematic of skimmed probe beam (y - z plane, $x = x_{\text{offset}}$)

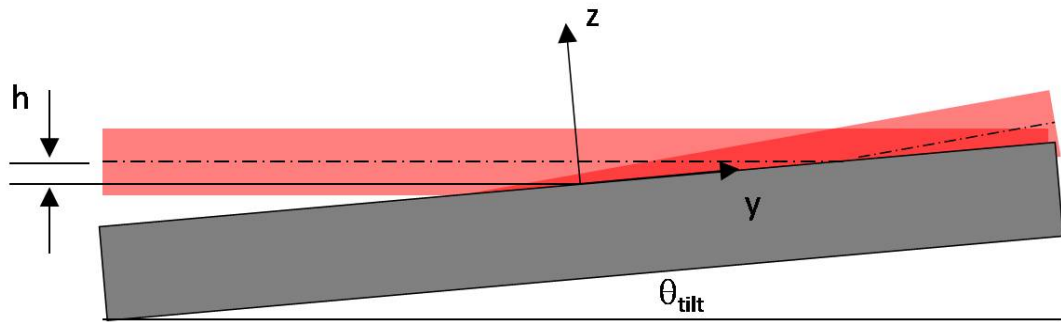


Figure 1-3b: Schematic of bounced probe beam (y - z plane, $x = x_{\text{offset}}$)

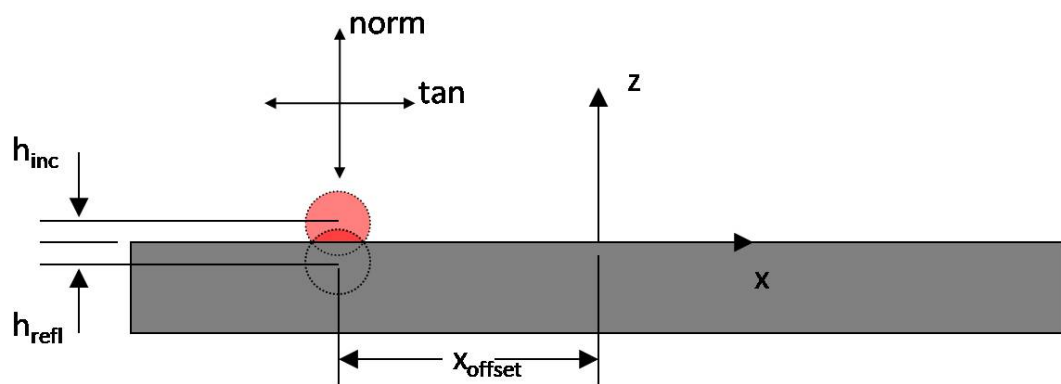


Figure 1-3c: Schematic of bounced probe beam (x - z plane, $y = 0$)

influence of quantum effects that may be applied to Fourier conduction. This is a reasonable approach based on the need for such properties in engineering design.

2.1 Thermal Field

A heating beam is used to provide periodic heating, by means of volumetric optical-to-thermal energy conversion, within the sample. The periodic heating waveform can be expressed as the sum of an infinite series of sinusoidal contributions in addition to a steady-state contribution.

$$P_h = \sum_n P_{h,n}(t) + P_{S.S.} \quad 1.1$$

Each of the terms in Eq 1.1 may be evaluated by performing a Fourier expansion of the heating beam's waveform [26]. The resulting temperature field is similarly

$$\theta = \sum_n \theta_n(t) + \theta_{S.S.} \quad 1.2.$$

We intend to solve for the temperature field resulting from a single harmonic of the heating waveform. This solution contains all of the information necessary to relate the temperature field and subsequent probe beam deflections to the thermal properties of the multilayer structure. Furthermore, the lock-in amplifier techniques we employ allow us to measure the behavior of the system at individual frequencies. Therefore, there is no need to discuss the steady-state contribution in Eq 1.2.

The energy equation for a particular layer j is

$$k_{r,j} \frac{\partial^2 \theta_{n,j}}{\partial r^2} + \frac{k_{r,j}}{r} \frac{\partial \theta_{n,j}}{\partial r} + k_{z,j} \frac{\partial^2 \theta_{n,j}}{\partial z^2} + q_{n,j}''' = \rho_j C_j \frac{\partial \theta_{n,j}}{\partial t} \quad 1.3.$$

The boundary conditions for Eq 1.3 are given in Table 1-1. The source term, $q_{n,j}'''$, can be expressed by a Gaussian radial intensity distribution of the heating beam with optical absorption governed by the Beer-Lambert law and sinusoidal modulation in the time domain as

Table 1-1: Boundary conditions to Eq 1.3 (physical domain) and Eq 1.6 (transform domain)

Physical Domain	Transform Domain
$\theta_{n,j}(r, z, t)$	$\hat{\theta}_{n,j}(\kappa, z, \omega)$
$\frac{\partial \theta_{n,j}}{\partial r}(r=0, z, t) = 0$	Satisfied by Hankel transform
$\theta_{n,j}(r \rightarrow \infty, z, t) = 0$	Satisfied by Hankel transform
$\theta_{n,j}(r, z, t) = \theta_{n,j}\left(r, z, t + \frac{m}{2\pi\omega_n}\right)$, where m = integer	Satisfied by Fourier transform
$\theta_{n,j}(r, z \rightarrow \pm\infty, t) = 0$	$\hat{\theta}_{n,j}(\kappa, z \rightarrow \pm\infty, \omega) = 0$
$k_{z,j} \frac{\partial \theta_{n,j}}{\partial z} \Big _{z=z_{bot,j}} = k_{z,j+1} \frac{\partial \theta_{n,j+1}}{\partial z} \Big _{z=z_{top,j+1}}$	$k_{z,j} \frac{\partial \hat{\theta}_{n,j}}{\partial z} \Big _{z=z_{bot,j}} = k_{z,j+1} \frac{\partial \hat{\theta}_{n,j+1}}{\partial z} \Big _{z=z_{top,j+1}}$
$\theta_{n,j+1} \Big _{z=z_{top,j+1}} - \theta_{n,j} \Big _{z=z_{bot,j}} = R_{bdry_{j,j+1}} \left(-k_{z,j} \frac{\partial \theta_{n,j}}{\partial z} \Big _{z=z_{bot,j}} \right)$	$\hat{\theta}_{n,j+1} \Big _{z=z_{top,j+1}} - \hat{\theta}_{n,j} \Big _{z=z_{bot,j}} = R_{bdry_{j,j+1}} \left(-k_{z,j} \frac{\partial \hat{\theta}_{n,j}}{\partial z} \Big _{z=z_{bot,j}} \right)$

$$q_{n,j}''' = \left[P_{top,n,j} \alpha_j e^{-\alpha_j(z_{top,j}-z)} + P_{bot,n,j} \alpha_j e^{-\alpha_j(z-z_{bot,j})} \right] \times \frac{2}{\pi R_h^2} e^{-\frac{2r^2}{R_h^2}} \times \sin(\omega_n t) \quad 1.4,$$

where α_j is the absorption coefficient in a particular layer. The terms $P_{top,n,j}$ and $P_{bot,n,j}$ represent the total amount of downward propagating optical power at the top surface of each layer and upward propagating optical power at the bottom surface of each layer, respectively. They may be calculated by accounting for reflections at each interface and subsequent absorption within each layer. These techniques have been discussed elsewhere in the literature [27, 28]. Since we are interested primarily in the thermal properties of the material, our analysis is simplified considerably by the addition of an optical absorption layer atop the multilayer structure. This reduces Eq 1.4 to

$$q_{n,j}''' = \begin{cases} (1 - refl_{surf}) |P_{h,n}| \alpha_2 e^{\alpha_2 z} \times \frac{2}{\pi R_h^2} e^{-\frac{2r^2}{R_h^2}} \times \sin(\omega_n t) & j = 2 \\ 0 & j \neq 2 \end{cases} \quad 1.5,$$

where the term $refl_{surf}$ is the reflectivity of the absorption layer at normal incidence at a particular wavelength.

Eq 1.3 can be reduced to a second-order ordinary differential equation by applying Hankel and Fourier transformations (see Appendix for details).

$$\frac{d^2 \hat{\theta}_{n,j}}{dz^2} - \Lambda_j^2 \hat{\theta}_{n,j} = -\frac{1}{k_{z,j}} \hat{q}_{n,j}''' \quad 1.6,$$

where

$$\Lambda_j = \sqrt{\frac{k_{r,j}}{k_{z,j}} \kappa^2 + i\omega \frac{\rho_j C_j}{k_{z,j}}} \quad 1.7$$

and

$$\hat{q}_{n,j}^m = \begin{cases} (1 - refl_{surf}) |P_{h,n}| \alpha_2 e^{\alpha_2 z} \times e^{-\frac{\kappa^2 R_h^2}{8}} \times \left(\frac{2\pi}{2i} [\delta(\omega - \omega_n) - \delta(\omega + \omega_n)] \right) & j = 2 \\ 0 & j \neq 2 \end{cases} \quad 1.8.$$

The boundary conditions for Eq 1.6 are given in Table 1-1. The general form of the solution to Eq 1.6 is

$$\hat{\theta}_{n,j} = c_{1,n,j} e^{\Lambda_j(z-z_{top,j}) - \frac{\kappa^2 R_h^2}{8}} + c_{2,n,j} e^{-\Lambda_j(z-z_{bot,j}) - \frac{\kappa^2 R_h^2}{8}} + \frac{1}{k_{z,j}} \frac{1}{\Lambda_j^2 - \alpha_j^2} \hat{q}_{n,j}^m \quad 1.9.$$

To solve for the unknown coefficients $c_{1,n,j}$ and $c_{2,n,j}$ in Eq 1.9, we must apply the boundary conditions expressed in Table 1-1. This results in the following equations which are to be evaluated at each interface between two adjacent layers.

$$\begin{aligned} & [k_{z,j} \Lambda_j e^{-\Lambda_j \delta_j}] c_{1,n,j} + [-k_{z,j} \Lambda_j] c_{2,n,j} + [-k_{z,j+1} \Lambda_{j+1}] c_{1,n,j+1} + [k_{z,j+1} \Lambda_{j+1} e^{-\Lambda_{j+1} \delta_{j+1}}] c_{2,n,j+1} \\ & = \begin{cases} \frac{\alpha_2^2}{\Lambda_2^2 - \alpha_2^2} (1 - refl_{surf}) |P_{h,n}| \left(\frac{2\pi}{2i} [\delta(\omega - \omega_n) - \delta(\omega + \omega_n)] \right) & j = 1 \\ 0 & j \neq 1 \end{cases} \end{aligned} \quad 1.10$$

and

$$\begin{aligned} & \left[(R_{bdry_{j,j+1}} k_{z,j} \Lambda_{z,j} - 1) e^{-\Lambda_j \delta_j} \right] c_{1,n,j} + \left[(-R_{bdry_{j,j+1}} k_{z,j} \Lambda_{z,j} - 1) \right] c_{2,n,j} \\ & \quad + [1] c_{1,n,j+1} + [e^{-\Lambda_{j+1} \delta_{j+1}}] c_{2,n,j+1} \\ & = \begin{cases} -\frac{1}{k_{z,2}} \frac{\alpha_2}{\Lambda_2^2 - \alpha_2^2} (1 - refl_{surf}) |P_{h,n}| \left(\frac{2\pi}{2i} [\delta(\omega - \omega_n) - \delta(\omega + \omega_n)] \right) & j = 1 \\ 0 & j \neq 1 \end{cases} \end{aligned} \quad 1.11.$$

In order to maintain a bounded solution in the top and bottom semi-infinite layers, we must set $c_{1,n,j=1} = 0$ and $c_{2,n,j=N_{layers}} = 0$. Written for each interface, Eqs 1.10 and 1.11 result in a block tri-diagonal matrix of size $2 \times (N_{layers} - 1)$, which must be solved for each value of the spatial wavenumber, κ . A matrix inversion solution may be used to solve for the unknown coefficients, $c_{1,n,j}(\kappa)$ and $c_{2,n,j}(\kappa)$ in Eq 1.9. Beyond a 3-layer system, the algebraic manipulations required to obtain a closed-form solution for the coefficients becomes intractable, and a generalized solution for an arbitrary

multilayered system is not possible. The calculations are readily handled, however, by software such as MATLAB.

The temperature field may be determined in physical space by performing the requisite inverse transformations, given by

$$\theta_{n,j} = \frac{1}{2\pi} \int_{\omega=-\infty}^{\infty} \left[\frac{1}{2\pi} \int_{\kappa=0}^{\infty} \kappa \hat{\theta}_{n,j} J_0(\kappa r) d\kappa \right] e^{i\omega t} d\omega \quad 1.12,$$

where $\hat{\theta}_{n,j}$ is given by Eq 1.9. The term in the square brackets is the Fourier transformed temperature field. Due to the sinusoidal source term, this may be shown to have solutions at $\omega = \pm\omega_n$ [29], which is also evident in the Dirac delta function terms contained in Eqs 1.8, 1.10 and 1.11. It may be shown that the proper linear combination of these two conditions produces a real-valued, sinusoidal result for Eq 1.12. The square-bracketed term is solved using a trapezoidal rule numerical integration scheme, although the use of quasi fast Hankel transforms [30] should be investigated to facilitate more rapid computations.

2.2 Probe Beam Deflections

We will calculate the intensity-averaged probe beam deflections caused by the temperature field determined in the Section 2.1. The deflection of a single ray, which is parallel to the sample surface (Figure 1-3a), can be broken into orthogonal components which are normal and tangential to the surface (Figure 1-3c). Similar to Eqs 1.1 and 1.2, these deflections are the sum of an infinite series of sinusoidal contributions in addition to a steady-state contribution.

$$\Phi_{\text{norm,tan}} = \sum_n \Phi_{\text{norm,tan},n}(t) + \Phi_{\text{norm,tan},S.S.} \quad 1.13,$$

where the normal and tangential components are given by [17, 31-34]

$$\Phi_{\text{tan},n} = \frac{1}{n_0} \frac{dn}{dT} \int_{y=-\infty}^{\infty} \frac{\partial \theta_{n,j=1}}{\partial x} dy \quad 1.14$$

and

$$\Phi_{\text{norm},n} = \frac{1}{n_0} \frac{dn}{dT} \int_{y=-\infty}^{\infty} \frac{\partial \theta_{n,j=1}}{\partial z} dy \quad 1.15.$$

It must be recognized that our probe beam consists of not a single ray, but a bundle of rays of differing intensity (Figure 1-3). We will assume that the probe beam is collimated in the region of the thermal field and define an intensity-averaged probe beam deflection as the convolution of a single ray (Eq 1.14 or 1.15) with the probe beam intensity distribution as

$$\bar{\Phi}_{\text{norm,tan},n} = \frac{1}{P_p} \int_{z=0}^{\infty} \int_{x=-\infty}^{\infty} I_p \Phi_{\text{norm,tan},n} dx dz \quad 1.16$$

where I_p is the intensity distribution of the probe beam. Although we utilize a bounced probe beam (Figure 1-3b) in our experiment, we are basing our computations on Eqs 1.14 and 1.15, which have been developed for a ray parallel to the sample surface. We use a model for our bounced beam which consists of the contribution from two beams parallel to the sample surface which are mirror images of each other separated by a distance $2h$ (Figure 1-3c) [17].

$$I_p = \frac{2P_p}{\pi R_p^2} e^{-\frac{2(x-x_0)^2}{R_p^2}} \left(e^{-\frac{2(z-h)^2}{R_p^2}} + e^{-\frac{2(z+h)^2}{R_p^2}} \right) \text{ for } z \geq 0 \quad 1.17$$

The first of these terms is based on the portion of the probe beam which bounces downstream of the thermal field (i.e. the incident portion), while the second is based on the portion of the probe beam which bounces upstream of the thermal field (i.e. the reflected portion). The height h is determined by the z -coordinate of the center of the probe beam as it crosses the x - z plane of the heated spot (Figure 1-2b). One important consequence of this model is that normal deflections which occur prior to bouncing are negated (i.e. sign flip) since the angle of incidence of a ray striking the surface must equal its angle of reflection. The result of this is that the normal deflections will

be zero when the probe beam is bounced at the heated spot, due to symmetry of the thermal field. This is not the case for a purely skimmed beam, nor is it the case for the tangential deflections under any circumstance.

We have solved for the intensity-averaged probe beam deflections at a particular harmonic induced by the temperature field in Eq 1.12 for $j=1$ (i.e. the gas phase). We first insert Eq 1.12 into either Eqs 1.14 or 1.15, which are subsequently inserted into Eq 1.16. It may be shown that the resulting intensity-averaged probe beam deflections are

$$\bar{\Phi}_{\tan,n} = \frac{1}{2\pi} \int_{\omega=-\infty}^{\infty} \left\{ \frac{1}{n_0} \frac{dn}{dT} \frac{1}{2} \int_{z=0}^{\infty} \frac{\sqrt{2}}{\sqrt{\pi R_p}} \left(e^{-\frac{2(z-h)^2}{R_p^2}} + e^{-\frac{2(z+h)^2}{R_p^2}} \right) \dots \right. \\ \left. \left[\frac{1}{2\pi} \int_{\kappa=-\infty}^{\infty} i\kappa c_{2n,j=1} e^{-\Lambda_{j=1}z - \frac{\kappa^2(R_h^2 + R_p^2)}{8}} e^{i\kappa x} d\kappa \right] dz \right\} e^{i\omega t} d\omega \quad 1.18$$

and

$$\bar{\Phi}_{\text{norm},n} = \frac{1}{2\pi} \int_{\omega=-\infty}^{\infty} \left\{ \frac{1}{n_0} \frac{dn}{dT} \frac{1}{2} \int_{z=0}^{\infty} \frac{\sqrt{2}}{\sqrt{\pi R_p}} \left(e^{-\frac{2(z-h)^2}{R_p^2}} \pm e^{-\frac{2(z+h)^2}{R_p^2}} \right) \dots \right. \\ \left. \left[\frac{1}{2\pi} \int_{\kappa=-\infty}^{\infty} \Lambda_{j=1} c_{2n,j=1} e^{-\Lambda_{j=1}z - \frac{\kappa^2(R_h^2 + R_p^2)}{8}} e^{i\kappa x} d\kappa \right] dz \right\} e^{i\omega t} d\omega \quad 1.19.$$

The \pm in Eq 1.19 allows the normal probe beam deflections to be used for either a skimmed (+) or a bounced (-) probe beam. For a bounced beam, $\bar{\Phi}_{\text{norm},n}(h=0) = 0$.

This produces a “notch” in the normal deflection signal whose location is useful in aligning the experiment. Performing the experiment at this condition is advantageous in data analysis since h is known.

The physics of the thermal transport within the multilayer structure are embedded in the coefficient $c_{2n,j=1}$. As with Eq 1.12, it may be shown that Eqs 1.18 and 1.19 produce real-valued, sinusoidal results. Observe that the terms in square

brackets represent an inverse Fourier transform in the spatial domain, which may be efficiently solved using commercially available fast Fourier transform (FFT) routines. The integration over the z-dimension is solved using a trapezoidal rule numerical integration scheme. Subsequent references to the real and imaginary components of the probe beam deflections (in this and future works) are referring to the complex-valued arguments to the inverse Fourier transforms in the time domain in Eqs 1.18 and 1.19 (i.e. the term in curly brackets).

3. Model Validation

3.1 Introduction

In order to validate our model, we effectively have two choices: measure the temperature field determined in Section 2.3, or measure the probe beam deflections determined in Section 2.4. Since our primary application is PDS, we take the latter approach. Our measured variables are the optical probe beam deflections from a PDS experiment using a series of NIST standard reference materials (SRMs). Specifically, we will be using NIST SRM8421 (Electrolytic Iron) [35] and NIST SRM1462 (Stainless Steel) [36]. We directly compare the probe beam deflections predicted by the model to those measured experimentally. Additionally, a model-based parameter estimation algorithm (Chapter 2) is used to determine a set of parameters that allows for the best agreement with the data.

We first make comparisons by treating the SRMs as bulk materials. Our model, however, allows for the effects of a more complex multi-layered system. Unfortunately, there are no thin film or multilayer systems that we know of which are able to serve as standard reference materials with known properties. Therefore, we developed a method to test the models ability to determine the thermal conductivity of a “virtual” film atop an otherwise bulk substrate. Unfortunately, we are unable to

validate the inclusion of thermal contact resistance and anisotropy due to a similar lack of standardization.

3.2 Experimental Apparatus

Figure 1-4 shows a schematic of the experimental apparatus. The heating beam was produced by a Coherent Innova 70 argon-ion laser operating at 514.5 nm which is coupled into a 9 μm diameter optical fiber. This fiber was coupled to a Brimrose acousto-optical modulator (AOM) (model TEM-100-5-514-2FP-9/125) to achieve square-wave intensity modulation at the desired frequencies. The modulated light exiting the fiber is then focused onto the sample surface using a matched pair of aspheric lenses ($f = 11$ mm). The focused spot size is assumed to have a radius $R_h = 4.5$ μm . The nominal amplitude of the heating beam power at the first harmonic frequency was 50 mW (c.f. $P_{h,p-p} = 78.5$ mW). Although higher power would allow for a better signal-to-noise ratio, it should be kept low enough to avoid convective and radiative phenomena that may be associated with high temperatures. In order to estimate the maximum temperature of the sample, we use the method of conduction shape factors presented by Incropera & DeWitt [37]. For a disk of diameter 9 μm (corresponding to the laser heated spot), with a steady-state incident power of 39.3 mW (c.f. 50% of $P_{h,p-p}$), we calculate that the maximum temperature in the sample will be 33 $^{\circ}\text{C}$ and 141 $^{\circ}\text{C}$ above the ambient temperature for SRM8421 and SRM1462, respectively. We believe that this estimate places an upper bound on the steady-state temperature rise, since it neglects heat transfer to the gas phase, which we know to occur. It is clear that there is a degree of ambiguity involved when thermal properties vary with temperature.

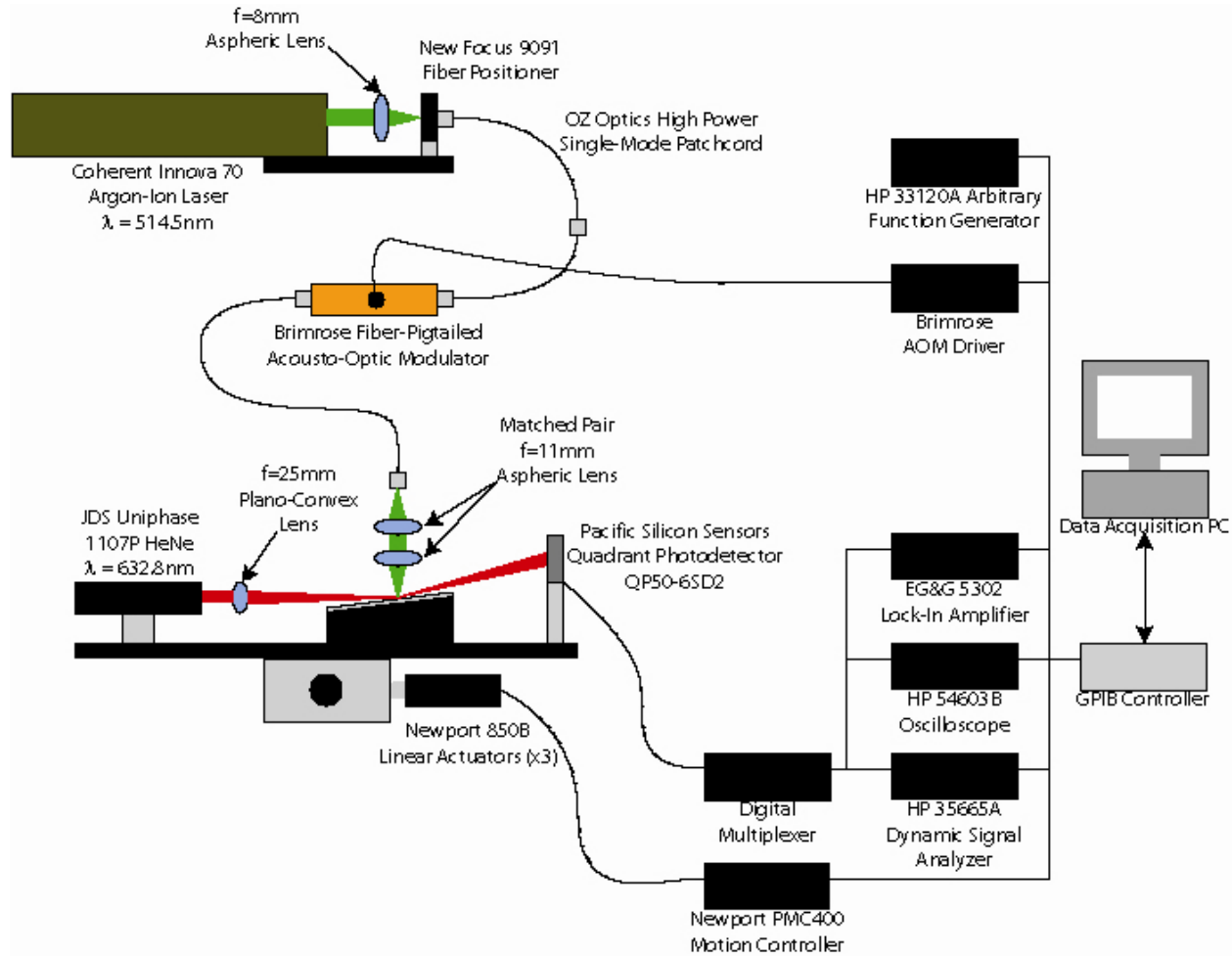


Figure 1-4: Schematic of experimental apparatus

The probe beam is produced by a JDS Uniphase HeNe laser operating at 632.8 nm which is focused onto the sample at a shallow angle ($\theta_{\text{tilt}} \sim 2^\circ$ in Figure 1-3b) such that the heating beam, probe beam, and sample surface are mutually aligned. The radius at the waist of the focused beam was measured to be 23.9 μm using a $f = 25$ mm plano-convex lens. The power of the probe beam is 0.8 mW, and is expected to make a negligible contribution toward steady-state heating, and no contribution toward periodic heating.

Deflections of the probe beam were detected using a Pacific Silicon Sensors QP50-6SD2 quadrant photodetector (QPD) with built-in amplification, summing, and differencing circuitry. An EG&G Princeton Applied Research model 5302 lock-in amplifier was used to measure the phase and amplitude of the signal from the QPD. A band-pass filter (12 dB exponential) was tuned to the modulation frequency to eliminate higher harmonics, extraneous noise sources, and to utilize the lock-in amplifier's full dynamic reserve. The time constant and sensitivity of the lock-in were set to 1 sec and 1 mV, respectively. A built-in analog-to-digital converter (ADC) was used to monitor the power of the probe beam, which is necessary for subsequent signal normalization.

The modulation frequencies selected for our experiment were $f = 1, 2, 4, 8, 16, 32, 64$ and 128 kHz. The highest frequency represents the limit of our amplifier bandwidth, above which the signal-to-noise ratio becomes poor. The one-dimensional thermal penetration depth, defined by

$$l_{pd} = \sqrt{\frac{2}{\omega_n} \frac{k_z}{\rho C}} \quad 1.20,$$

is 7.53 μm and 3.07 μm at 128 kHz for SRM8421 and SRM1462, respectively. The question of whether we will have sensitivity to films significantly thinner than this will be determined. At such a condition, the thermal wave propagates far into the

substrate, whose properties will dominate the temperature field and probe beam deflections.

The sample, probe laser, and QPD were moved in unison under a fixed heating beam using a Newport PMC400 motion controller and linear actuation stages. Scanning was performed in the X-Y plane for alignment and data collection. The heating beam's focusing lens was positioned to ensure that the waist was aligned to the sample surface. Furthermore, the height of the sample could be changed independently of the lasers using a manual elevation stage.

Alignment was achieved through observations of characteristics (e.g. minima, maxima) in the probe beam deflection signals (Figure 1-1 inset). X-direction alignment was determined by locating a characteristic “notch” in the tangential deflection signal which occurs when each half of the probe beam is deflected equally in opposite directions. Y-direction alignment was determined by locating a similar notch in the normal deflection signal. It can be shown in Eq 1.19 that the contributions from the incident and reflected portions of the probe beam nullify the normal deflection signal when the probe beam height is zero. Z-direction alignment was achieved by locating the maxima of the normal deflection signal as the heating beam focusing lens is scanned perpendicularly to the surface. This condition must be found at a position other than the aligned position to avoid the normal channel nullification which previously determined the Y-direction alignment. Looking ahead to Figures 1-5c and 1-6c, we acknowledge that there is mild asymmetry in the measurements. This effect is not predicted by the model, and seems most pronounced at the lowest frequencies. We have not been able to definitively determine the cause of this, but we believe that it may be due to misalignment of the quadrant photodetector or tilt of the sample surface. Furthermore, convection effects have been

reported to be most pronounced at low frequencies [19], which could possibly contribute to this asymmetry.

We will be comparing the measured probe beam deflections to those predicted by the model. There are two general cases for which this comparison will be made: 1.) using model parameters which we initially believe to be true (*a priori*), and 2.) using model parameters resulting from an estimation algorithm (*a posteriori*). The details of the estimation algorithm, which is based on a Levenberg-Marquardt [38] non-linear least-squares approach, are provided in (Chapter 2). The parameters which result from the algorithm are those which minimize the cost function, defined as

$$CF \equiv \frac{1}{2} \left[\sum_i \frac{1}{\sigma_i^2} (\bar{\Phi}_{\text{model},i} - \bar{\Phi}_{\text{data},i})^2 + \sum_j \frac{1}{\sigma_{0,j}^2} (s_j - s_{0,j})^2 \right] \quad 1.21$$

In Eq 1.21, σ_i represents the uncertainty (i.e. noise) in a measurement, $s_{0,j}$ represents the initial value of an estimated parameter, and $\sigma_{0,j}$ represents its initial uncertainty (which may be known with some accuracy from an alternate measurement, or may be infinite in the case of no prior knowledge). The subscript i represents an index over all measurements, while the subscript j represents an index over all parameters being estimated. $\bar{\Phi}_{\text{model}}$ represents the predicted probe beam deflections evaluated at \mathbf{s} , the suite of model parameters at the current iteration. The parameters resulting from the algorithm are not single-valued, but are represented by a normal probability density function (pdf) and may be described by a mean μ_{s_j} and standard deviation σ_{s_j} for each parameter s_j .

There are several terms in our model that act as linear multipliers to the probe beam deflection equations. These terms are embedded in either the transformed temperature coefficients (from Eq 1.9) or the probe beam deflection equations (Eqs 1.18 and 1.19). We re-write Eqs 1.18 and 1.19 as

$$\bar{\Phi}_{\text{norm, tan}, n} = \left(1 + \frac{\Delta G_1}{G_1}\right) G_1 \bar{\Phi}'_{\text{norm, tan}, n} \quad 1.22,$$

where

$$G_1 = \frac{1}{n_0} \frac{dn}{dT} (1 - \text{refl}_{\text{surf}}) |P_{h,n}| \quad 1.23.$$

G_1 is a collection of model parameters and ΔG_1 is the error associated with our knowledge of these parameters. In the case of perfect knowledge of the terms in Eq 1.23, the pre-factor in Eq 1.22 simply reduces to one. The ‘‘primed’’ probe beam deflections in Eq 1.22 have been defined such that we have removed the dependence of the parameters contained in G_1 as

$$\bar{\Phi}'_{\text{tan}, n} = \frac{1}{2\pi} \int_{\omega=-\infty}^{\infty} \left\{ \frac{1}{2} \int_{z=0}^{\infty} \frac{\sqrt{2}}{\sqrt{\pi} R_p} \left(e^{\frac{-2(z-h)^2}{R_p^2}} + e^{\frac{-2(z+h)^2}{R_p^2}} \right) \dots \right. \\ \left. \left[\frac{1}{2\pi} \int_{\kappa=-\infty}^{\infty} i\kappa c'_{2_{n,j=1}} e^{-\Lambda_{j=1} z - \frac{\kappa^2 (R_h^2 + R_p^2)}{8}} e^{i\kappa x} d\kappa \right] dz \right\} e^{i\omega t} d\omega \quad 1.24$$

and

$$\bar{\Phi}'_{\text{norm}, n} = \frac{1}{2\pi} \int_{\omega=-\infty}^{\infty} \left\{ -\frac{1}{2} \int_{z=0}^{\infty} \frac{\sqrt{2}}{\sqrt{\pi} R_p} \left(e^{\frac{-2(z-h)^2}{R_p^2}} - e^{\frac{-2(z+h)^2}{R_p^2}} \right) \dots \right. \\ \left. \left[\frac{1}{2\pi} \int_{\kappa=-\infty}^{\infty} \Lambda_{j=1} c'_{2_{n,j=1}} e^{-\Lambda_{j=1} z - \frac{\kappa^2 (R_h^2 + R_p^2)}{8}} e^{i\kappa x} d\kappa \right] dz \right\} e^{i\omega t} d\omega \quad 1.25,$$

where

$$c_{2_{n,j=1}} = (1 - \text{refl}_{\text{surf}}) |P_{h,n}| c'_{2_{n,j=1}} \quad 1.26.$$

Another linear multiplier to our probe beam deflections is the conversion factor between angular deflections and measured signals, G_0 . This parameter has been determined by calibration to be $G_0 = 180.1 \text{ rad}^{-1}$ for our experimental setup.

Assembling the above information, the probe beam deflection signals may be expressed as

$$\bar{\Phi}_{\text{norm,tan,sig}} = G_{\text{mult}} G_0 \bar{\Phi}_{\text{norm,tan}} \quad 1.27,$$

where the gain multiplier is defined as

$$G_{\text{mult}} = \left(1 + \frac{\Delta G_1}{G_1} \right) \quad 1.28.$$

This gain multiplier may be used as a floating parameter in our estimation algorithm in order to account for uncertainty in the terms contained in Eq 1.23.

3.3 Validation Results

3.3.1 Bulk

Figures 1-5a and 1-6a compare the experimental probe beam deflections for SRM8421 and SRM1462 to the probe beam deflections predicted by Eq 1.18 using the NIST published values of thermal conductivity at 300 K [35, 36] and model parameters which we initially believe to be true from the experiment (Table 1-2, Case 1). Although the model is qualitatively similar to the measurements, there are some obvious differences in the magnitude and spread of the data. In particular, the peaks of the magnitude of the tangential deflection seem to differ the most, indicating that we may have imperfect knowledge of certain model parameters. In order to determine whether this may be due to temperature dependence of the thermal conductivity, we predicted the probe beam deflections using thermal conductivities evaluated at the steady-state temperature approximated by the shape factor analysis performed in Section 3.2. The numerical results for this condition are provided in Table 1-2, Case 2, while the graphical results are provided in Figures 1-5b and 1-6b for SRM8421 and SRM1462, respectively. Based on the cost function, improvement over Case 1 was found for SRM1462, but not for SRM8421. This indicates that the differences may be due to parameters other than just thermal conductivity. In particular, we have found

that by letting the thermal conductivity, probe beam radius and linear gain multiplier to act as “floating” parameters in the estimation algorithm, we are able to achieve better agreement with the data (i.e. lower cost function). There are several combinations of model parameters which could have been used (e.g. density, specific heat, absorption coefficient, etc.), but it is prudent to use the smallest number of parameters possible in order for the estimation algorithm to converge.

Figures 1-5c and 1-6c compare the experimental probe beam deflections for SRM8421 and SRM1462 using parameters resulting from the 3-parameter fit (Table 1-2, Case 3). Although differences exist, we do not challenge the NIST published results, primarily due to the ambiguity over temperatures associated with the values we have obtained. We again point out the slight asymmetries which are evident in the data (Figures 5c and 6c) which are not predicted by the model. Similar occurrences may be found throughout the PDS literature (for example, Figure 12 in [39]), and their cause has not been clearly identified. We note that, although we show the magnitude of the tangential deflection in Figures 1-5 and 1-6, we actually fit the real and imaginary components of this deflection in order to preserve phase information. We believe that the results of this analysis validate the two-layer subset of our multilayer model.

3.3.2 Film on Substrate

Given a well-characterized NIST SRM, we will create a “virtual” film of arbitrary thickness on the surface of the otherwise bulk material. Since the “film” and “substrate” in Figure 1-1 are comprised of identical materials, we know that their properties match. The task, then, is to use our estimation algorithm to attempt to recover the properties of the “film” from the same experimental data used for the bulk analysis.

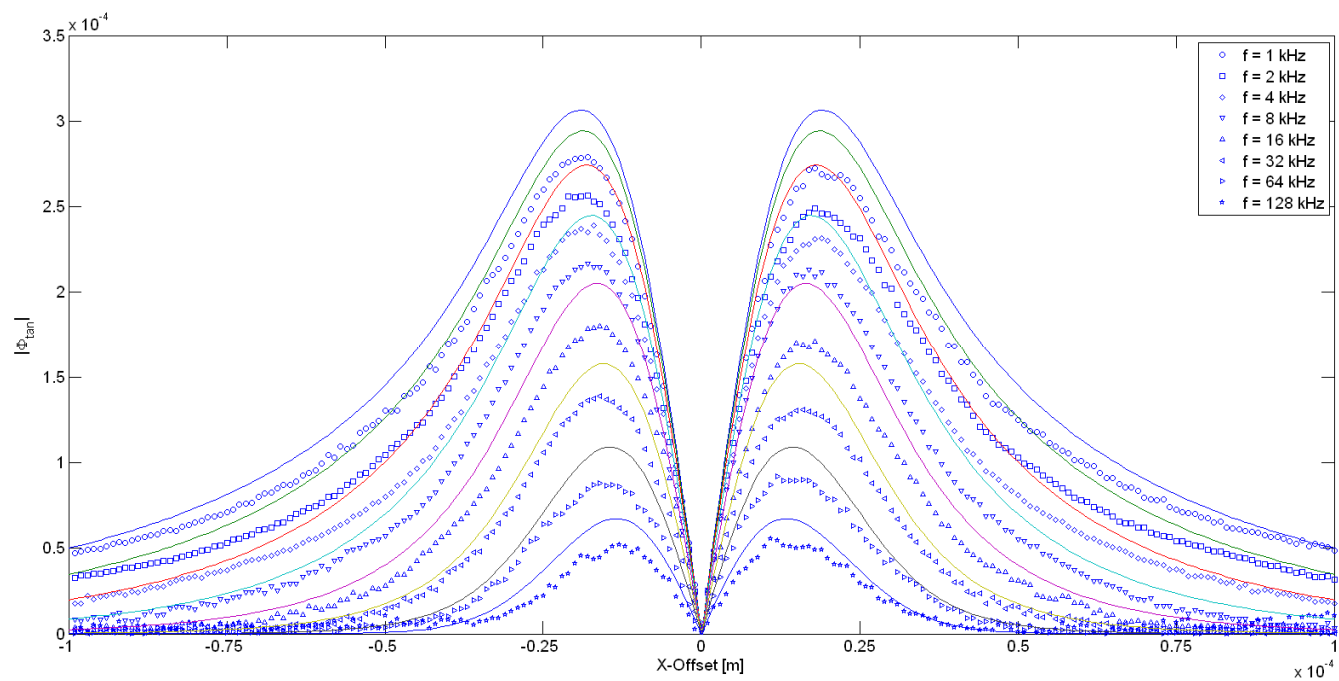
In our model, we allow the thickness of the virtual film to vary between $1 \text{ nm} < \delta < 1 \text{ mm}$. We again recognize that, at the smallest scales, the continuum assumption breaks down. This approach, however, allows us to explore the sensitivity of our model to the existence of such films, regardless of the precise mechanisms of heat transfer. The resulting mean and standard deviation (indicated by error bars) of the thermal conductivity estimates at each thickness can be found in Figures 1-7a and 1-7b for SRM8421 and SRM1462, respectively. The one-dimensional thermal penetration depths (Eq 1.20) are provided at the highest ($f = 1 \text{ kHz}$) and lowest ($f = 128 \text{ kHz}$) frequencies for each material. At film thicknesses which are on the order of, or greater than the thermal penetration depth in each material, we find excellent agreement with the thermal conductivity obtained for the bulk analysis in Section 3.3.1 (Table 1-2, Case 3). We believe that this provides a measure of validation to the three-layer subset of our multi-layer model.

For virtual films significantly thinner than the thermal penetration depth, the estimation algorithm is unable to accurately predict the thermal conductivity of the film, as evidenced by the large standard deviation of the estimated thermal conductivity at very thin film thicknesses. In this case, the thermal wave propagates far into the substrate, whose properties dominate the heat transfer into the gas phase and subsequent probe beam deflections. In order to corroborate this, we plot the maximum value of $\left| \partial \bar{\Phi}_{\tan} / \partial k_{film} \right|_{\max}$ as a function of film thickness in Figure 1-8. At film thicknesses which are thinner than the thermal penetration depth, the sensitivity to the properties of the film drops off precipitously.

Table 1-2: Comparison of model parameters and results for NIST SRM8421 and SRM1462 [35, 36]. Case 1 uses NIST published values for thermal conductivity @ 300K. Case 2 uses NIST published values for thermal conductivity evaluated at steady-state temperature approximated by shape-factor analysis. Case 3 shows the results of a 3-parameter fit using k_z , R_p , and gain multiplier.

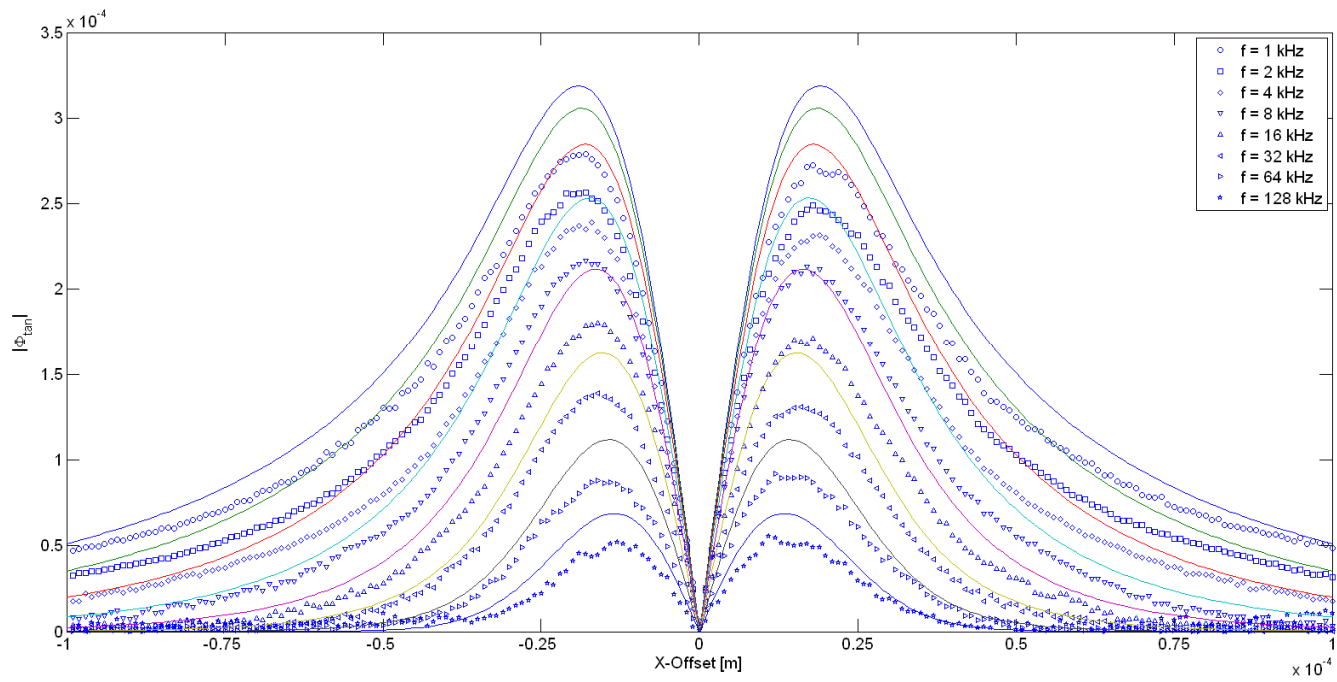
Parameter	SRM8421			SRM1462		
	Case 1	Case 2	Case 3	Case 1	Case 2	Case 3
k_z [W/m-K]	76.4 (300K)	73.3 (333K)	70.9	14.32 (300K)	16.71 (441K)	13.45
ρC [J/m ³ -kg]	3.52x10 ⁶	3.52x10 ⁶	3.52x10 ⁶	3.77x10 ⁶	3.77x10 ⁶	3.77x10 ⁶
R_p [μm]	23.9	23.9	24.0	23.9	23.9	25.3
R_h [μm]	4.5	4.5	4.5	4.5	4.5	4.5
$ P_{h,n} $ [mW]	50	50	50	50	50	50
$\text{Refl}_{\text{surf}}$	0.492	0.492	0.492	0.492	0.492	0.492
Gain Mult	1	1	0.81	1	1	0.94
Cost Function	3.34x10 ⁵	4.65x10 ⁵	9.23x10 ⁴	1.88x10 ⁶	1.05x10 ⁶	3.35x10 ⁵

Figure 1-5a – 1-5c: Comparison of experimental measurements and modeled probe beam deflections for SRM8421 (Electrolytic Iron). Conditions are: a.) thermal conductivity of SRM8421 @ 300K, b.) thermal conductivity of SRM8421 @ 333K, and c.) 3-parameter fit with thermal conductivity, probe beam radius, and gain multiplier. Other *a priori* model parameters provided in Table 1-2.



(a)

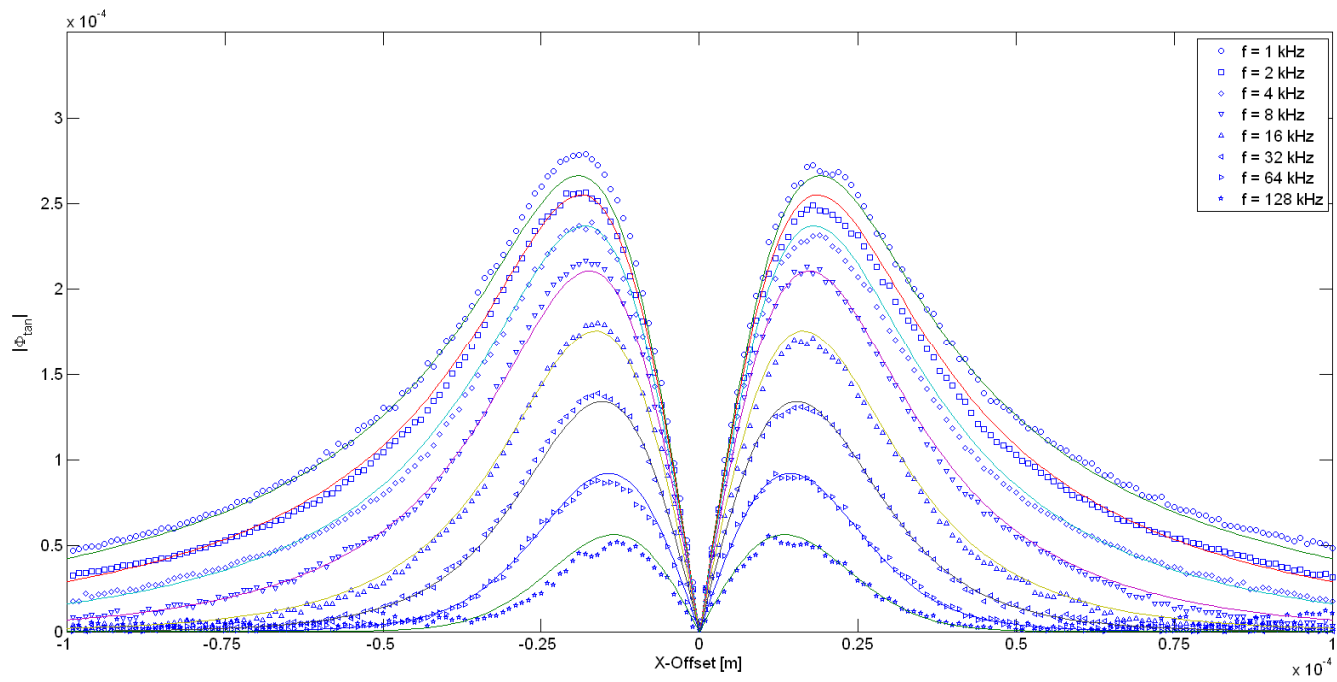
Figure 1-5 (continued)



(b)

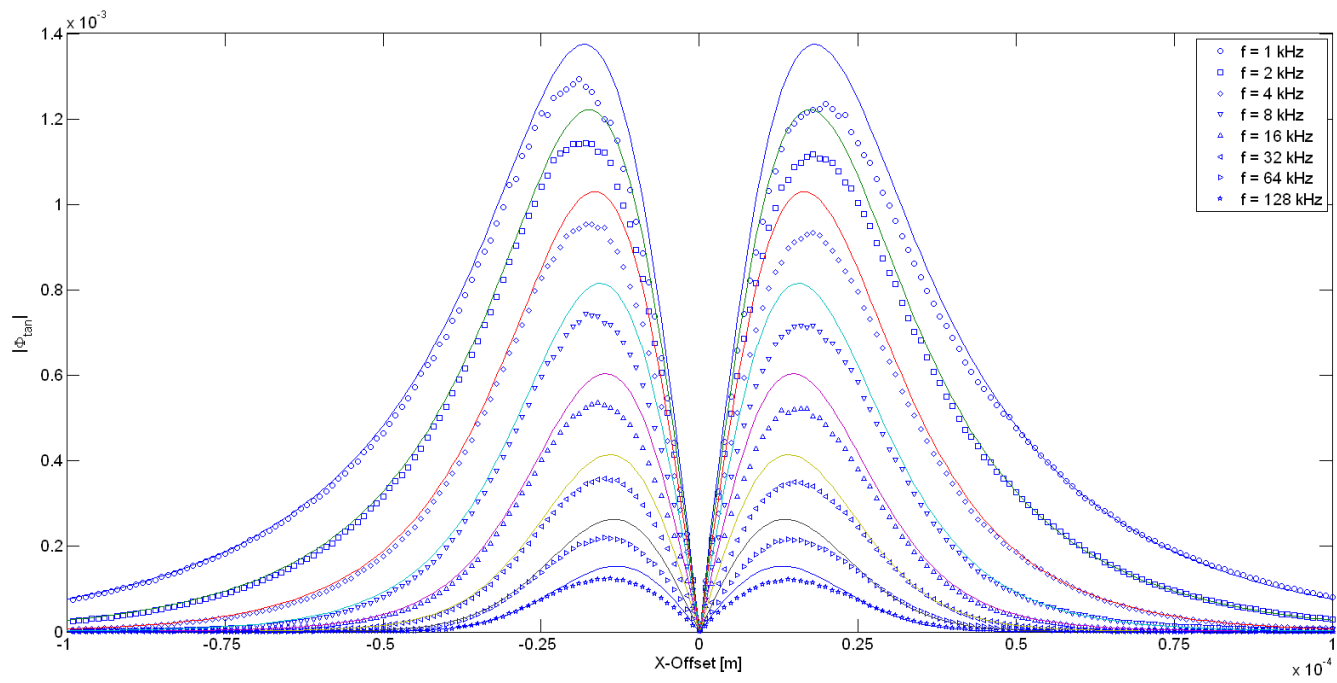
Figure 1-5 (continued)

30



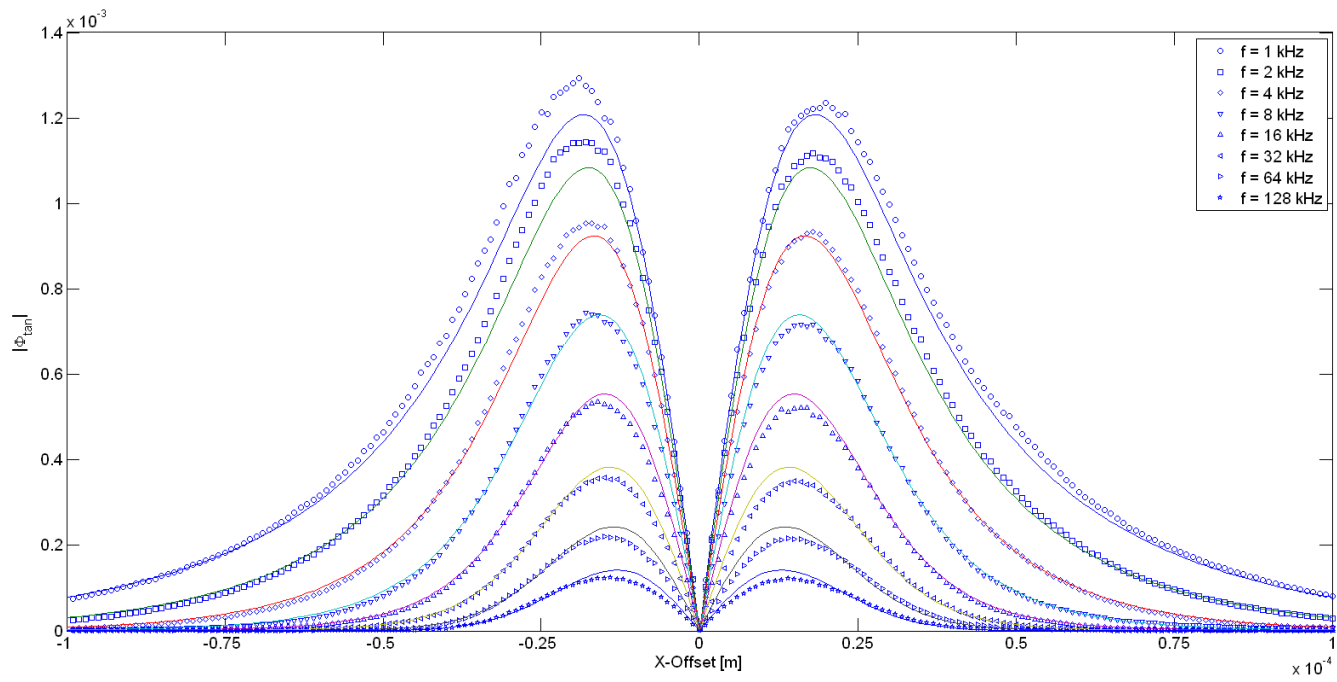
(c)

Figure 1-6a – 1-6c: Comparison of experimental measurements and modeled probe beam deflections for SRM1462 (Stainless Steel). Conditions are: a.) thermal conductivity of SRM8421 @ 300K, b.) thermal conductivity of SRM8421 @ 441K, and c.) 3-parameter fit with thermal conductivity, probe beam radius, and gain multiplier. Other *a priori* model parameters provided in Table 1-2.



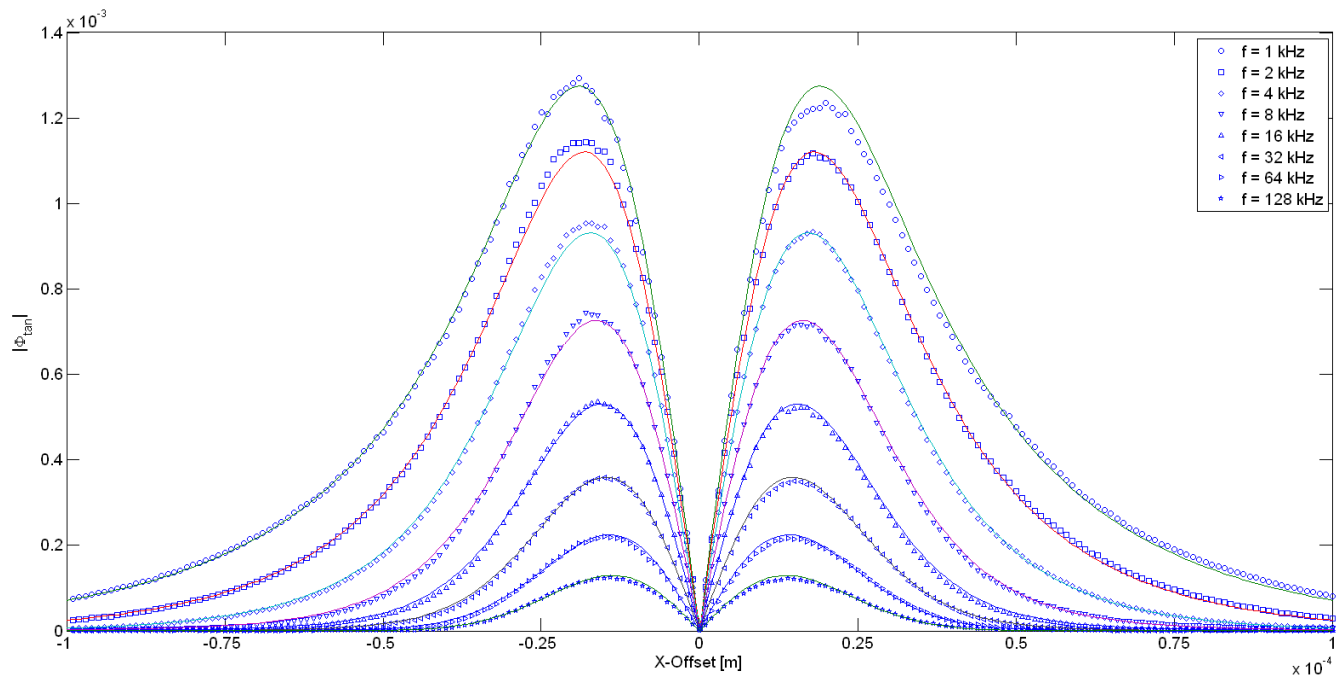
(a)

Figure 1-6 (continued)



(b)

Figure 1-6 (continued)



(c)

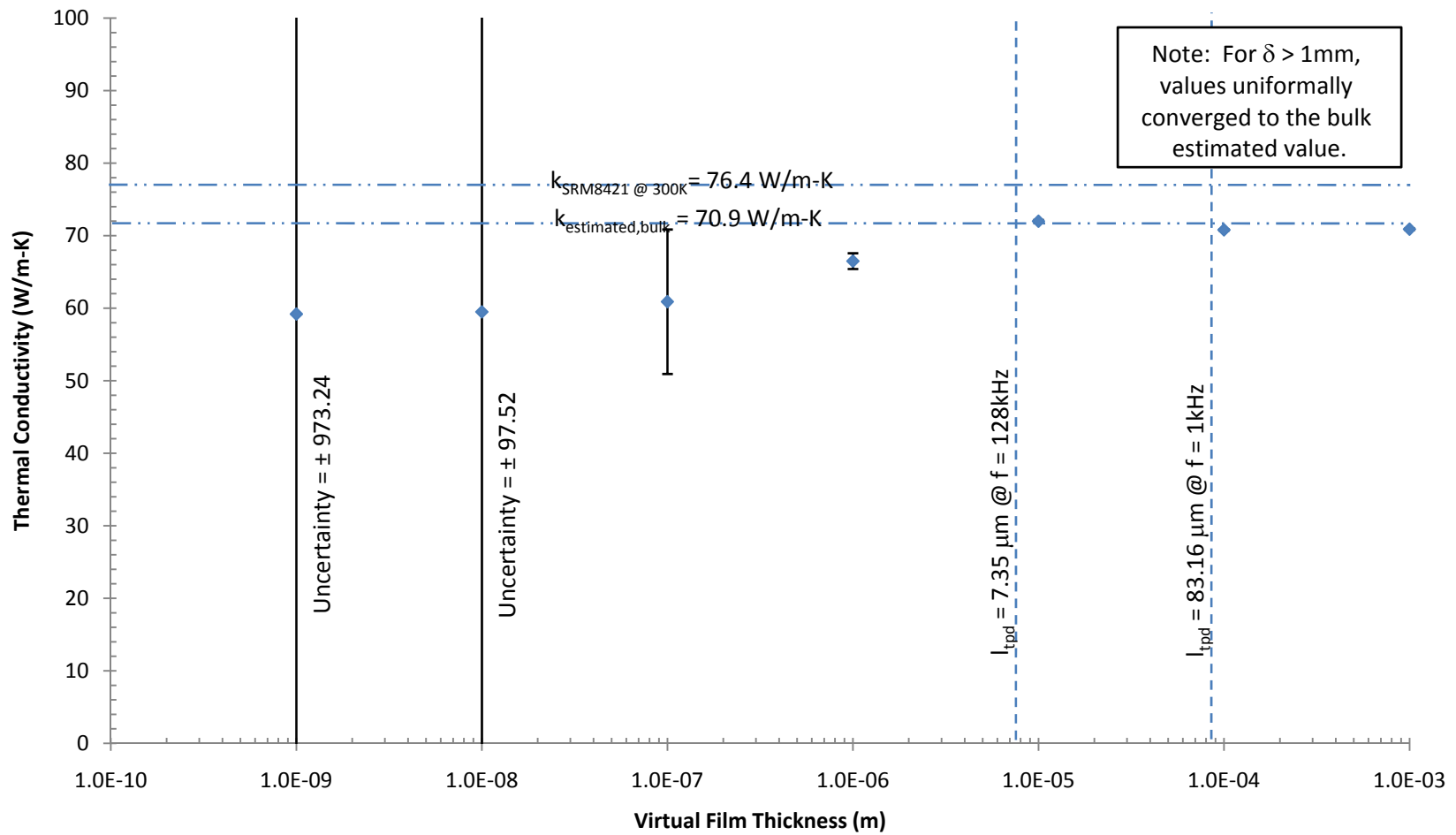


Figure 1-7a: Results of virtual film analysis for NIST SRM8421

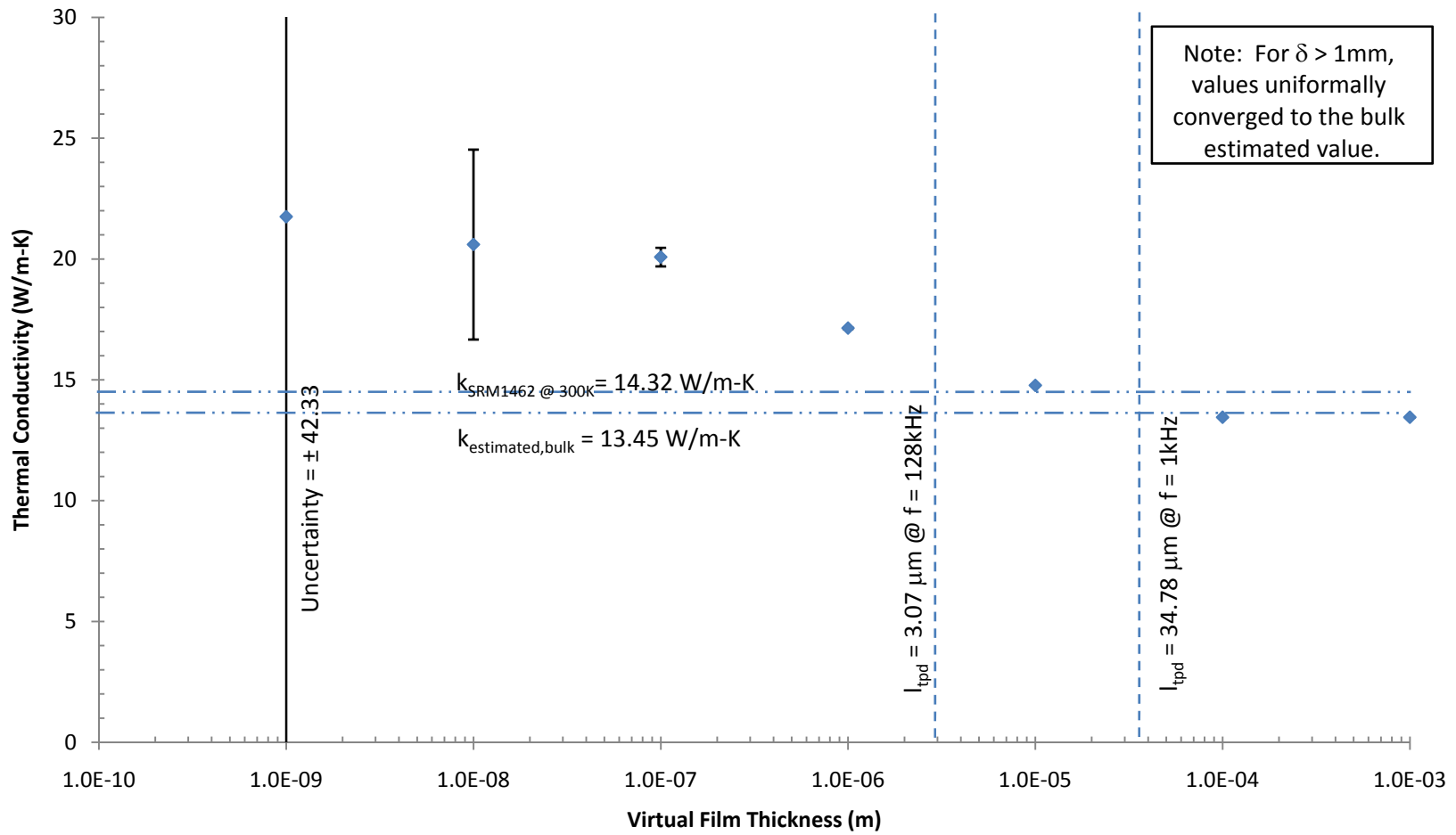


Figure 1-7b: Results of virtual film analysis for NIST SRM1462

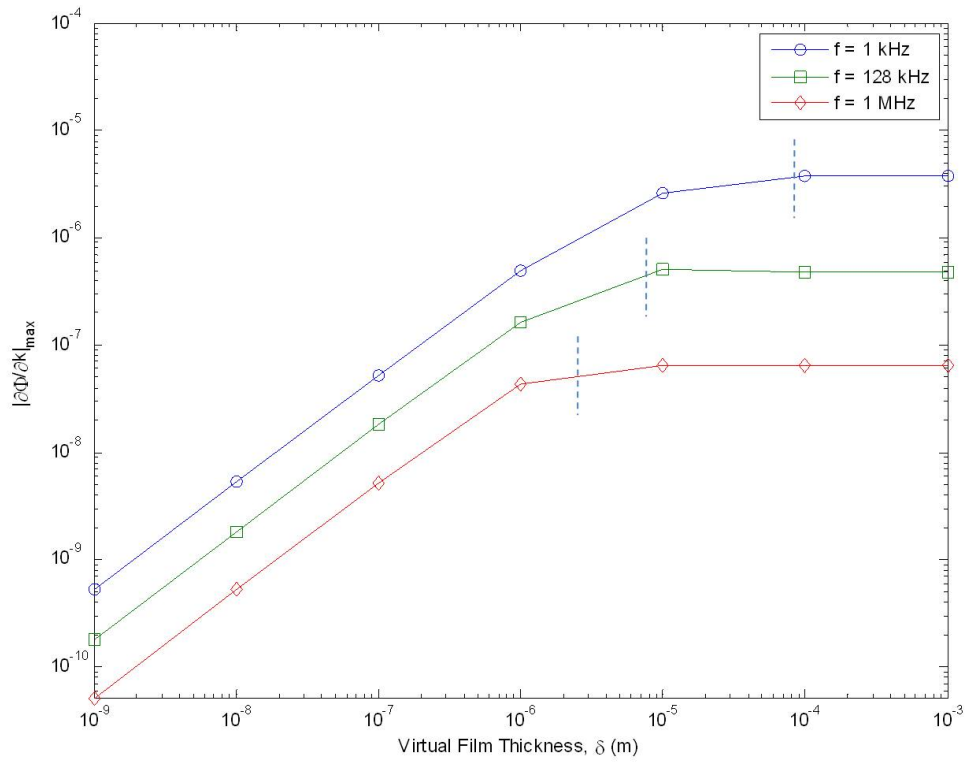


Figure 1-8: Sensitivity of probe beam deflections to the thermal conductivity of a virtual film of thickness δ . Dashed lines represent thermal penetration depth (Eq 1.20) at each frequency.

4. Parametric Investigation

In this section, we illustrate the influence of several model parameters on the periodic components of the temperature field and optical probe beam deflections developed in Section 2. For the purposes of these simulations, we use the following systems: bulk Si, SiO₂ film on Si substrate, and SiO₂/Si multilayer on Si substrate. In each case, a 100nm layer of tungsten (W) is used as the top-most optical absorption layer. The bulk properties used for these calculations may be found in Table 1-3, understanding that the true properties of these materials may differ significantly depending on factors such as doping concentration and fabrication process [40, 41]. Other model parameters may be found in Table 1-4. Variations to these values will be indicated where necessary. It is worthy of noting that the heating beam power is modeled to be 1 W in this investigation. This is a truly unreasonable power with such a small heating beam radius. The temperature fields and probe beam deflections will scale, however, with this temperature. The following figures should be interpreted accordingly (i.e. per Watt of heating beam power).

Figures 1-9a through 1-9d show the magnitude of the temperature oscillations as the modulation frequency is varied from 1 kHz < f < 1 MHz. The contour lines, which indicate drops of $e^{-n/4}$ ($n=1,2,3\dots$) from $|\theta_{\max}|$ (which always occurs at $r = 0, z = 0$), show that the temperatures decay more rapidly at high frequencies (Figure 1-9d) than at low frequencies (Figure 1-9a). It is clear that there is more confinement of the thermal field at high frequencies, as would be predicted from the thermal penetration depth in Eq 1.20. The peak temperature varies only slightly between each case, since the integrated amount of energy put into the sample is the same. Figure 1-9e shows that the reduced size of the thermal field creates tangential probe beam deflections of smaller magnitude. This is due to the fact that the probe beam becomes large

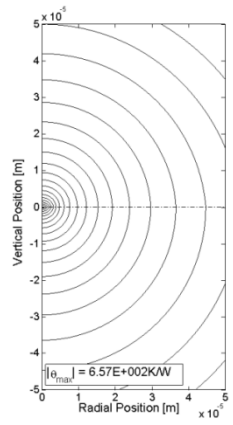
Table 1-3: Default material properties used in Section 4. Properties @ 300K obtained from Incropera & DeWitt [37].

Property	Si	SiO₂	W
k_z [W/m-K]	148	1.38	174
k_r/k_z	1	1	1
ρ [kg/m³]	2,330	2,220	19,300
C [J/kg-K]	712	745	132

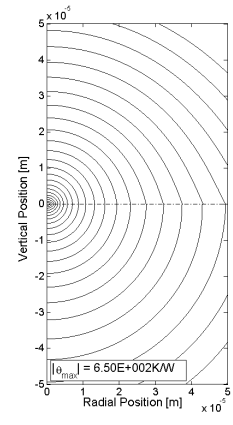
Table 1-4: Default model parameters used in Section 4

Parameter	Value
P_h [W]	1
R_h [μm]	2.0
R_p [μm]	21.3
h [μm]	0
Gain [rad⁻¹]	150
f [Hz]	1000

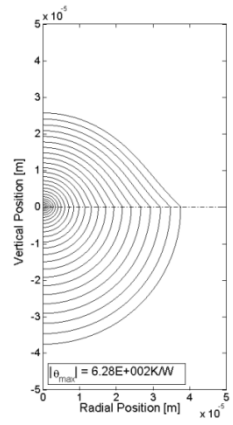
Figures 1-9a – 1-9e: Effect of modulation frequency (f) on the temperature field and probe beam deflections in Si. Frequencies are: a.) 1 kHz, b.) 10 kHz, c.) 100 kHz and d.) 1 MHz. Figures 1-9a – 1-9d show the magnitude of the temperature field at each frequency. The contour lines indicate drops of $e^{-n/4}$ ($n=1,2,3,\dots,24$) from $|\theta_{\max}|$, which occurs at (0,0). Figure 1-9e shows the magnitude of the tangential probe beam deflection at each frequency.



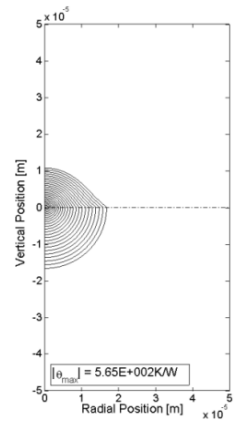
(a)



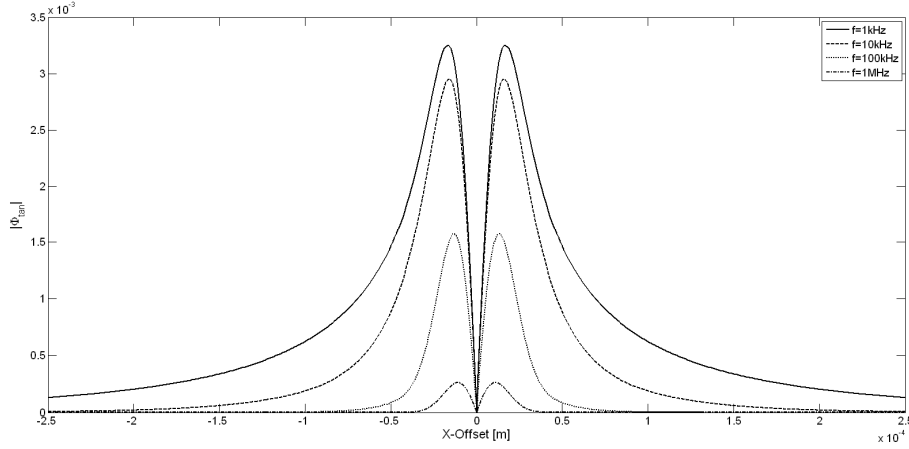
(b)



(c)



(d)



(e)

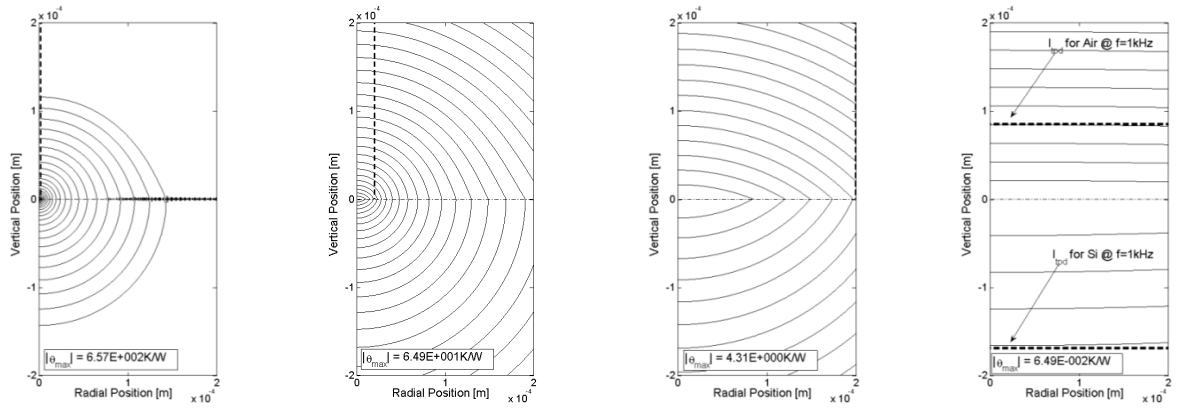
compared to the size of the thermal field, and less of it passes through heated portions of the gas.

Figures 1-10a through 1-10d show the effect of heating beam radius (R_h) on the thermal field. At small radii, the temperature field is clearly two-dimensional in nature. As the radius increases, however, the temperature field becomes progressively one-dimensional. At the limit of an infinitely wide heating beam, we expect the thermal penetration depth to be predicted by Eq 1.20. This is clearly the case, even at $R_p = 2.0$ mm in Figure 1-10d. In Figure 1-10e, we observe that the tangential probe beam deflections become vanishingly small as the radius increases. This is because a one-dimensional thermal field has no temperature gradients in the x-direction, which is what drives the tangential deflections in Eq 1.14. This condition is not helpful at the aligned position, since both the normal and tangential deflection signals will be zero.

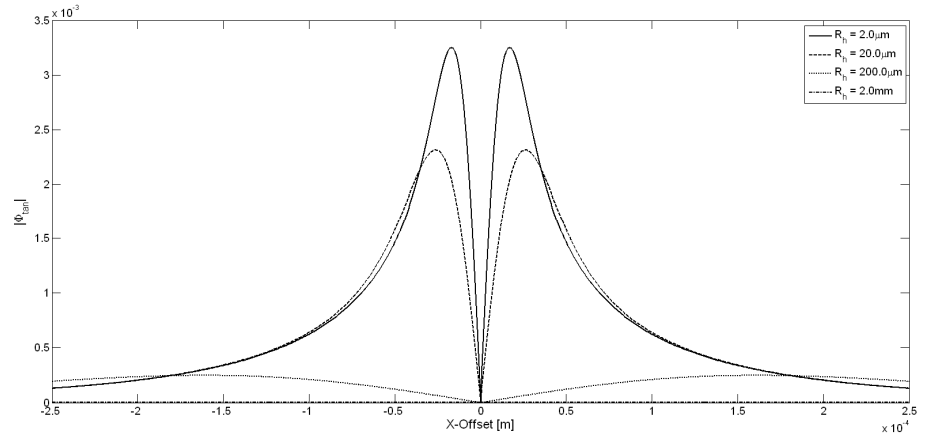
Figures 1-11a through 1-11e show the effect of anisotropic thermal conductivity (defined as k_r/k_z) on the thermal field. At low levels of anisotropy, we see strong effects of confinement in the radial direction, directing energy deep into the substrate. As anisotropy is increased, however, there is strong radial spreading. As it tends toward infinity, all heat flow will be in the radial direction. This is the reason why, in Figure 1-11f, the tangential probe beam deflections diminish as anisotropy is increased. Once again, the radial spreading decreases the temperature gradients in the x-direction of the gas through which the probe beam passes.

Figures 1-12a through 1-12d show the effect of increasing thermal contact resistance from $10^{-8} < R_{\text{bdry}} < 10^{-5}$ m²-K/W located between a 1 μ m film of SiO₂ and a semi-infinite Si substrate. The inset figures show the full thermal field, while the main figures provide a close-up of the film/substrate interface. In these figures, the W absorption layer is visible atop the SiO₂ film (dashed line). At small values of contact

Figures 1-10a – 1-10e: Effect of heating beam radius (R_h) on the temperature field and probe beam deflections in Si. Radii are: a.) $2\mu\text{m}$, b.) $20\mu\text{m}$, c.) $200\mu\text{m}$ and d.) 2mm indicated by dashed vertical line. Figures 1-10a – 1-10d show the magnitude of the temperature field at each radius. The contour lines indicate drops of $e^{-n/4}$ ($n=1,2,3,\dots,24$) from $|\theta_{\text{max}}|$, which occurs at $(0,0)$. 1-10e shows the magnitude of the tangential probe beam deflection at each radius.

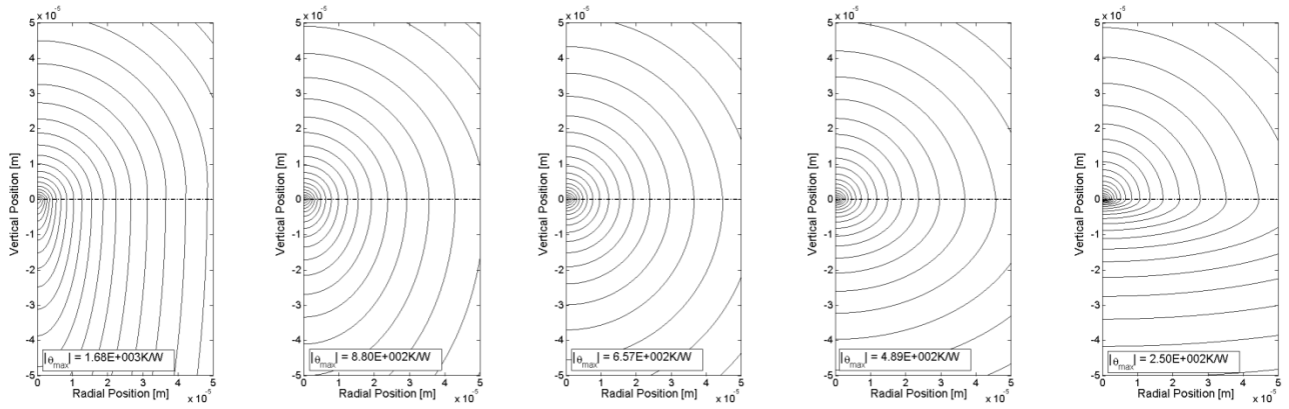


(a) (b) (c) (d)

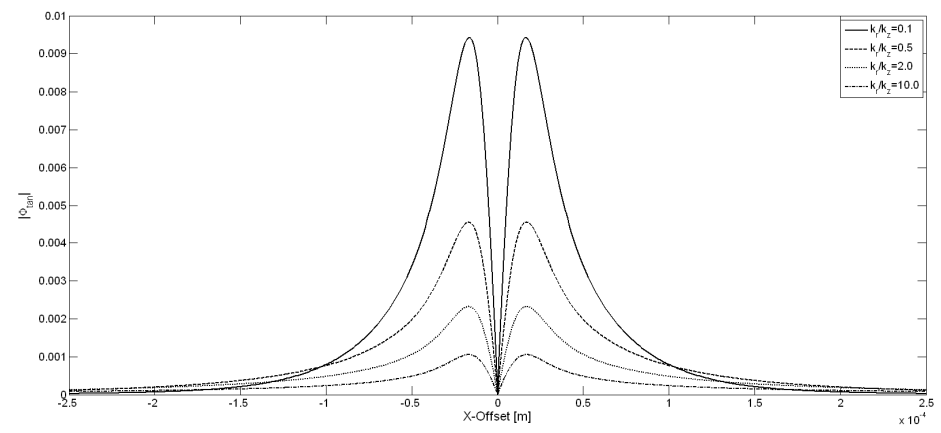


(e)

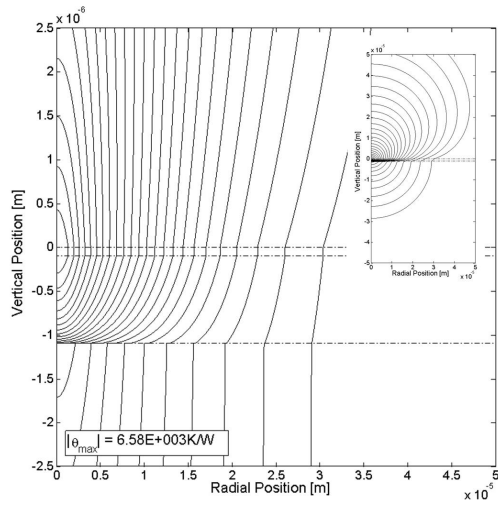
Figures 1-11a – 1-11f: Effect of anisotropy (k_r/k_z) on the temperature field and probe beam deflections in Si. Anisotropy levels are: a.) 0.1, b.) 0.5, c.) 1.0, d.) 2.0 and e.) 10.0. Figures 1-11a – 1-11e show the magnitude of the temperature field at each level of anisotropy. The contour lines indicate drops of $e^{-n/4}$ ($n=1,2,3,\dots,24$) from $|\theta_{\max}|$, which occurs at (0,0). Figure 1-11f shows the magnitude of the tangential probe beam deflection at each level of anisotropy.



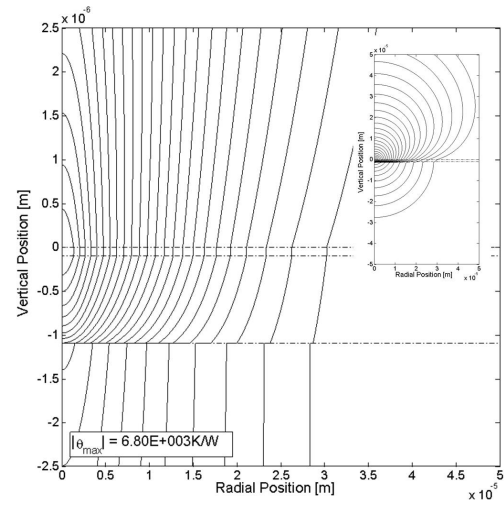
(a) (b) (c) (d) (e)



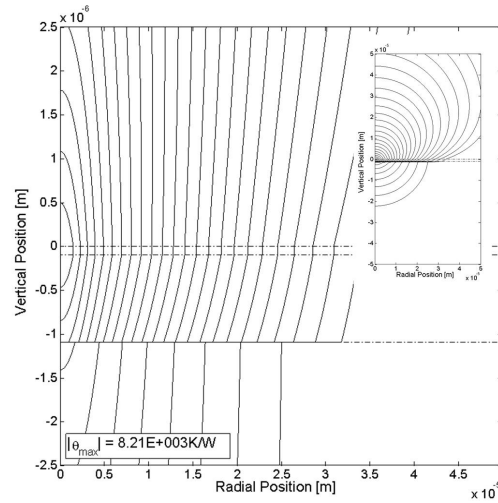
(f)



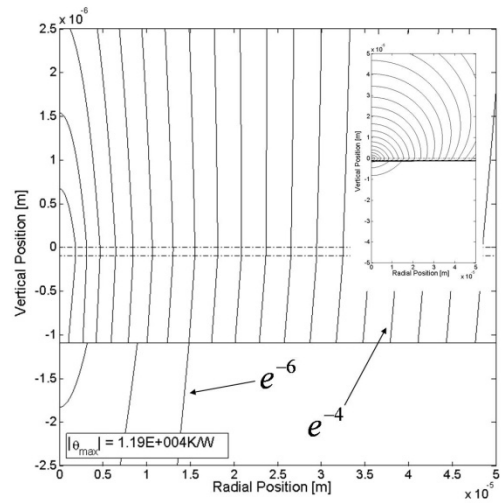
(a)



(b)



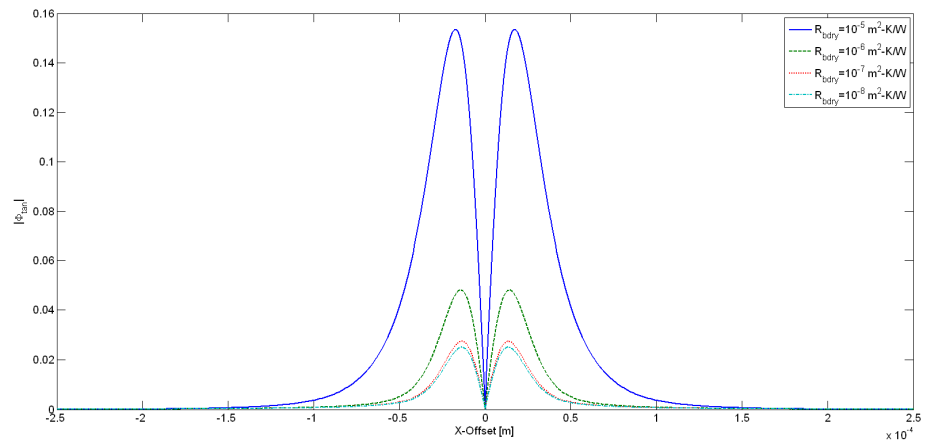
(c)



(d)

Figures 1-12a – 1-12e: Effect of thermal contact resistance (R_{bdry}) located between a 1 μm SiO₂ film and Si substrate on the temperature field and probe beam deflections. R_{bdry} is a.) 10^{-8} m²-K/W, b.) 10^{-7} m²-K/W, c.) 10^{-6} m²-K/W and d.) 10^{-5} m²-K/W. Figures 1-12a – 1-12d show the magnitude of the temperature field for each value of contact resistance. Layer interfaces, including the 100nm W absorption layer, are indicated by dashed lines. The contour lines indicate drops of $e^{-n/4}$ ($n=1,2,3,\dots,24$) from $|\theta_{max}|$, which occurs at (0,0). Figure 1-12e shows the magnitude of the tangential probe beam deflections for each value of contact resistance.

Figure 1-12 (continued)



(e)

resistance, we see only small temperature excursions across the boundary. As the resistance increases, however, substantial jumps become evident, particularly in the locations of greatest heat flux (i.e. greatest temperature gradients). Ultimately, the contact resistance may be so high that it prohibits any heat from entering the substrate. This localization of energy in the film and gas phase causes higher temperature gradients, thus larger probe beam deflections in Figure 1-12e.

Figures 1-13a and 1-13b show the thermal field in a multi-layer stack of alternating SiO₂/Si films. In Figure 1-13a, the bi-layer thickness is 0.5μm with a total stack height of 1μm (i.e. 2 periods). In Figure 1-13b, the bi-layer thickness is 0.25μm with the same total stack height (i.e. 4 periods). In both of these cases, we see a large temperature drop across the individual SiO₂ layers, with virtually no temperature drop across the more conductive Si layers. This indicates a predominantly radial heat flow pattern in the conductive Si layer, and a predominantly axial heat flow pattern in the insulating SiO₂ layer.

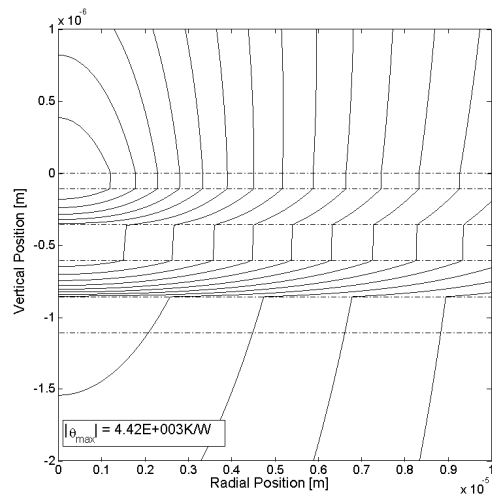
In Figure 1-14a, we show the effect of increasing the probe beam radius from 15.4 μm < R_p < 60.7 μm. The most notable effect is that the magnitude of the probe beam deflections diminish with increasing radius. This is due to the convolution effect (i.e. $e^{-\frac{\kappa^2(R_h^2+R_p^2)}{8}}$ in Eqs 1.18 and 1.19) that the probe beam has on the single-ray deflections. At small radii, the probe “volume” is small, and the gas within this volume is at a higher average temperature. Conversely, at large radii, the probe volume is large and may extend outside of the influence of the thermal field. It appears evident that one should choose the smallest probe beam possible, but there are some physical and practical limitations involved. Certainly, the optical setup must allow for physical clearance of the components. Furthermore, it was implicit in the development of our model that the probe beam is collimated throughout the entire thermal field. In laser optics, the depth of focus scales with the focused spot size.

Although it is physically possible to focus a laser beam to the order of its wavelength (i.e. $R_p \sim 1\mu m$), such a beam is rapidly divergent and may not be considered collimated. Larger probe beams also allow for a degree of relaxation in the relatively difficult alignment procedure.

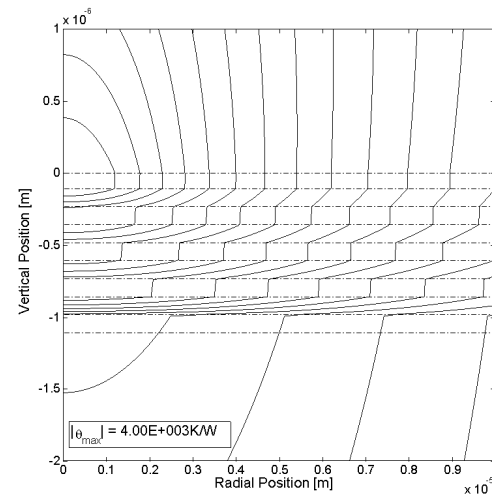
Figure 1-14b demonstrates the effect of probe beam height on the probe beam deflections. This figure shows that the tangential probe beam deflections are strongest when the center of the probe beam is very close to the surface, where the highest temperature gradients exist. As the probe beam height is increased, however, the probe volume begins to rise above the influence of the thermal field resulting in smaller magnitude deflections. Notice that the effects seen in Figure 1-14b are very similar to those seen in Figure 1-14a. This provides evidence that it may be difficult to differentiate between the effect of probe beam height and probe beam radius in our estimation algorithm. For this reason, we typically prefer to perform the experiment at an aligned position of $h = 0$.

5. Summary & Conclusions

A model has been developed to determine the modulated thermal field and optical probe beam deflections caused by periodic laser heating of a multi-layer material system. Fourier and Hankel transform methods have been used to reduce the governing heat equation to an ordinary differential equation. Application of interfacial boundary conditions leads to a solution in transform space, which is related to the physical domain through the requisite inverse transform procedures. These temperature fields were used to determine expressions for the intensity-average probe beam deflections. All information about the thermal properties in the multi-layer system is contained in a single coefficient resulting from the solution of the temperature field in the gas phase.

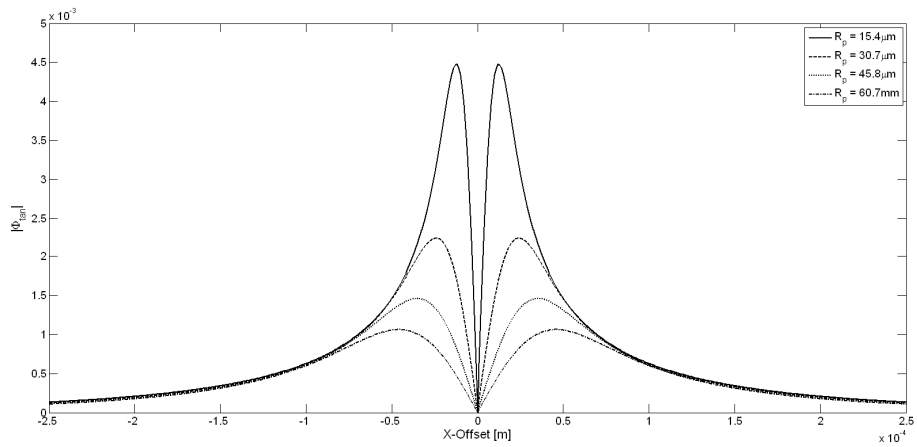


(a)

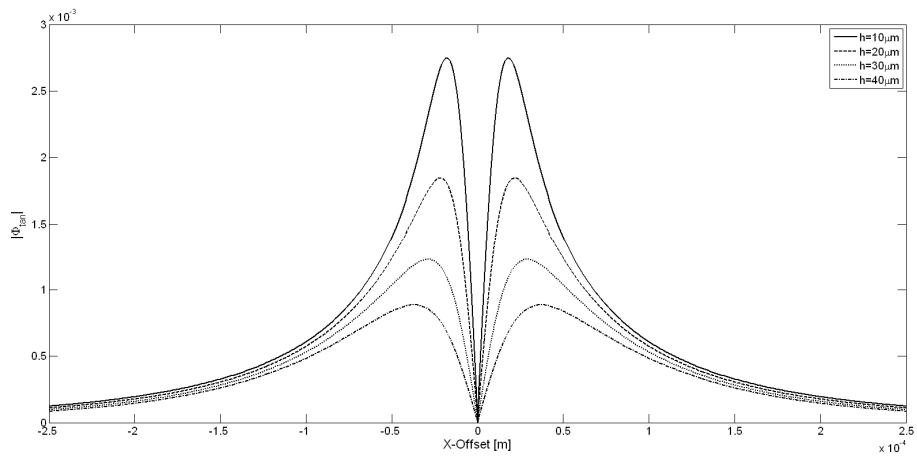


(b)

Figures 1-13a – 1-13b: Temperature field in a multi-layer stack of SiO_2/Si with a Si substrate. In Figure 1-13a, there are 2 periods with individual film thicknesses of $0.25 \mu\text{m}$, providing a total stack height of $1 \mu\text{m}$. In Figure 1-13b, there are 4 periods with individual film thicknesses of $0.125 \mu\text{m}$, providing a total stack height of $1 \mu\text{m}$. In each system, the top-most layer is a 100nm film of W used for optical absorption. The contour lines indicate drops of $e^{-n/4}$ ($n=1,2,3,\dots,24$) from $|\theta_{\text{max}}|$, which occurs at $(0,0)$.



(a)



(b)

Figures 1-14a – 1-14b: Effect of probe beam parameters on the magnitude probe beam deflections for Si. Figure 1-14a shows the effect of increasing probe beam radius (R_p) on the magnitude of the tangential probe beam deflections. Figure 1-14b shows the effect of increasing probe beam height (h) on the magnitude of the tangential probe beam deflections.

The model was validated for the case of bulk and film-on-substrate subsets of the full multi-layer case using measured probe beam deflections for NIST SRM8432 and SRM1462 in a bounced-probe transverse PDS experiment. The film-on-substrate case was accomplished by treating the material as having a “virtual film” of varying thickness atop the otherwise bulk substrate. Using a non-linear least-squares estimation algorithm, we were able to reproduce the thermal conductivity of this film when its virtual thickness was greater than or equal to the thermal penetration depth in the material. For virtual thicknesses much smaller than this length-scale, however, the sensitivity of the model to the properties of the virtual film were too small to allow the estimation algorithm to accurately predict the thermal conductivity.

REFERENCES

- [1] J. C. Murphy and L. C. Aamodt, "Photothermal spectroscopy using optical beam probing: Mirage effect," *Journal of Applied Physics*, vol. 51, pp. 4580-4588, 1980.
- [2] A. Salazar, A. Sanchez-Lavega, and J. Fernandez, "Theory of thermal diffusivity determination by the "mirage" technique in solids," *Journal of Applied Physics*, vol. 65, pp. 4150-4156, 1989.
- [3] A. Rosencwaig, "Photo-acoustic spectroscopy of solids," *Review of Scientific Instruments*, vol. 48, pp. 1133-1137, 1977.
- [4] D. G. Cahill, "THERMAL-CONDUCTIVITY MEASUREMENT FROM 30-K TO 750-K - THE 3-OMEGA METHOD," *Review of Scientific Instruments*, vol. 61, pp. 802-808, Feb 1990.
- [5] C. A. Paddock and G. L. Eesley, "TRANSIENT THERMOREFLECTANCE FROM THIN METAL-FILMS," *Journal of Applied Physics*, vol. 60, pp. 285-290, Jul 1986.
- [6] A. Majumdar, "Scanning thermal microscopy," *Annual Review of Materials Science*, vol. 29, pp. 505-585, 1999.
- [7] J. Opsal and A. Rosencwaig, "THERMAL-WAVE DEPTH PROFILING - THEORY," *Journal of Applied Physics*, vol. 53, pp. 4240-4246, 1982.
- [8] A. C. Boccara, D. Fournier, W. Jackson, and N. M. Amer, "Sensitive photothermal deflection technique for measuring absorption in optically thin media," *Optics Letters*, vol. 5, pp. 377-379, 1980.
- [9] D. Fournier, A. C. Boccara, N. M. Amer, and R. Gerlach, "Sensitive in situ trace-gas detection by photothermal deflection spectroscopy," *Applied Physics Letters*, vol. 37, pp. 519-521, 1980.
- [10] W. B. Jackson, N. M. Amer, A. C. Boccara, and D. Fournier, "Photothermal deflection spectroscopy and detection," *Applied Optics*, vol. 20, pp. 1333-1344, 1981.

- [11] P. K. Kuo, M. J. Lin, C. B. Reyes, L. D. Favro, R. L. Thomas, D. S. Kim, S. Y. Zhang, L. J. Inglehart, D. Fournier, A. C. Boccara, and N. Yacoubi, "MIRAGE-EFFECT MEASUREMENT OF THERMAL-DIFFUSIVITY .1. EXPERIMENT," *Canadian Journal of Physics*, vol. 64, pp. 1165-1167, Sep 1986.
- [12] P. K. Kuo, E. D. Sandler, L. D. Favro, and R. L. Thomas, "MIRAGE-EFFECT MEASUREMENT OF THERMAL-DIFFUSIVITY .2. THEORY," *Canadian Journal of Physics*, vol. 64, pp. 1168-1171, Sep 1986.
- [13] A. Salazar, A. Sanchez-Lavega, and J. Fernandez, "Thermal diffusivity measurements in solids by the ``mirage" technique: Experimental results," *Journal of Applied Physics*, vol. 69, pp. 1216-1223, 1991.
- [14] T. R. Anthony, W. F. Banholzer, J. F. Fleischer, L. H. Wei, P. K. Kuo, R. L. Thomas, and R. W. Pryor, "THERMAL-DIFFUSIVITY OF ISOTOPICALLY ENRICHED C-12 DIAMOND," *Physical Review B*, vol. 42, pp. 1104-1111, Jul 1990.
- [15] H. Machlab, W. A. McGahan, and J. A. Woollam, "THERMAL-DIFFUSIVITY MEASUREMENTS BY PHOTOTHERMAL LASER-BEAM DEFLECTION (PTD) - DATA-ANALYSIS USING THE LEVENBERG-MARQUARDT ALGORITHM," *Thin Solid Films*, vol. 215, pp. 103-107, Jul 1992.
- [16] J. Rantala, L. Wei, P. K. Kuo, J. Jaarinen, M. Luukkala, and R. L. Thomas, "Determination of thermal diffusivity of low-diffusivity materials using the mirage method with multiparameter fitting," *Journal of Applied Physics*, vol. 73, pp. 2714-2723, 1993.
- [17] L. Wei, "Thermal property characterization of single crystal diamond with varying isotropic composition," in *Physics (Condensed Matter)*. vol. Ph.D. Detroit: Wayne State University, 1993.
- [18] E. J. Gonzalez, J. E. Bonevich, G. R. Stafford, G. White, and D. Josell, "Thermal transport through thin films: Mirage technique measurements on aluminum/titanium multilayers," *Journal of Materials Research*, vol. 15, pp. 764-771, 2000.

- [19] G. Rousset, F. Charbonnier, and F. Lepoutre, "INFLUENCE OF RADIATIVE AND CONVECTIVE TRANSFERS IN A PHOTOTHERMAL EXPERIMENT," *Journal of Applied Physics*, vol. 56, pp. 2093-2096, 1984.
- [20] W. A. McGahan and K. D. Cole, "Solutions of the heat conduction equation in multilayers for photothermal deflection experiments," *Journal of Applied Physics*, vol. 72, pp. 1362-1373, 1992.
- [21] B. C. Li and S. Y. Zhang, "The effect of interface resistances on thermal wave propagation in multi-layered samples," *Journal of Physics D-Applied Physics*, vol. 30, pp. 1447-1454, May 1997.
- [22] J. R. Foley, "Model-based estimation of the anisotropic thermal properties of materials from photothermal deflection spectroscopy data using Bayesian inference," Cornell University, Aug., 2007., 2007, pp. xvii, 353 leaves.
- [23] G. Chen, "Ballistic-diffusive equations for transient heat conduction from nano to macroscales," *Journal of Heat Transfer-Transactions of the Asme*, vol. 124, pp. 320-328, 2002.
- [24] D. G. Cahill, W. K. Ford, K. E. Goodson, G. D. Mahan, A. Majumdar, H. J. Maris, R. Merlin, and S. R. Phillpot, "Nanoscale thermal transport," *Journal of Applied Physics*, vol. 93, pp. 793-818, 2003.
- [25] D. G. Cahill, K. Goodson, and A. Majumdar, "Thermometry and Thermal Transport in Micro/Nanoscale Solid-State Devices and Structures," *Journal of Heat Transfer*, vol. 124, pp. 223-241, 2002.
- [26] M. D. Greenberg, *Advanced engineering mathematics*, 2nd ed. Upper Saddle River, N.J.: Prentice Hall, 1998.
- [27] J. S. C. Prentice, "Coherent, partially coherent and incoherent light absorption in thin-film multilayer structures," *Journal of Physics D-Applied Physics*, vol. 33, pp. 3139-3145, 2000.
- [28] A. W. Crook, "The Reflection and Transmission of Light by Any System of Parallel Isotropic Films," *Journal of the Optical Society of America*, vol. 38, pp. 954-964, 1948.

- [29] R. N. Bracewell, *The Fourier transform and its applications*, 3rd ed. Boston: McGraw Hill, 2000.
- [30] A. E. Siegman, "QUASI-FAST-HANKEL TRANSFORM FOR OPTICAL DIFFRACTION CALCULATIONS," *Journal of the Optical Society of America*, vol. 66, pp. 1132-1132, 1976.
- [31] Y. D. Chung, "Thermal property measurements," Cornell University, August, 1995., 1995, pp. xiii, 236 leaves.
- [32] P. K. Kuo, L. J. Inglehart, E. D. Sessler, M. J. Lin, L. D. Favro, and R. L. Thomas, *Review of Progress in Quantitative NDE* vol. 4B. New York: Plenum, 1985.
- [33] C. B. Reyes, "Thermal Wave Measurement of Thermal Diffusivity of Solids," in *Physics (Solid State)*. vol. Ph.D. Detroit, MI: Wayne State University, 1988.
- [34] A. P. Chojnacka, C. T. Avedisian, and A. Rendtel, "The thermal diffusivity of silicon nitride/silicon carbide nanocomposites using a photothermal deflection technique," *Proceedings of the Royal Society of London A*, vol. 455, pp. 2781-2802, 1999.
- [35] J. G. Hust and A. B. Lankford, "Research Materials 8420 and 8421: Electrolytic Iron: Thermal Conductivity and Electrical Resistivity as a Function of Temperature from 2 to 1000 K," National Bureau of Standards, Gaithersburg, MD1984.
- [36] J. G. Hust and A. B. Lankford, "Standard Reference Materials 1460, 1461, and 1462: Austenitic Stainless Steel Thermal Conductivity and Electrical Resistivity as a Function of Temperature from 2 to 1000 K," National Bureau of Standards, Washington, D.C.1984.
- [37] F. P. Incropera, *Introduction to heat transfer*, 5th ed. Hoboken, N.J.: J. Wiley, 2007.
- [38] D. W. Marquardt, "AN ALGORITHM FOR LEAST-SQUARES ESTIMATION OF NONLINEAR PARAMETERS," *Journal of the Society for Industrial and Applied Mathematics*, vol. 11, pp. 431-441, 1963.

- [39] M. Bertolotti, R. L. Voti, G. Liakhou, and C. Sibia, "ON THE PHOTODEFLECTION METHOD APPLIED TO LOW THERMAL-DIFFUSIVITY MEASUREMENTS," *Review of Scientific Instruments*, vol. 64, pp. 1576-1583, 1993.
- [40] C. J. Glassbrenner and G. A. Slack, "THERMAL CONDUCTIVITY OF SILICON + GERMANIUM FROM 3 DEGREES K TO MELTING POINT," *Physical Review a-General Physics*, vol. 134, pp. 1058-&, 1964.
- [41] J. C. Thompson and B. A. Younglove, "THERMAL CONDUCTIVITY OF SILICON AT LOW TEMPERATURES," *Journal of Physics and Chemistry of Solids*, vol. 20, pp. 146-149, 1961.

CHAPTER TWO

A maximum *a posteriori* non-linear least squares estimation algorithm
for the determination of thermal properties using PDS

1. Introduction

Thin films and multi-layer structures represent the cornerstone of micro and nano-scale technology. These films range from several atomic layers ($\sim 1 \text{ \AA} = 10^{-10} \text{ m}$) to several micrometers ($\sim 1 \text{ \mu m} = 10^{-6} \text{ m}$) in thickness. For many years, one of the limiting factors in the computer industry, as captured by Moore's Law [1], has been how thin a layer of silicon dioxide (SiO_2) can be deposited for use as a gate dielectric in a transistor. For example, Intel's current 65 nm chip architecture uses a SiO_2 film which is only 1.2 nm ($1 \text{ nm} = 10^{-9} \text{ m}$) thick, a mere five atomic layers [2]. Similarly thin multi-layered structures of alternating films have found extensive use in areas such as x-ray optics [3], vertical cavity surface emitting lasers (VCSELs) [4], and thermoelectrics [5].

Materials at such small length scales are known to have thermal properties which differ significantly from their bulk quantities due to confinement effects of the energy carriers (i.e. electrons and phonons) [6]. Significant reduction in thermal conductivity is expected, and has been observed [7, 8], when the thickness of a film is less than the mean free path of the energy carriers ($\sim 10 \text{ nm}$ for electrons in metals and $\sim 10\text{-}100 \text{ nm}$ for phonons in insulators and semiconductors) [9]. Thermal transport at these scales is most often analyzed using the Boltzmann or ballistic-diffusive equations [10, 11]. Conventional thermal design, however, uses continuum theories such as Fourier conduction for which we may identify macroscopic properties such as thermal conductivity and thermal diffusivity. It is clear that the continuum hypothesis is not satisfied at these small length-scales, but knowledge of "effective" properties which incorporate confinement and quantum effects is essential for engineering design.

We have previously developed a model (Chapter 1) for the temperature field and optical probe beam deflections of a periodically heated multi-layer structure which

has direct applications toward photothermal deflection spectroscopy (PDS). PDS, commonly referred to as the “mirage” [12] or “photothermal deflection” [13] technique, uses a modulated laser (i.e. heating beam) to periodically heat a material. Heat flow through the solid and into the surrounding gas phase causes deflections of a second laser (i.e. probe beam) which may be related to the thermal properties of the material. The concept is depicted schematically in Figure 2-1. The strength of PDS is its ability to confine the temperature field, effectively a thermal probe, to small length-scales by adjusting the modulation frequency of the applied heat source. This is also true of other “thermal wave” techniques such as photoacoustic spectroscopy [14], $3-\omega$ [15], modulated thermal reflectance [16], and scanning thermal microscopy [17]. These techniques are particularly useful in the study of thin films, since the thermal probe may be confined to the thin film or multi-layer structure, allowing maximum sensitivity to the region of interest. One of the limiting traits of PDS which prevents it from analyzing infinitesimally small thermal fields is that the probe beam is of finite size. Our ability to detect fluctuations in the thermal field diminishes as the field becomes small with respect to the size of the probe beam.

The principal measurement of PDS is the oscillatory deflection angle of the probe beam, which can be decomposed into orthogonal normal and tangential components. In order to determine the thermal properties of the material from these deflections, it is necessary to have an appropriate model of heat transfer in both the solid and gas phases. Our model incorporates the effects of anisotropic thermal conductivity and inter-layer thermal contact resistance on heat flow in an arbitrary multi-layer system. With this model in hand, we may estimate the properties of the material system by determining the suite of model parameters which allows for the best agreement between the measured and predicted probe beam deflections. This will be done by means of a maximum *a posteriori* non-linear least squares estimator.

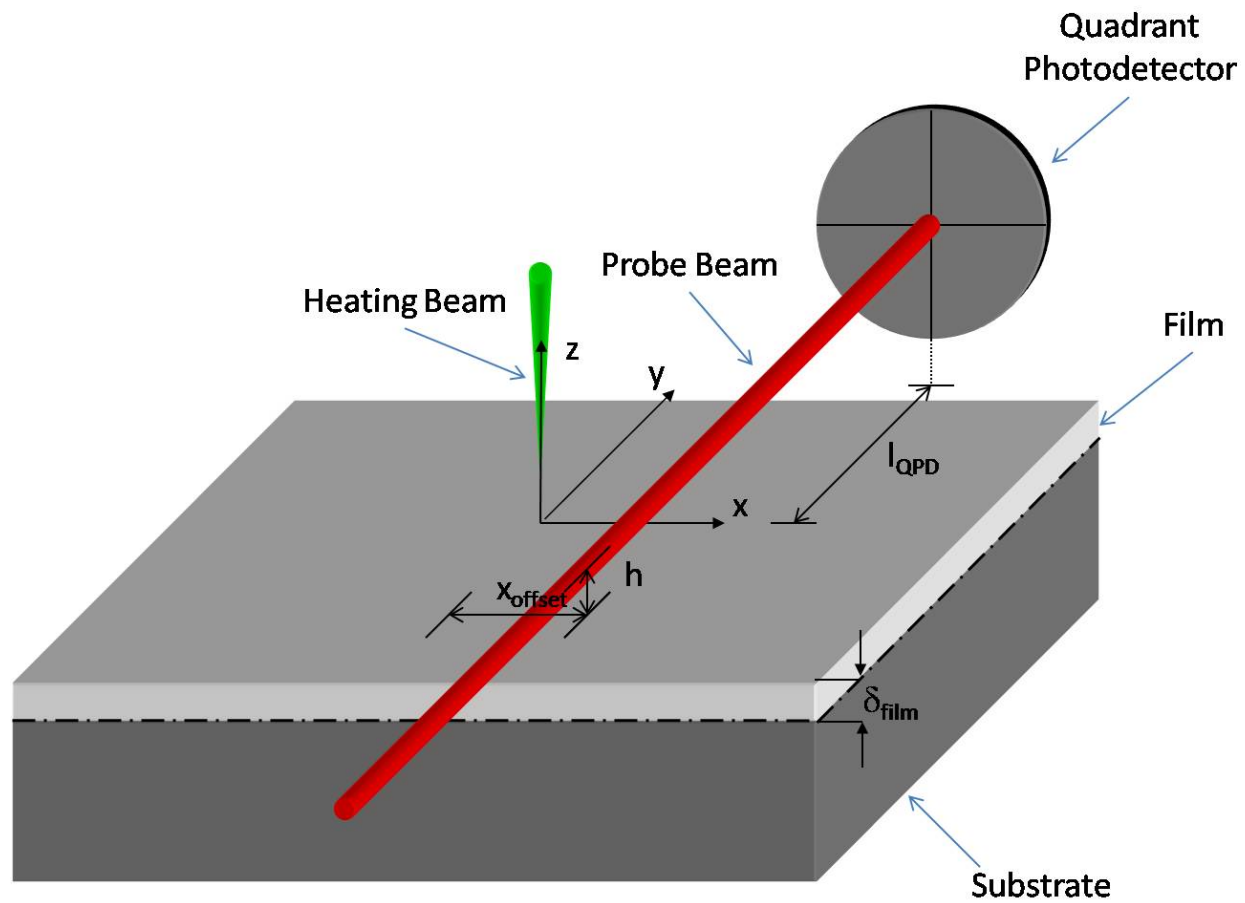


Figure 2-1: Schematic of transverse PDS concept

The objective of this chapter is the following: 1.) develop a maximum *a posteriori* estimation algorithm to determine the thermal properties and other model parameters from simulated PDS probe beam deflection data, 2.) develop a procedure to determine the thermal properties of a “black box” material system, 3.) examine the existence and uniqueness of the set of parameters resulting from the estimation algorithm.

2. Estimation Algorithm

Previous works relating to the estimation of thermal properties using PDS have used blanket statements such as “a curve fitting routine was used” or have provided only limited information about their multi-parameter fitting procedure [18-20]. Our intent is to clearly spell out the mechanics of our estimation algorithm so that it may be used as a reference for future work. This should not be seen as a contribution toward the well developed field of estimation [21, 22], but rather a particular application of using our model to extract thermal properties and other model parameters from PDS measurements. The flow-chart in Figure 2-2 will provide a useful tool for navigating the algorithm. We point out that that the algorithm presented here is general enough that it may be used for bulk materials, film-on-substrate, and multi-layer systems.

We begin by assuming that a measurement of the probe beam deflection ($\bar{\Phi}_{\text{meas},i}$) is equal to that computed by the model ($\bar{\Phi}_{\text{model},i}$) at the true set of model parameters (\mathbf{s}_{true}), in addition to some normally distributed measurement noise (w_i), such that

$$\bar{\Phi}_{\text{meas},i} = \bar{\Phi}_{\text{model},i}(\mathbf{s}_{\text{true}}) + w_i \quad 2.1.$$

The vector of model parameters (\mathbf{s}) may include any, or all of the following: thermal conductivity or diffusivity of each layer, anisotropy ratio of thermal conductivity in

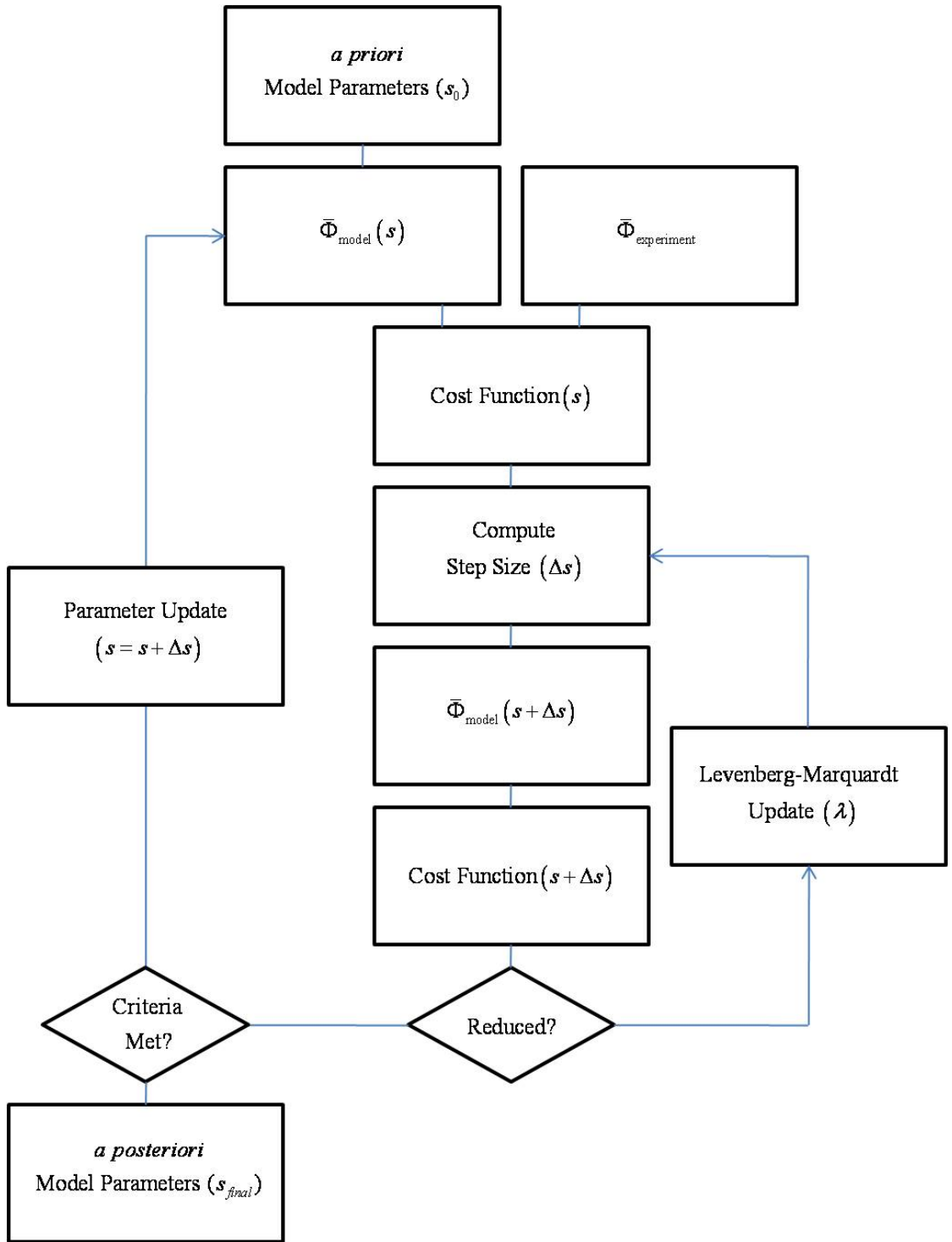


Figure 2-2: Flow chart of estimation algorithm

each layer, thermal contact resistance between adjacent layers, probe and heating beam parameters (e.g. R_p , R_h , P_h), and signal gain (or gain multiplier). A “full” treatment of the problem would include all possible parameters in the model. This, however, is prohibitively difficult and will not be done here.

From Bayes’ Rule [22], the probability density function (pdf) of a set of model parameters conditioned on a set of measurements is

$$p(\mathbf{s} | \bar{\Phi}_{meas}) = \left(\frac{|2\pi\mathbf{R}_w|^{1/2} |2\pi\mathbf{R}_{s_0}|^{1/2}}{p(\bar{\Phi}_{meas})} \right) e^{-\frac{1}{2}(\Delta'\mathbf{R}_w^{-1}\Delta + \Delta_0'\mathbf{R}_{s_0}^{-1}\Delta_0)} \quad 2.2.$$

For a maximum *a posteriori* estimator, we wish to determine the set of model parameters which maximizes the probability in Eq 2.2 (the uniqueness of this solution will be discussed later in this chapter). We may accomplish this by minimizing the argument of the exponential term. This leads us to define a scalar “cost function” as

$$CF(\mathbf{s}) = \frac{1}{2}(\Delta'\mathbf{R}_w^{-1}\Delta + \Delta_0'\mathbf{R}_{s_0}^{-1}\Delta_0) \quad 2.3.$$

Minimization of Eq 2.3 creates, in effect, a non-linear least squares problem which is weighted by the variance of the measurement noise and *a priori* parameter information. The first term in the cost function normalizes the difference between the measurements and the model (i.e. Δ , the residuals) by the level of measurement noise at each point. If the residuals are normally distributed, then we expect 95% of them to fall within $-2\sigma_{w,i} \leq \Delta_i \leq 2\sigma_{w,i}$ when evaluated at \mathbf{s}_{true} . The second term is a measure of how far the parameters are from their *a priori* values. It may be possible, perhaps by means of a secondary measurement, to have prior knowledge of the distribution of each parameter. This may include “perfect” knowledge, where $\sigma_s \rightarrow 0$, or “diffuse” knowledge, where $\sigma_s \rightarrow \infty$. Practically speaking, it makes no sense to estimate parameters for which you have perfect knowledge, but allowing for this term enables

the parameters to move slightly away from their *a priori* values during the estimation process.

Theoretically, it is possible to calculate the value of Eq 2.3 throughout the entire parameter space. This is, however, a computationally prohibitive task. The minima of the cost function is located at \mathbf{s}_{true} . At this point, $\nabla CF(\mathbf{s}_{true}) = 0$. We do not yet know the value of \mathbf{s}_{true} , but we will assume that it is a distance $\Delta\mathbf{s}$ from our current point in parameter space $\mathbf{s}_{current}$. In order to calculate the necessary step size, we linearize the gradient of the cost function by performing a Taylor series expansion about $\mathbf{s}_{current}$.

$$\nabla CF(\mathbf{s}_{true}) = \nabla CF(\mathbf{s}_{current} + \Delta\mathbf{s}) \approx \nabla CF\Big|_{\mathbf{s}_{current}} + \mathbf{H}(CF)\Big|_{\mathbf{s}_{current}} \Delta\mathbf{s} \quad 2.4,$$

where elements of the Hessian of the cost function are defined as

$$H_{ij}(CF) = \frac{\partial^2}{\partial s_i \partial s_j}(CF) \quad 2.5.$$

The step size may be computed by setting Eq 2.4 equal to zero, resulting in

$$\Delta\mathbf{s} = \left(\mathbf{J}'\mathbf{R}_w^{-1}\mathbf{J} - \Delta'\mathbf{R}_w^{-1}\mathbf{H}(\bar{\Phi}_{model}) + \mathbf{R}_{s_0}^{-1} \right)^{-1} \left(\mathbf{J}'\mathbf{R}_w^{-1}\Delta - \mathbf{R}_{s_0}^{-1}\Delta_0 \right) \quad 2.6.$$

Evaluation of the Jacobian matrix \mathbf{J} in Eq 2.6 is a critical step in this process.

Its elements are

$$J_{ij} = \frac{\partial}{\partial s_j} \bar{\Phi}_{model,i} \quad 2.7.$$

The Jacobian represents the sensitivity of the each point in the model to a change in each model parameter. Since our physical model may take on any number of embodiments, and the combination of parameters which we choose to estimate may differ, it is not productive for us to present a generalized analytical expression for the elements of this matrix. Instead, we compute it numerically using a forward-difference approximation

$$J_{ij} \approx \frac{\bar{\Phi}_{\text{model},i}(\chi s_j) - \bar{\Phi}_{\text{model},i}(s_j)}{(\chi s_j) - (s_j)} \quad 2.8,$$

where χ quantifies the step size. In practice, we typically use $\chi = 1.01$ for a 1% step size.

The Hessian of the model, $\mathbf{H}(\bar{\Phi}_{\text{model}})$ in Eq 2.6, is a computationally expensive operation to perform. Its elements are

$$H_{ijk}(\bar{\Phi}_{\text{model}}) = \frac{\partial^2}{\partial s_i \partial s_j} \bar{\Phi}_{\text{model},k} \quad 2.9.$$

We will neglect this term, however, by invoking the assumption that the residuals are “sufficiently small”, allowing us to reduce Eq 2.6 to

$$\Delta \mathbf{s} = \left(\mathbf{J}' \mathbf{R}_w^{-1} \mathbf{J} + \mathbf{R}_{s_0}^{-1} \right)^{-1} \left(\mathbf{J}' \mathbf{R}_w^{-1} \Delta - \mathbf{R}_{s_0}^{-1} \Delta_0 \right) \quad 2.10.$$

This is a poor assumption when $\mathbf{s}_{\text{current}}$ is far from \mathbf{s}_{true} , but we are simply using it as a tool to approach the point where the assumption becomes valid. This step size, referred to as a Gauss-Newton step, allows for a much more efficient calculation than Eq 2.6.

Since the cost function is a non-linear function of \mathbf{s} , we have no guarantee that the step size given by Eq 2.10 has either minimized or even reduced its value. To guarantee reduction of the cost function, we will implement a method developed by Levenberg & Marquardt [23]. We add a scalar parameter $\lambda \geq 0$ to Eq 2.10 such that

$$\Delta \mathbf{s} = \left(\mathbf{J}' \mathbf{R}_w^{-1} \mathbf{J} + \mathbf{R}_{s_0}^{-1} + \lambda \mathbf{I} \right)^{-1} \left(\mathbf{J}' \mathbf{R}_w^{-1} \Delta - \mathbf{R}_{s_0}^{-1} \Delta_0 \right) \quad 2.11.$$

A similar technique was implemented by Foley [24]. When $\lambda = 0$, we recover the Gauss-Newton step in Eq 2.10. As $\lambda \rightarrow \infty$, the step size follows the direction of “steepest descent”. The algorithm will preferentially step in the direction of the parameter which causes the greatest reduction in cost function. We generally initialize

the estimation algorithm with a small value, such as $\lambda = 10^{-3}$. Once the step size has been calculated, we check to see if the following condition has been met

$$CF(\mathbf{s} + \Delta\mathbf{s}) < CF(\mathbf{s}) \quad 2.12.$$

If Eq 2.12 is true, we decrease the value of λ ($\lambda_{new} = 0.1\lambda_{old}$) and update the parameters such that

$$\mathbf{s}_{new} = \mathbf{s}_{old} + \Delta\mathbf{s} \quad 2.13.$$

If Eq 2.12 is not true, we increase the value of λ ($\lambda_{new} = 10\lambda_{old}$) and re-compute the step size in Eq 2.11. Note that the factors of 0.1 and 10 are arbitrary and may be adjusted as necessary. Larger factors may speed convergence, but if they are too large, algorithm may not converge at all.

The process is terminated under the following conditions: 1.) the change in cost function is below a specified tolerance, 2.) the changes in parameter values are below a specified tolerance, 3.) the maximum number of iterations has been reached, or 4.) the maximum number of λ updates has been reached.

2.1 Posterior Results

The estimation algorithm does not produce a single-valued result for each of the parameters, but rather a mean and standard deviation which may be used to define the posterior pdf of each parameter. The mean value is reported as \mathbf{s}_{final} . The covariance of the estimation error is

$$\mathbf{R}_s = \left(\mathbf{J}'\mathbf{R}_w^{-1}\mathbf{J} + \mathbf{R}_{s_0}^{-1} \right)^{-1} \quad 2.14.$$

The posterior standard deviation of each parameter is the square root of the diagonal elements in Eq 2.14.

$$\sigma_{s,i} = \sqrt{R_{s,ii}} \quad 2.15.$$

Large values of $\sigma_{s,i}$ represent poor knowledge of a particular estimated parameter. Due to our inclusion of *a priori* information, however, it is not possible to have worse knowledge of a parameter than that which we initially had (although it does not necessarily improve).

The correlation between any two parameters is

$$\rho_{ij} = \frac{R_{s,ij}}{\sqrt{R_{s,ii}R_{s,jj}}} \quad 2.16.$$

This parameter is useful in helping us determine linear combinations of parameters in the model. Values of $\rho_{ij} \approx \pm 1$ indicate parameters which are tightly coupled in the model. A value of $\rho_{ij} = 1$ indicates that two parameters have the same effect on the model, while a value of $\rho_{ij} = -1$ indicates that they have the opposite effect. In such cases, it may not be possible to determine a unique set of parameters which minimize the cost function.

From the standpoint of estimation, observability refers to an algorithm's ability to uniquely and unambiguously determine each of the parameters in \mathbf{s} . If our system is not observable, there are two possibilities: 1.) a parameter (or several) has no effect on the measurements (i.e. the measurements are insensitive to changes in that parameter), or 2.) a linear combination of two (or more) parameters influence the measurement in the same way as one parameter alone.

According to the method of Ham and Brown [25], we may examine the eigenvalues and eigenvectors of a scaled version of Eq 2.16 to determine the observability of the system. We will define

$$\mathbf{p}_{scaled} \equiv \frac{N_s}{\text{trace}(\mathbf{p})} \mathbf{p} \quad 2.17,$$

where N_s is the number of parameters in \mathbf{s} . The eigenvectors of \mathbf{p}_{scaled} are related to the variance of the model parameters in such a way that smaller eigenvalues indicate a

more observable system. The eigenvector associated with the smallest eigenvalue indicates the “direction” in parameter space associated with the highest degree of observability. Elements in the eigenvector that are of comparable magnitude indicate a linear combination of parameters, rather than a single parameter, that is highly observable. In such a case, we must either combine these parameters into a new one, or assume a fixed value of the parameter (e.g. set its *a priori* uncertainty to zero or remove it from \mathbf{s}). The best circumstance is when the most observable direction in parameter space is the single parameter you are most interested in determining.

2.2 Uniform Noise

In the event of uniform measurement noise, the posterior pdf in Eq 2.2 is

$$p(\mathbf{s} | \bar{\Phi}_{\text{meas}}) = \left(\frac{1}{\sqrt{2\pi}\sigma_w} \frac{|2\pi\mathbf{R}_{s_0}|^{1/2}}{p(\bar{\Phi}_{\text{meas}})} \right) e^{-\frac{1}{2\sigma_w^2}(\Delta'\Delta + \sigma_w^2\Delta_0'\mathbf{R}_{s_0}^{-1}\Delta_0)} \quad 2.18.$$

In this case, the cost function in Eq 2.3 becomes

$$CF(\mathbf{s}) = \frac{1}{2\sigma_w^2} (\Delta'\Delta + \sigma_w^2\Delta_0'\mathbf{R}_{s_0}^{-1}\Delta_0) \quad 2.19.$$

The step-size in Eq 2.11 becomes

$$\Delta\mathbf{s} = (\mathbf{J}'\mathbf{J} + \sigma_w^2\mathbf{R}_{s_0}^{-1} + \lambda\mathbf{I})^{-1} (\mathbf{J}'\Delta - \sigma_w^2\mathbf{R}_{s_0}^{-1}\Delta_0) \quad 2.20.$$

The posterior parameter covariance in Eq 2.14 becomes

$$\mathbf{R}_s = \sigma_w^2 (\mathbf{J}'\mathbf{J} + \sigma_w^2\mathbf{R}_{s_0}^{-1})^{-1} \quad 2.21.$$

In order to test the algorithm, we will generate “truth model” data. This data will contain no additional noise other than the small contribution from discretization and digitization error. We observe that, as $\sigma_w \rightarrow 0$, the pdf in Eq 2.18 takes on the form of a Dirac delta function. There is zero probability that the parameters can exist anywhere but the location where they are at their true value. Similarly, the cost function in Eq 2.19 takes on a value of infinity unless the residuals are identically

zero. Since our objective is the minimization of the cost function, and we cannot effectively deal with values of infinity, we must re-define the cost function for the case when $\sigma_w \rightarrow 0$ (or when CF is computationally equivalent to infinity) as

$$CF(\mathbf{s}) = (\Delta' \Delta) \tag{2.22}$$

This reduces the problem, in effect, to an un-weighted non-linear least squares problem.

In the case of zero measurement noise, we also find that the step size in Eq 2.20 loses the influence of *a priori* information, and the posterior covariance in Eq 2.21 tends to zero. Essentially, all of these results indicate that one should have perfect knowledge of model parameters. The reason why we will test the estimator using such data is to determine whether it is able to converge to the true set of parameters from any initial guess. If it does not, it is possible that the algorithm has locked onto a local (rather than global) minima of the cost function, or that a condition has been encountered such that two (or more) parameters are perfectly correlated and the system becomes unobservable. If our algorithm is unable to determine the desired properties using perfect data, it certainly will not work for real data, which suffers from noise and other factors (e.g. temperature dependant properties, thermo-elastic effects) which are not included in our model.

In order to determine the quality of the estimated results, we may re-evaluate Eq 2.21 in the absence of prior information to obtain the normalized posterior covariance as

$$\frac{1}{\sigma_w^2} \mathbf{R}_s = (\mathbf{J}'\mathbf{J})^{-1} \tag{2.23}$$

The normalized posterior standard deviation of the parameters is the square root of the diagonal terms in Eq 2.23,

$$\frac{\sigma_{s,i}}{\sigma_w} = \sqrt{\frac{1}{\sigma_w^2} R_{s,ii}} \quad 2.24.$$

2.3 Scaling

The sensitivity of the measurements to each parameter may differ by many orders of magnitude. For example, since the probe beam radius is of the order 10^{-5} m and the thermal conductivity may be of the order 10^2 W/m-K, we may assume that $|\partial\bar{\Phi}_{\text{model}}/\partial R_p| \gg |\partial\bar{\Phi}_{\text{model}}/\partial k_z|$. A change of 1 m in probe beam radius is much more dramatic than a change of 1 W/m-K in thermal conductivity. Because of this, it is prudent to utilize a scaling algorithm which makes the columns of the Jacobian matrix of comparable size. This is particularly important in the computation of the matrix inverse in Eq 2.11, which may be ill-conditioned without appropriate scaling. We will use a scaling matrix \mathbf{D} such that its diagonal elements are the maximum value from each corresponding column of the Jacobian matrix.

$$D_{ii} = \max(J_{ji}) \quad 2.25.$$

Scaling definitions can be found in the nomenclature. The scaled step size becomes [26]

$$\Delta\bar{\mathbf{s}} \equiv \mathbf{D}\Delta\mathbf{s} = \left(\bar{\mathbf{J}}\mathbf{R}_w^{-1}\bar{\mathbf{J}} + \bar{\mathbf{R}}_{s_0}^{-1} + \lambda\mathbf{D}^{-1}\mathbf{D}^{-1}\right)^{-1} \left(\bar{\mathbf{J}}\mathbf{R}_w^{-1}\Delta - \bar{\mathbf{R}}_{s_0}^{-1}\Delta_0\right) \quad 2.26.$$

The physical step size from Eq 2.11 may be re-expressed using scaled quantities as

$$\Delta\mathbf{s} = \mathbf{D}^{-1}\Delta\bar{\mathbf{s}} \quad 2.27.$$

The covariance of the measurement error from Eq 2.14 may be re-expressed using scaled quantities as

$$\mathbf{R}_s = \mathbf{D}^{-1} \left(\bar{\mathbf{J}}\mathbf{R}_w^{-1}\bar{\mathbf{J}} + \bar{\mathbf{R}}_{s_0}^{-1}\right)^{-1} \mathbf{D}^{-1} \quad 2.28.$$

2.4 Pre-Processing Data

In order to prepare the data for the estimation algorithm, it is necessary to perform several pre-processing steps.

Step 1: Removing Offsets

The data acquired from the lock-in amplifier has offsets which are difficult to remove using hardware. To remove them using software, we manually select several data points which are far from the influence of the thermal field. The mean of these far-field measurements is taken, and then subtracted from the measurements. This procedure is performed for the real and imaginary components of the tangential and normal (if applicable) probe beam deflections

Step 2: Determine Measurement Noise

The measurements contain some random variation resulting from thermal, electronic, and mechanical noise sources. To quantify this noise, we calculate the standard deviation of the data points selected in Step 1. Although it would be preferred, we do not readily have the ability to acquire an *in situ* estimate of measurement noise at each data point (as it would significantly increase the time of the experiment). This procedure is performed for the real and imaginary components of the tangential and normal (if applicable) probe beam deflections.

Step 3: Removing Position Error

Although we go to great lengths to align the experiment, there is some finite positional error due to backlash in the linear actuators. The position of $x_{\text{offset}} = 0$ may be accurately determined by locating the position at which the real and imaginary components of the tangential probe beam deflections pass through zero (after the offsets have been removed). The data is shifted accordingly.

Step 4: Interpolating Position Data

In the estimation algorithm, it is necessary for the model and measurements to be evaluated at the same locations. Due to the resolution of the linear actuators, there are small fluctuations ($\ll 1 \mu\text{m}$) in position about the desired measurement location.

We linearly interpolate the data between two adjacent points in order to determine the value at the desired measurement location.

Step 5: Phase Nulling

The electronic amplifiers introduce phase shifts to our measurements that are a function of frequency. This shift is primarily due to the high impedance amplifiers used in the quadrant photodetector [27]. We have not quantified these shifts in our experimental apparatus, but we may remove their effect by setting a reference phase of zero at $x_{\text{offset}} = 0$. As shown in Figure 2-3, we determine the slope of the tangential probe beam deflections in the complex plane and uniformly rotate the data by an angle ϕ_{rotate} such that the central-most points are horizontal (i.e. purely real) in the complex plane. Theoretically, any reference phase (e.g. $\phi = 45^\circ$ at $x_{\text{offset}} = 0$) may be used as long as it is uniform. This operation is performed on the data during pre-processing and on the model for each intermediate calculation of probe beam deflections.

Our model predicts a phase shift due to frequency-dependent temperature gradients alone (Figure 2-4), but we are unable to separate this effect from that of the electronic phase shift. It is possible that we are losing “information” by performing this phase-nulling operation. The operation maintains the point-to-point phase shift at each individual frequency, but removes the relative inter-frequency phase shift. The phase-nulled counterpart to Figure 2-4 is provided in Figure 2-5. A recommendation for future work is to quantify the electronically introduced phase shift and incorporate its effect into the model.

Historically, this phase-nulling operation was used for the zero-crossing method [19, 28, 29] to identify the offset position where the tangential probe beam deflections have a phase which is $\pi/2 \text{ rad}$ different from the aligned position. The slope of this distance plotted against $1/\sqrt{f}$ can be related to the thermal diffusivity of bulk materials.

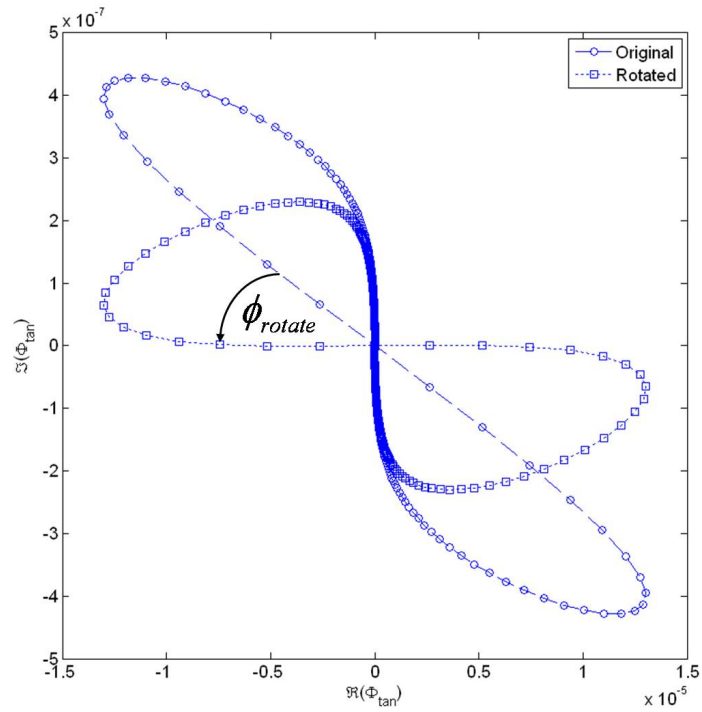


Figure 2-3: Phase-nulling operation on the tangential probe beam deflections

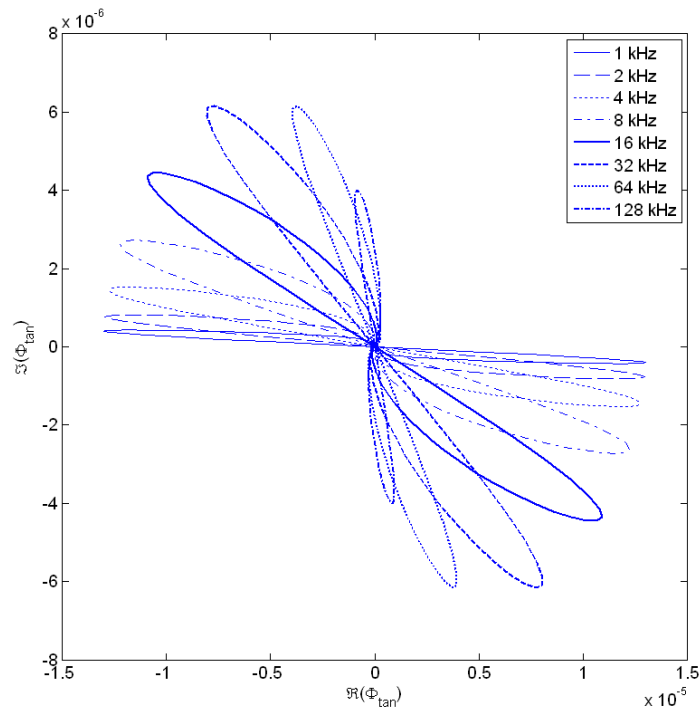


Figure 2-4: Simulated PDS data at several frequencies prior to phase-nulling operation

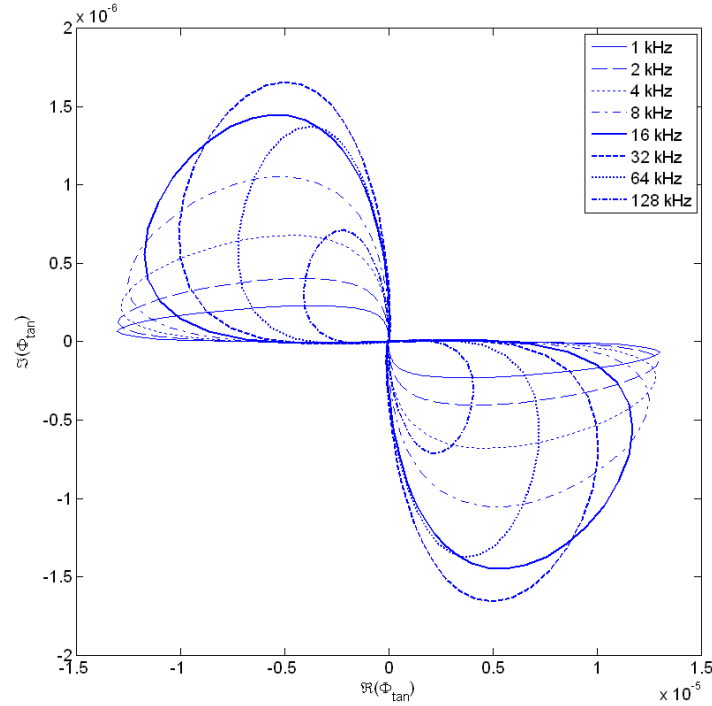


Figure 2-5: Simulated PDS data at several frequencies after phase-nulling operation

Step 6: Assembly

In the estimation algorithm, we will analyze data taken at multiple frequencies simultaneously. In order to assemble the necessary data vector, we append the pre-processed data taken at each individual frequency in the appropriate order. The resulting data vector will be of the form

$$\bar{\Phi}_{meas,model} = \left\{ \text{Re}[\bar{\Phi}_{\tan}(f_1)]; \dots; \text{Re}[\bar{\Phi}_{\tan}(f_N)]; \text{Im}[\bar{\Phi}_{\tan}(f_1)]; \dots; \text{Im}[\bar{\Phi}_{\tan}(f_N)] \right\} \quad 2.29.$$

There are several other possible assembly techniques which could be used, consisting of various combinations of the real and imaginary components, magnitude, and phase of the probe beam deflections. We prefer this method since the real and imaginary components allow for the calculation of both the magnitude and phase of the data. They are also of comparable magnitude, while the phase is bound by significantly larger values of $-\pi \leq \phi \leq \pi$. We believe that this would artificially skew the

estimator to preferentially favor the phase representation over the real, imaginary, or magnitude representations of the probe beam deflections. Regardless of assembly order, the most critical aspect is to ensure that the model output is assembled in the same way as the data.

3. Multi-Frequency Analysis

Ideally, the estimation algorithm would be able to converge to the true set of parameters under any set of conditions from any reasonable initial guess. We know from experience, however, that this does not always occur. We would like to develop a technique which offers some ability to aid in convergence, observability, and accuracy of the results.

One of the strengths of PDS is its ability to control the penetration depth of a thermal wave by adjusting the modulation frequency of the applied heat source. At very low frequencies, the thermal wave propagates deep into the substrate of a film-on-substrate system (Figure 2-6, left). At this condition, we expect probe beam deflections to be most sensitive to the properties of the substrate rather than those of the film. At high frequencies, we can constrain the thermal field to within the film, but the size of the field becomes very small in contrast to the size of the probe beam (Figure 2-6, right). We will show that there is a substantial benefit to estimating properties by simultaneously processing measurements at multiple frequencies. Such measurements will contain “information” contained at either extreme.

We model the system depicted in Figure 2-7 consisting of the following: a 100 nm Tungsten (W) film used as an optical absorption layer, a 1 μm SiO_2 film, and a semi-infinite Si substrate. The properties used to model these materials are found in

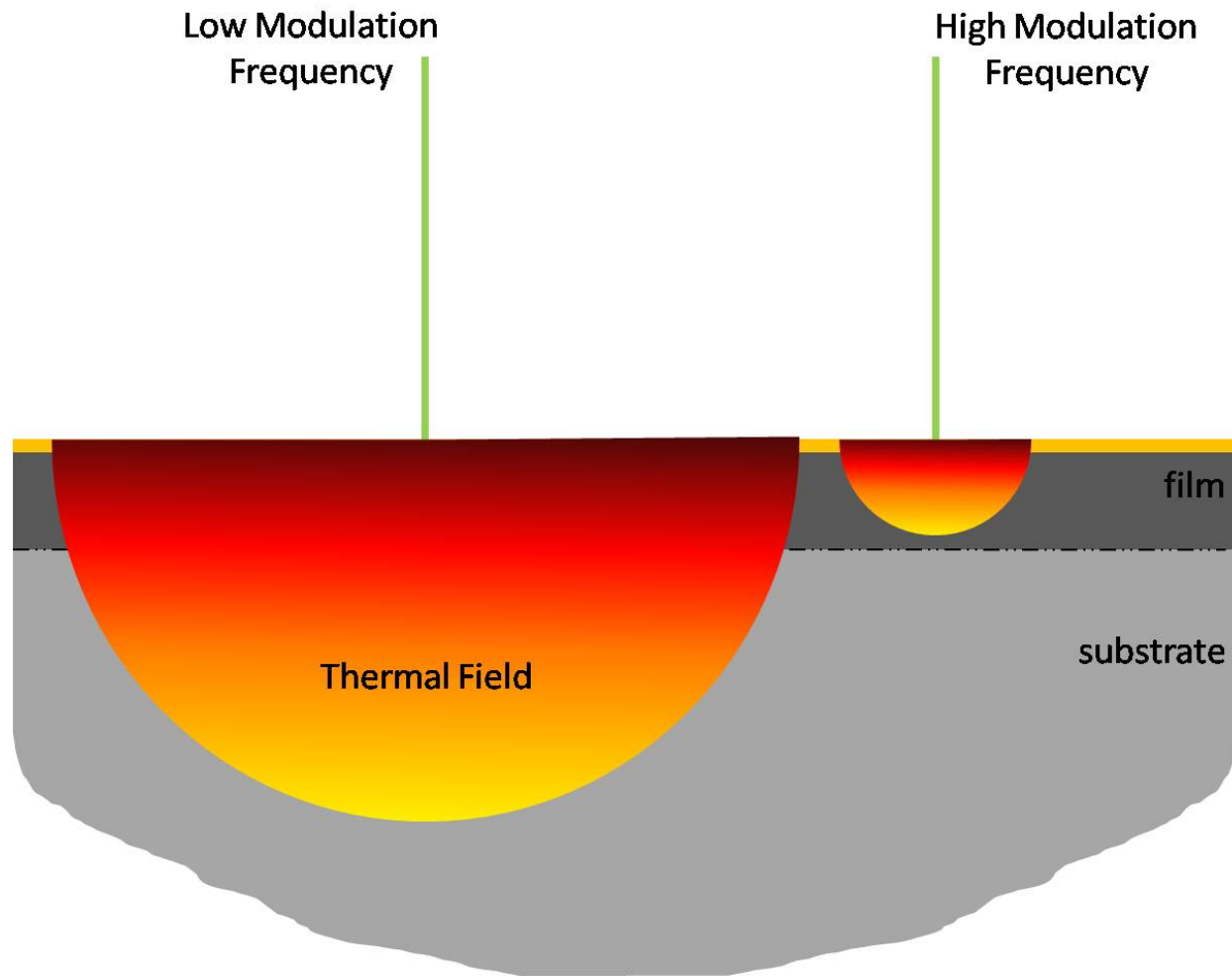


Figure 2-6: Schematic of thermal penetration dependence on heating beam modulation frequency

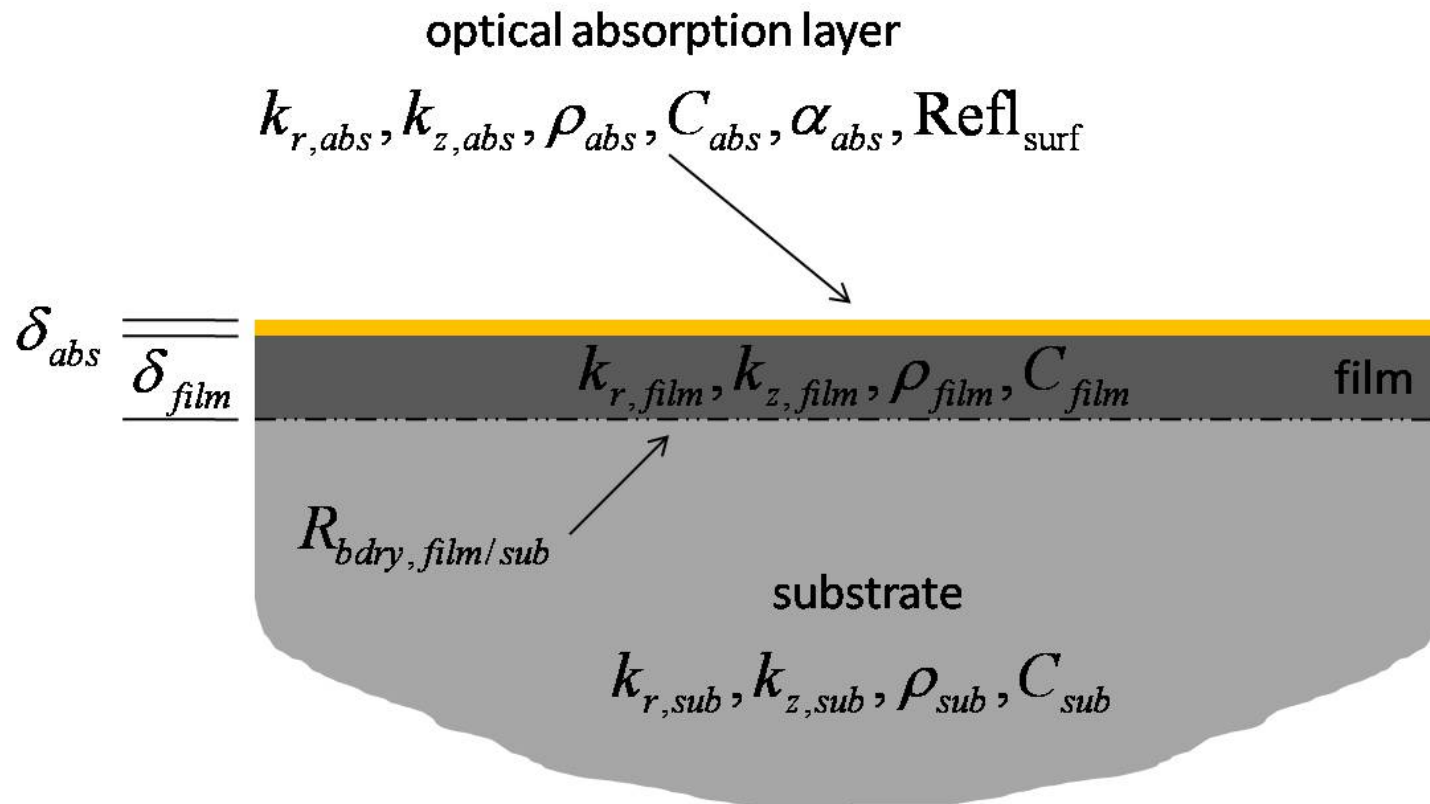


Figure 2-7: Multi-layer model applied to a film-on-substrate system with an optical absorption layer

Table 2-1 [30]. Furthermore, a thermal contact resistance of $10^{-6} \text{ m}^2\text{-K/W}$ will be modeled between the film and substrate. This value was chosen since it is close to the 1-D thermal resistance of a $1 \text{ }\mu\text{m}$ SiO_2 film assuming bulk properties ($\delta_{film}/k_{film} = 7.25 \times 10^{-7} \text{ m}^2 - \text{K} / \text{W}$). Therefore, it can neither be considered dominant or negligible in contrast to the resistance of the film alone.

The one-dimensional thermal penetration depth is (c.f. Eq 1-20)

$$l_{pd} = \sqrt{\frac{1}{\pi f} \frac{k_z}{\rho C}} \quad 2.30.$$

In order for the SiO_2 film to be considered “thermally thin”, we will select a frequency of 2.656 kHz such that $\delta_{film}/l_{pd} = 0.1$. In order for the film to be considered “thermally thick”, we will select a frequency of 26.56 MHz such that $\delta_{film}/l_{pd} = 10$.

We note, in advance, that the latter condition is not a practically attainable frequency from an experimental standpoint (due to amplification and signal strength issues), but since our current analysis is based in simulation, it remains useful to demonstrate our point. For our multi-frequency approach, we will select frequencies and relative film thicknesses according to Table 2-2.

In order to determine the extent to which the system is observable at each of these three (i.e. low frequency, high frequency, and multi-frequency) conditions, we will calculate the posterior parameter standard deviation in Eq 2.24 (Table 2-3) and the associated correlation matrix in Eq 2.16 (Tables 2-4 through 2-6). The parameter vector will be $\mathbf{s} = \left[k_{z,film}, (k_r/k_z)_{film}, R_{bdry}, R_p, G_{mult} \right]$. We will assume no prior knowledge of their parameter distributions ($\sigma_{s,i} \rightarrow \infty$). All other model parameters (e.g. those of the absorption layer, substrate, and gas phase) are assumed to be known precisely. We note that no actual parameter estimation is being performed in this section. We are only calculating the uncertainty at the true set of parameters (since they are known). Trial estimation runs will be performed in Section 4.

Table 2-1: Bulk properties @ 300K [30]

Property	Air	W	SiO₂	Si
ρ [kg/m ³]	1.1614	19300	2220	2330
C [J/kg-K]	1007	132	745	712
k [W/m-K]	0.0263	174	1.38	148

Table 2-2: Relative thermal penetration depths and frequency selection used for multi-frequency validation

δ_{film}/l_{tpd}	f [Hz]
0.1	2.656x10 ³
0.2	10.624x10 ³
0.5	66.399x10 ³
1	265.6x10 ³
2	1.0624x10 ⁶
5	6.6399x10 ⁶
10	26.56x10 ⁶

The results in Table 2-3 provide the normalized standard deviation of the parameters that would be calculated if the estimator had converged to \mathbf{s}_{true} . For example, at the low-frequency condition, we report that $\frac{1}{\sigma_w} \left(\frac{\sigma_{k_r}}{k_r} \right) = 3.47 \times 10^4$. If we wish to have a relative uncertainty of $\frac{\sigma_{k_r}}{k_r} = 10\%$, the level of noise must be $\sigma_w = 2.88 \times 10^{-6}$. In our PDS experiment, both the signal and noise level have non-dimensional units of $\frac{(V_{diff}/V_{sum})}{rad} \times rad$, where the first term represents a normalized calibration constant and the second term represents the angular deflections of the probe beam. Using lock-in amplifier techniques, it is possible to “custom tailor” the noise level by choosing longer time constants. Lower levels of noise come at the expensive of longer measurements. The equivalent noise bandwidth (ENBW) of our lock-in amplifier is $1/8\tau$, where τ is the time constant. In practice, we use a time constant of 1 sec.

At the lowest frequency condition (i.e. 2.656 kHz), the film may be considered thermally thin. Much of the heat flow will be in the substrate, and we expect that the details of the film structure will not be the major contributor toward the probe beam deflections. Figure 2-8 and Table 2-3 show us that the lowest normalized uncertainty is attained for the probe beam radius and gain multiplier. Although this is not a negative result, we are likely to already have a good *a priori* estimate of these parameters. Comparing the remaining three parameters, we see that the thermal contact resistance has the lowest uncertainty, followed by cross-plane thermal conductivity and anisotropy ratio. Figure 2-9 and Table 2-4 show the cross-correlation values for anisotropy ratio, thermal contact resistance, and gain with respect to cross-plane thermal conductivity. The greatest concern with the low frequency case is the

Table 2-3: Normalized relative uncertainty for multi-frequency validation

	$\frac{1}{\sigma_w} \left(\frac{\sigma_s}{s} \right)$		
Modulation Frequency	2.656 kHz	26.56 MHz	Multi
k_z (W/m-K)	3.47×10^4	1.04×10^{11}	4.97×10^3
k_r/k_z	1.37×10^5	6.93×10^{12}	2.10×10^4
R_{bdry} (m²-K/W)	2.32×10^4	2.90×10^{15}	1.17×10^3
R_p (m)	7.13×10^2	1.13×10^7	1.42×10^2
Gain (rad⁻¹)	2.83×10^3	1.47×10^{10}	1.37×10^3

Table 2-4: Correlation matrix for f = 2.656 kHz

ρ_{ij}	k_z	k_r/k_z	R_{bdry}	R_p	Gain
k_z	1	-0.77	0.98	0.59	0.41
k_r/k_z		1	-0.75	-0.91	-0.33
R_{bdry}			1	0.50	0.21
R_p				1	0.58
Gain					1

Table 2-5: Correlation matrix for f = 26.56 MHz

ρ_{ij}	k_z	k_r/k_z	R_{bdry}	R_p	Gain
k_z	1	1.00	-0.12	1.00	1.00
k_r/k_z		1	-0.12	1.00	1.00
R_{bdry}			1	-0.12	-0.12
R_p				1	1.00
Gain					1

Table 2-6: Correlation matrix for multi-frequency

ρ_{ij}	k_z	k_r/k_z	R_{bdry}	R_p	Gain
k_z	1	0.35	0.87	0.36	0.98
k_r/k_z		1	0.53	-0.63	0.24
R_{bdry}			1	0.02	0.75
R_p				1	0.50
Gain					1

extremely high degree of correlation between thermal contact resistance and cross-plane thermal conductivity ($\rho_{k_z, R_{bdry}} = 0.98$). This is not unexpected, however, as low frequencies are the least likely to resolve the features of the film due to the large thermal penetration depth. We will use this case as a baseline for comparison with the other cases.

We anticipate that the high frequency condition might dissociate the cross-plane thermal conductivity from the thermal contact resistance. This is because the thermal wave is confined within the film and is minimally affected by the presence of the contact resistance. Unfortunately, the length-scale of the thermal field will be on the order of 0.1 μm at this condition, while our probe beam has a radius of 23.9 μm . Our probe is not nearly small enough to pick up the fine detail in the thermal field. This becomes clear by observing the extremely large uncertainty in all parameters at the high frequency condition in Figure 2-8 and Table 2-3. The correlation matrix (Table 2-5) is even more disturbing, in that it contains many values of unity. The cross-plane thermal conductivity alone is identically correlated to anisotropy, probe beam radius, and signal gain. It is evident, however, that our initial desire to uncouple the effects of thermal conductivity and contact resistance was successful, with $\rho_{k_z, R_{bdry}} = -0.12$. Other than this uncoupling effect, however, the results at this frequency have little value to us.

More insight can be found into this condition by analyzing the eigenvalues and eigenvectors (Table 2-7) to the scaled correlation matrix from Eq 2.17. Again, the smallest eigenvalue represents the state of the system with the highest degree of observability. The eigenvector associated with this state indicates the direction of maximum observability in parameter space. It is clear that even in its most observable state, there is a linear combination of thermal conductivity and signal gain (i.e. the 1st

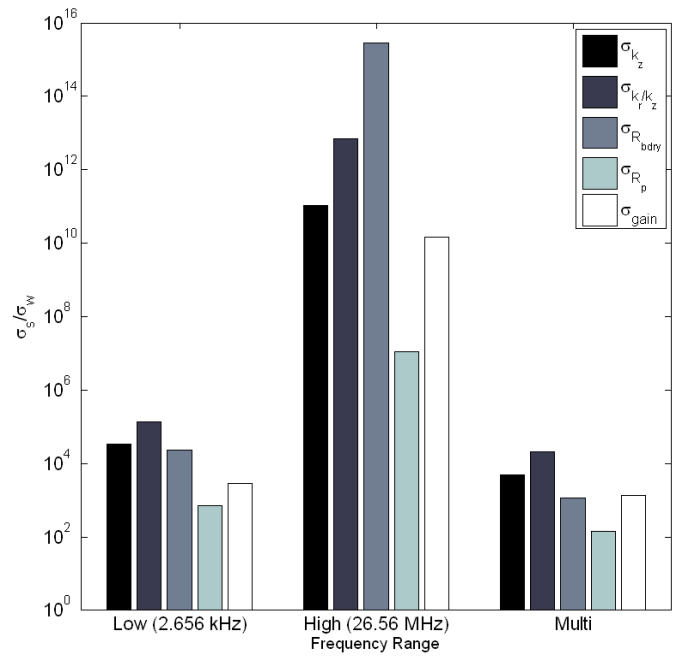


Figure 2-8: Normalized relative uncertainty of estimation parameters for low frequency, high frequency, and multi-frequency data from a simulated film-on-substrate system

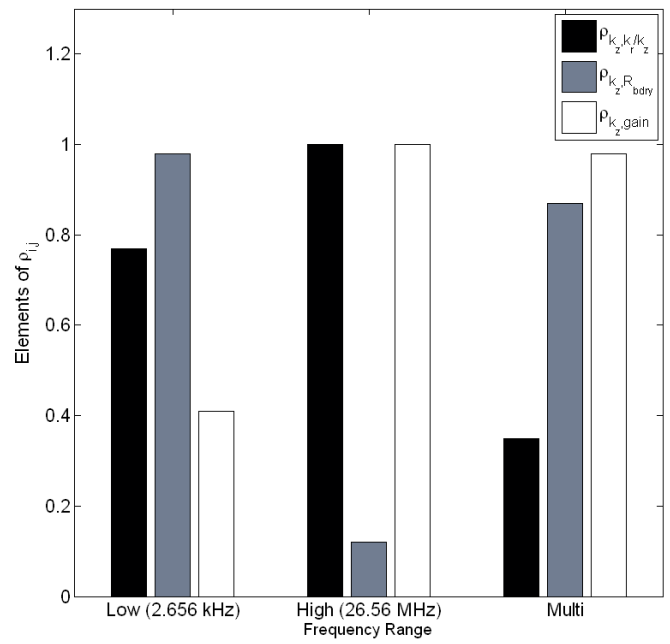


Figure 2-9: Elements of the correlation matrix for low frequency, high frequency, and multi-frequency data from a simulated film-on-substrate system

and 5th elements) to which the system is most observable, and the system is least observable for contact resistance (i.e. the 3rd element).

Table 2-7: Eigenvalue and eigenvectors for scaled correlation matrix in high frequency analysis

Parameter	Eigenvalues	4.02	0.981	9.09x10 ⁻⁵	2.73x10 ⁻⁶	3.91x10 ⁻¹¹
k_z	Eigenvectors	0.498	-0.0391	0.313	0.389	0.707
k_r/k_z		0.498	-0.0392	0.240	-0.832	-0.00145
R_{bdry}		0.0785	-0.997	2.55x10 ⁻⁴	6.25x10 ⁻⁵	1.25x10 ⁻⁵
R_p		0.498	-0.0395	-0.865	0.0513	0.00125
Gain		0.498	-0.0392	0.311	0.391	-0.707

Our initial hypothesis is confirmed by the results of the multi-frequency analysis. The normalized relative uncertainty results in Figure 2-8 and Table 2-3 show improvement by nearly an order of magnitude for thermal conductivity, anisotropy ratio, and contact resistance over the low frequency results. Furthermore, we have significantly de-coupled thermal conductivity from contact resistance, with $\rho_{k_z, R_{bdry}} = 0.87$ (Figure 2-9 and Table 2-6). The only downfall of this technique is that we have increased the correlation between thermal conductivity and gain multiplier. Fortunately, we have a good *a priori* estimate of the value for signal gain, which will effectively decouple these two parameters. We conclude that the multi-frequency approach has the benefit of providing better (i.e. lower uncertainty) parameter estimates and the ability to decouple parameters which are highly correlated in either the high frequency or low frequency regimes.

4. “Black Box” Estimation Procedure

In Section 3, we had the benefit of knowing the true set of parameters used in the model. This will not be the case in any realistic analysis of a material system. Even if we know the bulk properties, the values for a thin film may be substantially different. We must therefore develop a sufficiently robust procedure that will allow for the determination of thermal properties for any thin film system. The system we wish to analyze is shown in Figure 2-7, where the properties of the film and its interface with the substrate are unknown.

Since the properties of the “black box” film are unknown, it is not possible to select modulation frequencies according to relative thermal penetration depths. We still believe, however, that the multi-frequency approach provides us with more valuable information than a single frequency alone. Experimentally, our electronic amplification system limits us to modulation frequencies on the order of 100 kHz before the signal-to-noise ratio becomes prohibitively small. On the low end, a frequency of 1 kHz leads to a one-dimensional thermal penetration depth of 10’s of μm in low diffusivity materials such as SiO_2 . This length-scale will only increase in higher diffusivity materials. We therefore propose a frequency doubling scheme which includes $f = 1, 2, 4, 8, 16, 32, 64,$ and 128 kHz.

Originally in Eq 2.10, we employed the assumption that the residuals were “sufficiently small”. Starting from any arbitrary point in parameter space, however, this is likely not the case. The measurements and the model may, in fact, be separated by several orders of magnitude. In light of this, it is necessary to take an initial step to reduce the residuals to the point where this assumption becomes better. We accomplish this by fixing all model parameters at their *a priori* estimate, with the exception of the cross-plane thermal conductivity of the film, which we allow to “float”. We initially assume that the film is isotropic ($k_r = k_z$) and that there is no thermal contact resistance between the film and the substrate ($R_{\text{bdry}} = 0$). The result of

this is an estimate for thermal conductivity which minimizes the difference between the model and the measurements with all other parameters fixed. We do not claim that this is the true value for thermal conductivity, since our *a priori* estimates of other model parameters may be incorrect.

In the next step, we allow multiple parameters to float simultaneously. For the thermal conductivity, we use an initial guess resulting from the previous step with a “diffuse” prior uncertainty (i.e. $\sigma_{k_z} \rightarrow \infty$). For the anisotropy ratio, we use an initial guess of $k_r/k_z = 1$ and a diffuse prior. For the thermal contact resistance, we use an initial guess of $R_{bdry} = 10^{-6} \text{ m}^2 - K / W$ (our forward difference computation of the Jacobian in Eq 2.8 is not possible for $R_{bdry} = 0$) and a diffuse prior. For the probe beam radius and gain multiplier, we will use appropriate *a priori* estimates which come from calibration or external measurement.

After running the multi-parameter estimation, it is important to examine the posterior results discussed in Section 2.1. We first examine the correlation matrix defined in Eq 2.16 to determine which parameters, if any, are highly correlated. There is no specific value at which the algorithm “breaks down”, but values of $\rho_{ij} \approx \pm 1$ indicate that the results may be questionable. We also look for parameters with a very high uncertainty. This is a strong indication that the model is insensitive to this parameter at the current set of conditions.

4.1 Test Case

In order to test our procedure for determining the properties of a black-box material system, we will generate simulated probe beam deflections for the system depicted in Figure 7 consisting of the following: a 100 nm W film used as an absorption layer, a 1 μm SiO₂ film, and a semi-infinite Si substrate. We will modify the thermal contact resistance between the SiO₂ and Si layers and the anisotropy ratio of the film’s thermal conductivity according to the cases in Table 2-8. The final

estimated values and the normalized uncertainties for each parameter are in Tables 9a – 9i. The cross correlation matrices for each case are in Tables 10a – 10i.

With the exception of Case 1, all cases converged to the \mathbf{s}_{true} . Case 1 was halted at 100 iterations due to extremely slow convergence. At this case, we find that the correlation between thermal contact resistance and thermal conductivity, $\rho_{k_z, R_{bdry}}$, is effectively unity (Table 2-10a, Figure 2-17). These two parameters have nearly the same effect on the probe beam deflections, and the estimation algorithm is unable to determine whether an increase in k_z (Figure 2-10) or an increase in R_{bdry} (Figure 2-11) is necessary to reduce the cost function (Figure 2-13). The columns of the Jacobian matrix associated with k_z and R_{bdry} will differ by a linear factor. In more severe cases of high correlation, the estimation algorithm will report an ill-conditioned or rank deficient matrix when attempting to perform the matrix inversion required by Eq 2.23. In such situations, it may be necessary to combine highly correlated parameters into a single parameter. For instance, one may estimate an “equivalent” thermal conductivity which accounts for the effects of both thermal contact resistance and cross-plane thermal conductivity. We hypothesize that this combination may be in the form of a series thermal resistance across the film layer and boundary. Figure 2-14 illustrates this by showing that the value of $\delta_{film} / k_z + R_{bdry}$ does not change from one iteration to the next (after the first ~10 iterations). Although the anisotropy ratio in the film is not as highly correlated to the other parameters, we see (Figure 2-12) that its convergence is likewise hindered by the other parameters.

From Figure 2-15, we see that the relative uncertainty in cross-plane thermal conductivity, σ_{k_z} / σ_w , is a strong function of anisotropy. High ratios of anisotropy produce lower uncertainty in thermal conductivity. We associate these high ratios of anisotropy with low values of cross-plane thermal conductivity (since k_r has been fixed), or films which are more insulating across their thickness. Such films have a

smaller thermal penetration depth, keeping more thermal energy in the film and gas phase rather than the substrate. Because of this, it is reasonable to expect that the probe beam deflections will be more sensitive to the thermal conductivity of the film. Thermal contact resistance seems to play much less of a role in our ability to accurately predict thermal conductivity.

Table 2-8: Conditions for varying anisotropy ratio and test case in truth-model validation

		$R_{bdry} \text{ (m}^2\text{-K/W)}$		
		10^{-7}	10^{-6}	10^{-5}
k_r/k_z $k_r = 1.38$	0.1	Case 1	Case 2	Case 3
	1	Case 4	Case 5	Case 6
	10	Case 7	Case 8	Case 9

From Figure 2-16, we see that the uncertainty in thermal contact resistance, $\sigma_{R_{bdry}}/\sigma_w$, is a strong function of thermal contact resistance. Higher values of contact resistance produce lower uncertainty in contact resistance. Such large values confine energy to the film and gas phase. Even for films with a large thermal penetration depth, the existence of a contact resistance may prevent energy flow from entering the substrate. This causes the probe beam deflections to be more sensitive to the composition of the film. Anisotropy seems to play less of a role in our ability to accurately predict thermal contact resistance. Increasing ratios of anisotropy provide only a slight decrease in this uncertainty.

From Figure 2-17, we see that the uncertainty in the anisotropy ratio of thermal conductivity, $\sigma_{k_r/k_z}/\sigma_w$, is a more complicated function of both anisotropy and thermal conductivity than the previous cases. The general trend is that the uncertainty

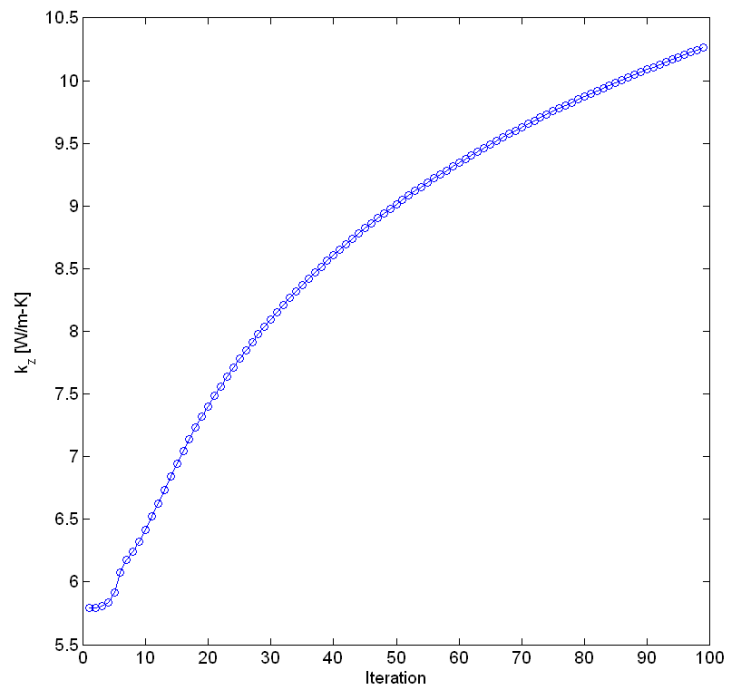


Figure 2-10: Estimation results (by iteration) for cross-plane thermal conductivity in Case 1

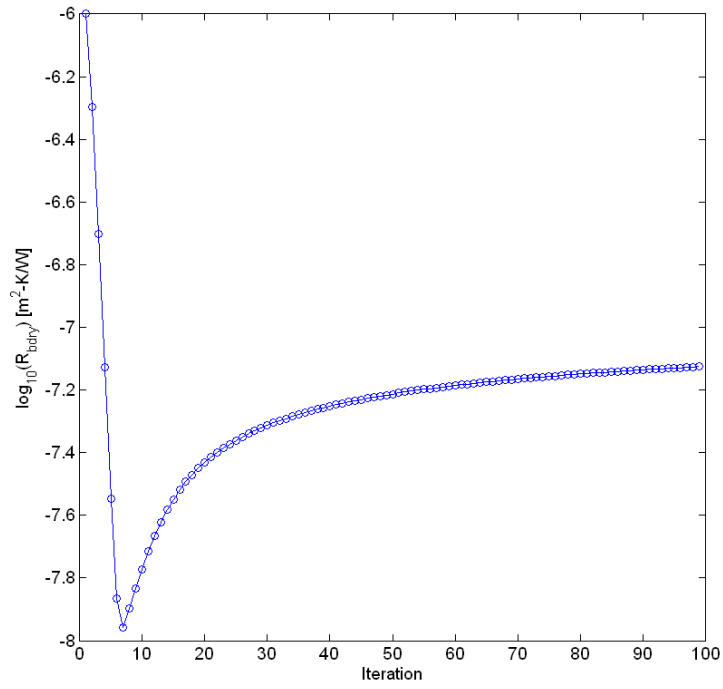


Figure 2-11: Estimation results (by iteration) for thermal contact resistance in Case 1

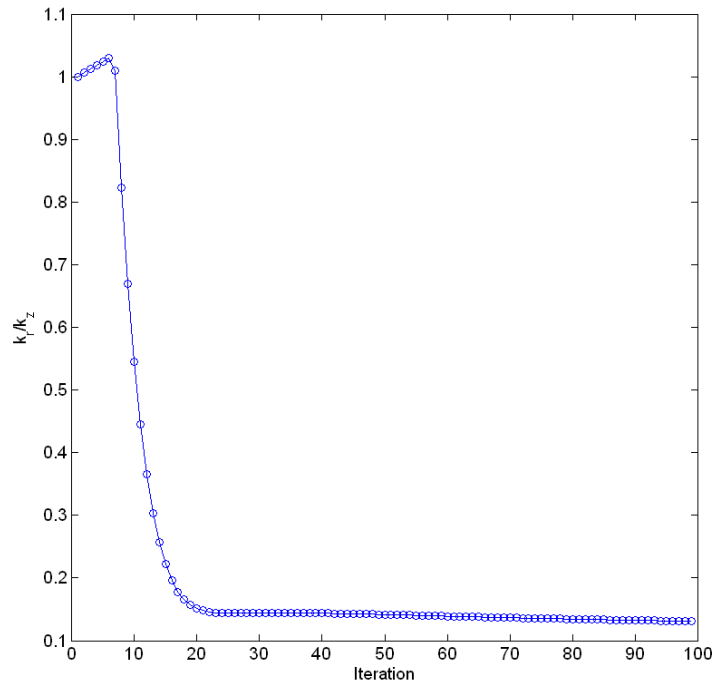


Figure 2-12: Estimation results (by iteration) for anisotropy ratio in Case 1

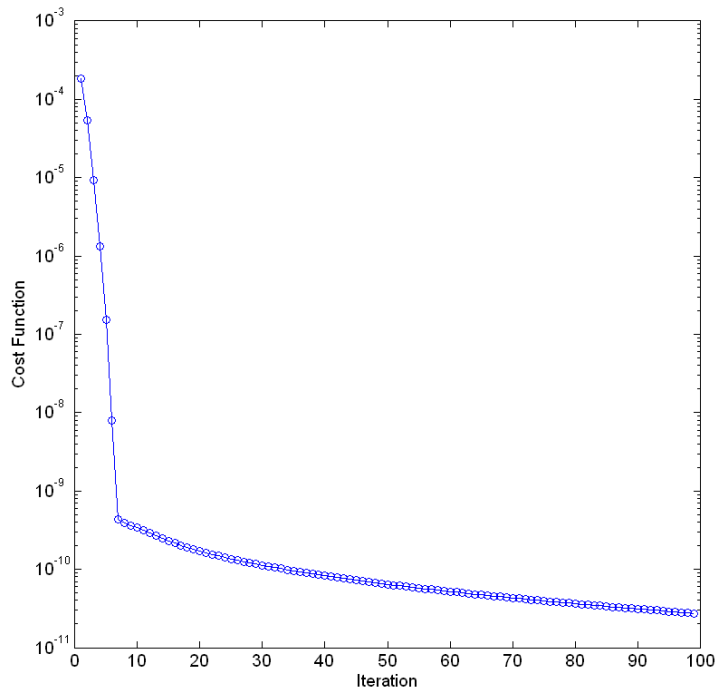


Figure 2-13: Cost function (by iteration) for Case 1

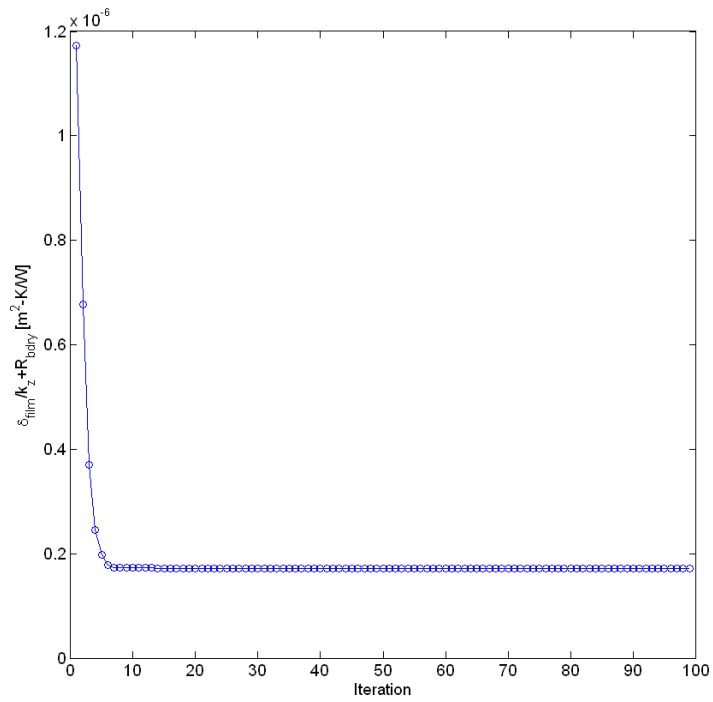


Figure 2-14: Equivalent resistance (by iteration) for Case 1

Table 2-9 (Case 1 – Case 9): Final parameter estimates and normalized parameter uncertainty for truth-model validation

Case 1 (Halted after 100 iterations)		
s	S_{final}	σ_s/σ_w
k_z [W/m-K]	10.3	3.98×10^5
$\log_{10}(R_{bdry})$ [m ² -K/W]	-7.13	2.39×10^4
k_r/k_z	0.13	2.70×10^4
Cost Function	2.74×10^{-11}	

Case 2		
s	S_{final}	σ_s/σ_w
k_z [W/m-K]	13.8	1.35×10^5
$\log_{10}(R_{bdry})$ [m ² -K/W]	-6.0	3.33×10^2
k_r/k_z	0.1	1.25×10^3
Cost Function	1.93×10^{-18}	

Case 3		
s	S_{final}	σ_s/σ_w
k_z [W/m-K]	13.8	1.22×10^5
$\log_{10}(R_{bdry})$ [m ² -K/W]	-5.0	3.11×10^1
k_r/k_z	0.1	8.89×10^2
Cost Function	6.71×10^{-19}	

Case 4		
s	S_{final}	σ_s/σ_w
k_z [W/m-K]	1.38	1.73×10^3
$\log_{10}(R_{bdry})$ [m ² -K/W]	-7.0	4.29×10^3
k_r/k_z	1.0	2.52×10^4
Cost Function	1.70×10^{-15}	

Case 5		
s	S_{final}	σ_s/σ_w
k_z [W/m-K]	1.38	9.37×10^2
$\log_{10}(R_{bdry})$ [m ² -K/W]	-6.0	2.34×10^2
k_r/k_z	1.0	5.51×10^3
Cost Function	1.32×10^{-16}	

Case 6		
s	S_{final}	σ_s/σ_w
k_z [W/m-K]	1.38	9.71×10^2
$\log_{10}(R_{bdry})$ [m ² -K/W]	-5.0	2.56×10^1
k_r/k_z	1.0	9.20×10^2
Cost Function	6.20×10^{-15}	

Table 2-9 (continued)

Case 7		
s	S_{final}	σ_s/σ_w
k_z [W/m-K]	0.138	1.11×10^1
$\log_{10}(R_{bdry})$ [m²-K/W]	-7.0	2.79×10^3
k_r/k_z	10	1.74×10^4
Cost Function	8.35×10^{-20}	
Case 8		
s	S_{final}	σ_s/σ_w
k_z [W/m-K]	0.138	1.01×10^1
$\log_{10}(R_{bdry})$ [m²-K/W]	-6.0	2.54×10^2
k_r/k_z	10	1.41×10^4
Cost Function	1.08×10^{-19}	
Case 9		
s	S_{final}	σ_s/σ_w
k_z [W/m-K]	0.138	8.84×10^0
$\log_{10}(R_{bdry})$ [m²-K/W]	-5.0	2.42×10^1
k_r/k_z	10	4.99×10^3
Cost Function	3.68×10^{-18}	

Table 2-10 (Case 1 – Case 9): Correlation matrix for truth-model validation

Case 1 s_2

ρ_{s_1, s_2}	k_z	$\log_{10}(R_{\text{bdry}})$	k_r/k_z
k_z	1.00	1.00	-0.05
$\log_{10}(R_{\text{bdry}})$		1.00	-0.03
k_r/k_z			1.00

Case 2 s_2

ρ_{s_1, s_2}	k_z	$\log_{10}(R_{\text{bdry}})$	k_r/k_z
k_z	1.00	0.99	-0.80
$\log_{10}(R_{\text{bdry}})$		1.00	-0.74
k_r/k_z			1.00

Case 3 s_2

ρ_{s_1, s_2}	k_z	$\log_{10}(R_{\text{bdry}})$	k_r/k_z
k_z	1.00	0.95	-1.00
$\log_{10}(R_{\text{bdry}})$		1.00	0.94
k_r/k_z			1.00

Case 4 s_2

ρ_{s_1, s_2}	k_z	$\log_{10}(R_{\text{bdry}})$	k_r/k_z
k_z	1.00	1.00	-0.14
$\log_{10}(R_{\text{bdry}})$		1.00	-0.07
k_r/k_z			1.00

Table 2-10 (continued)

Case 5

s_2

ρ_{s_1, s_2}	k_z	$\log_{10}(R_{bdry})$	k_r/k_z
k_z	1.00	0.98	-0.22
$\log_{10}(R_{bdry})$		1.00	-0.08
k_r/k_z			1.00

Case 6

s_2

ρ_{s_1, s_2}	k_z	$\log_{10}(R_{bdry})$	k_r/k_z
k_z	1.00	0.92	-0.84
$\log_{10}(R_{bdry})$		1.00	-0.63
k_r/k_z			1.00

Case 7

s_2

ρ_{s_1, s_2}	k_z	$\log_{10}(R_{bdry})$	k_r/k_z
k_z	1.00	0.96	-0.30
$\log_{10}(R_{bdry})$		1.00	-0.11
k_r/k_z			1.00

Case 8

s_2

ρ_{s_1, s_2}	k_z	$\log_{10}(R_{bdry})$	k_r/k_z
k_z	1.00	0.95	-0.30
$\log_{10}(R_{bdry})$		1.00	-0.08
k_r/k_z			1.00

Table 2-10 (continued)

Case 9

s_2

ρ_{s_1, s_2}		k_z	$\log_{10}(R_{\text{bdry}})$	k_r/k_z
s_1	k_z	1.00	0.84	-0.35
	$\log_{10}(R_{\text{bdry}})$		1.00	-0.04
	k_r/k_z			1.00

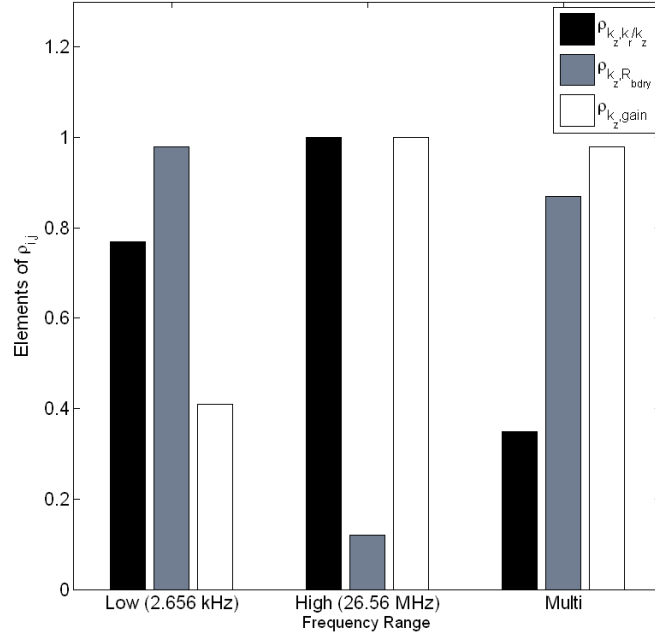


Figure 2-15: Normalized uncertainty in cross-plane thermal conductivity for film-on-substrate test cases

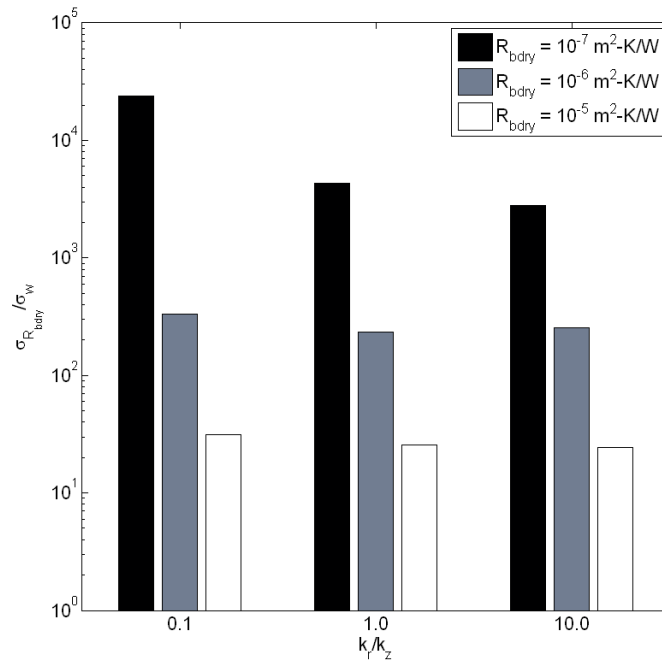


Figure 2-16: Normalized uncertainty in thermal contact resistance for film-on-substrate test cases

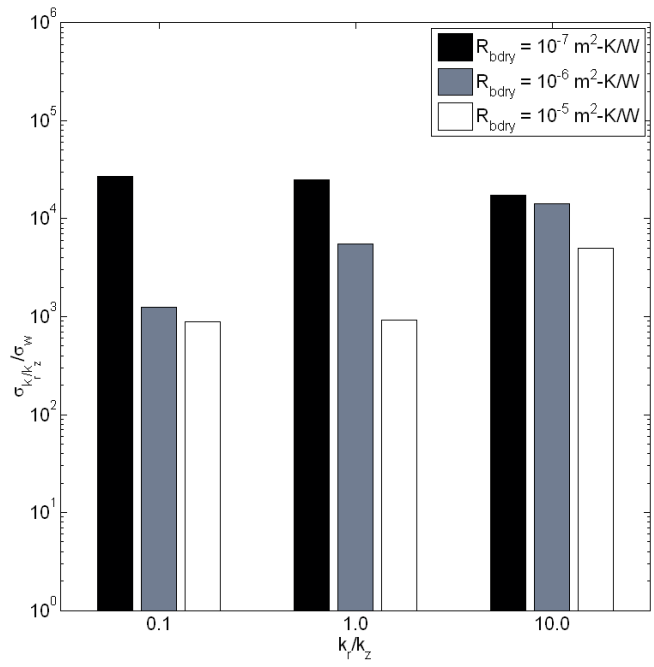


Figure 2-17: Normalized uncertainty in anisotropy ratio for film-on-substrate test cases

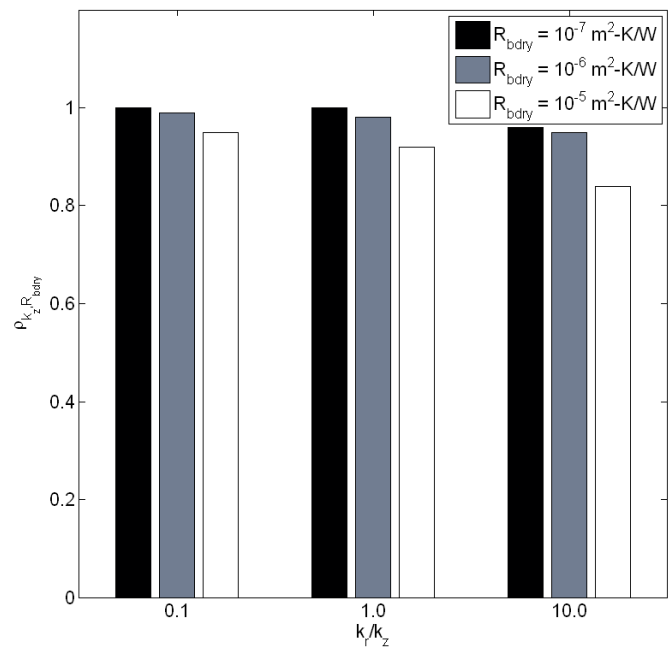


Figure 2-18: Cross correlation between cross-plane thermal conductivity and thermal contact resistance for film-on-substrate test cases

is reduced with increasing contact resistance, but increases with increasing anisotropy. In any case, there is no clear winner. It appears that anisotropy will often be the most uncertain of all of our parameters. Since the films we are analyzing are so thin, and the in-plane conductivity is so low, there is negligible heat spreading present to influence the probe beam deflections.

5. Conclusion

In this chapter, we have developed a maximum *a posteriori* parameter estimation algorithm which may be used to determine thermal properties of materials using PDS data. Special attention was paid to the posterior results, which include parameter covariances, uncertainty, and cross correlation values. A multi-frequency analysis scheme was developed which increases the overall accuracy of the parameter estimates and decreases the cross correlation between parameters such as thermal contact resistance and cross-plane thermal conductivity. A procedure was outlined for analyzing a “black box” film on substrate system in which the properties of the film are unknown.

Several test cases were run using simulated data sets for a representative film on substrate system. In most cases, the estimation algorithm was able to recover the properties of the film. For one case, however, the algorithm did not converge to the proper results. We diagnosed that the correlation between cross-plane thermal conductivity and thermal contact resistance was unity, indicating that these two parameters cannot be uniquely determined. In this case, the proper parameter grouping appears to be a series thermal resistance combining the thermal resistance of the film with the thermal contact resistance.

REFERENCES

- [1] G. E. Moore, "Cramming more components onto integrated circuits," *Electronics*, vol. 38, 1965.
- [2] R. M. Ramanathan and R. Willoner, "Silicon Innovation: Leaping from 90 nm to 65 nm," Intel, 2006.
- [3] A. Kazimirov, D. M. Smilgies, Q. Shen, X. Xiao, Q. Hao, E. Fontes, D. H. Bilderback, S. M. Gruner, Y. Platonov, and V. V. Martynov, "Multilayer X-ray optics at CHESS," *Journal of Synchrotron Radiation*, vol. 13, pp. 204-210, 2006.
- [4] C. W. Wilmsen, H. Temkin, and L. A. Coldren, *Vertical-cavity surface-emitting lasers : design, fabrication, characterization, and applications*. Cambridge ; New York: Cambridge University Press, 1999.
- [5] D. M. Rowe, *CRC handbook of thermoelectrics*. Boca Raton, FL: CRC Press, 1995.
- [6] N. W. Ashcroft and N. D. Mermin, *Solid state physics*. Philadelphia: Saunders College, 1976.
- [7] S. M. Lee and D. G. Cahill, "Heat transport in thin dielectric films," *Journal of Applied Physics*, vol. 81, pp. 2590-2595, 1997.
- [8] S. M. Lee, D. G. Cahill, and R. Venkatasubramanian, "Thermal conductivity of Si-Ge superlattices," *Applied Physics Letters*, vol. 70, pp. 2957-2959, 1997.
- [9] D. G. Cahill, K. Goodson, and A. Majumdar, "Thermometry and Thermal Transport in Micro/Nanoscale Solid-State Devices and Structures," *Journal of Heat Transfer*, vol. 124, pp. 223-241, 2002.
- [10] G. Chen, "Ballistic-diffusive heat-conduction equations," *Physical Review Letters*, vol. 86, pp. 2297-2300, 2001.

- [11] T. Zeng and G. Chen, "Phonon Heat Conduction in Thin Films: Impacts of Thermal Boundary Resistance and Internal Heat Generation," *Journal of Heat Transfer*, vol. 123, pp. 1-8, 2001.
- [12] J. C. Murphy and L. C. Aamodt, "Photothermal spectroscopy using optical beam probing: Mirage effect," *Journal of Applied Physics*, vol. 51, pp. 4580-4588, 1980.
- [13] A. C. Boccara, D. Fournier, W. Jackson, and N. M. Amer, "Sensitive photothermal deflection technique for measuring absorption in optically thin media," *Optics Letters*, vol. 5, pp. 377-379, 1980.
- [14] A. Rosencwaig, "Photo-acoustic spectroscopy of solids," *Review of Scientific Instruments*, vol. 48, pp. 1133-1137, 1977.
- [15] D. G. Cahill, "THERMAL-CONDUCTIVITY MEASUREMENT FROM 30-K TO 750-K - THE 3-OMEGA METHOD," *Review of Scientific Instruments*, vol. 61, pp. 802-808, Feb 1990.
- [16] C. A. Paddock and G. L. Eesley, "TRANSIENT THERMOREFLECTANCE FROM THIN METAL-FILMS," *Journal of Applied Physics*, vol. 60, pp. 285-290, Jul 1986.
- [17] A. Majumdar, "Scanning thermal microscopy," *Annual Review of Materials Science*, vol. 29, pp. 505-585, 1999.
- [18] J. Rantala, L. Wei, P. K. Kuo, J. Jaarinen, M. Luukkala, and R. L. Thomas, "Determination of thermal diffusivity of low-diffusivity materials using the mirage method with multiparameter fitting," *Journal of Applied Physics*, vol. 73, pp. 2714-2723, 1993.
- [19] C. B. Reyes, "Thermal Wave Measurement of Thermal Diffusivity of Solids," in *Physics (Solid State)*. vol. Ph.D. Detroit, MI: Wayne State University, 1988.
- [20] H. Machlab, W. A. McGahan, and J. A. Woollam, "THERMAL-DIFFUSIVITY MEASUREMENTS BY PHOTOTHERMAL LASER-BEAM DEFLECTION (PTD) - DATA-ANALYSIS USING THE LEVENBERG-MARQUARDT ALGORITHM," *Thin Solid Films*, vol. 215, pp. 103-107, Jul 1992.

- [21] P. E. Gill, W. Murray, and M. H. Wright, *Practical optimization*. London ; New York: Academic Press, 1981.
- [22] Y. Bar-Shalom, X.-R. Li, and T. Kirubarajan, *Estimation with applications to tracking and navigation*. New York: Wiley, 2001.
- [23] D. W. Marquardt, "AN ALGORITHM FOR LEAST-SQUARES ESTIMATION OF NONLINEAR PARAMETERS," *Journal of the Society for Industrial and Applied Mathematics*, vol. 11, pp. 431-441, 1963.
- [24] J. R. Foley, "Model-based estimation of the anisotropic thermal properties of materials from photothermal deflection spectroscopy data using Bayesian inference," Cornell University, Aug., 2007., 2007, pp. xvii, 353 leaves.
- [25] F. M. Ham and R. G. Brown, "Observability, Eigenvalues, and Kalman Filtering," *IEEE Transactions on Aerospace and Electronic Systems*, vol. AES-19, pp. 269-273, 1983.
- [26] A. Neumaier, "Solving ill-conditioned and singular linear systems: A tutorial on regularization," *Siam Review*, vol. 40, pp. 636-666, 1998.
- [27] J. G. Graeme, *Photodiode amplifiers : op amp solutions*. Boston, Mass.: McGraw Hill, 1996.
- [28] A. Salazar, A. Sanchez-Lavega, and J. Fernandez, "Thermal diffusivity measurements in solids by the ``mirage" technique: Experimental results," *Journal of Applied Physics*, vol. 69, pp. 1216-1223, 1991.
- [29] P. K. Kuo, L. J. Inglehart, E. D. Sandler, M. J. Lin, L. D. Favro, and R. L. Thomas, *Review of Progress in Quantitative NDE* vol. 4B. New York: Plenum, 1985.
- [30] F. P. Incropera, *Introduction to heat transfer*, 5th ed. Hoboken, N.J.: J. Wiley, 2007.

CHAPTER THREE

Determining the thermal conductivity of W/B₄C multilayer structures

1. Introduction

Our current objective is to determine the thermal properties of a series of multilayer (ML) materials consisting of alternating films of tungsten (W) and boron carbide (B_4C). These materials serve as X-ray monochromator mirrors in Cornell's High Energy Synchrotron Source (CHESS) [1]. One of the challenges faced with ML monochromators is that they experience a thermo-elastic deformation (i.e. a "thermal bump") due to the tremendous heat load of the incident synchrotron radiation [2]. This bump produces an undesirable broadening of the X-ray rocking curve. It is possible to compensate for this effect through a deconvolution process, but the thermal properties of the ML must be known in order to correctly model the temperature distribution and resulting deformation. Unfortunately, the value of the thermal conductivity of thin films and ML structures is known to experience a significant reduction when contrasted to its bulk counterpart, thus the bulk values may not be used. This difference may be the result of: 1.) confinement effects when the thickness of the film is much less than the mean free path (mfp) of the energy carriers (i.e. electrons and phonons), 2.) thermal contact resistance between adjacent layers, and 3.) defects in the film or ML crystal structure.

There are several excellent review articles which discuss heat transfer at the micro and nano-scales [3-6]. It is clear that, despite much effort and progress, the mechanisms of heat transfer in ML structures continue to be poorly understood. It is known, however, that crystal lattice vibrations called "phonons" play a significant part in the thermal conductivity of such materials. From kinetic theory, thermal conductivity is

$$k = \frac{1}{3} c v_g l \tag{3.1}$$

where c is the volumetric specific heat, v_g is the phonon group velocity, and l is the phonon mfp. When the thickness of a film, δ , is significantly less than l , the thermal

conductivity is expected to be reduced. Cahill et al. [5] have previously reported that the mfp for phonons in bulk insulators and semiconductors ranges from 10-100 nm, with a corresponding group velocity ranging from $3-10 \times 10^3$ m/s. The individual layers in our W/B₄C ML structures have thicknesses ranging from 0.41-4.6 nm, well below the expected phonon mfp.

Traditional methods for the determination of thermal conductivity, such as the cut-bar method [7], are not suitable for use with thin films or ML structures. The thickness of the sample is so small that an unreasonably large heat flux is necessary to produce a measurable temperature drop across the sample. Over the past several years, researchers have begun using a class of “thermal wave” techniques which share the characteristic that they are able to confine a thermal wave to specified length-scales by controlling the modulation frequency of an applied heat source. Using these techniques, it is possible to thermally probe thin films and ML structures at length-scales comparable to their thickness.

The most commonly used thermal wave technique is the $3-\omega$ method [8], an AC calorimetry technique which utilizes a combined heater/resistance thermometer on the sample surface to provide a modulated heat source and measure the resulting temperature response. This method has successfully been used to determine the thermal conductivity of materials such as oxide films [9-11], Si/Ge [12-14], Bi/Sb [15], InGaAs/InGaAsP [13], and GaAs/AlGaAs [16] superlattices. The modulated/transient thermoreflectance (TR) technique uses surface reflectivity as a thermometric property to determine the surface temperature from modulated or pulsed laser heating of a sample. It has been successful in determining the thermal conductivity of materials such as SiO₂ films [17], metallic films [18-20], and GaAs/AlAs superlattices [21]. The scanning thermal microscope (SThM) uses an AFM-like stylus as a thermocouple to determine the surface temperature from

modulated laser heating of a sample. It has been successful in determining the thermal conductivity of Au [22] and SiO₂ [23] films. The photoacoustic (PA) method, which measures pressure changes caused by variations in temperature, has also been used to determine the thermal conductivity of several thin films [24]. The method which we will use (discussed in previous chapters) is photothermal deflection spectroscopy (PDS). PDS has previously been used to determine the thermal conductivity of diamond films [25], GaAs epitaxial layers [26], and Al/Ti multilayers [27]. To our knowledge, none of these techniques have been used to determine the thermal properties of W/B₄C multilayers. A more comprehensive literature review on thermal wave techniques and PDS is given in [28].

2. Multilayer Samples

The W/B₄C ML samples used for this study were fabricated by Rigaku, Inc. (9009 New Trails Dr, The Woodlands, TX, USA, 77381-5209). Each of the multilayers was deposited on a 4", 9 mil (228.6 μm) Si wafer using a magnetron sputtering process. In order to neglect the complicated condition in which there are multiple reflections with partial optical absorption of the heating beam in each layer (see Chapter 1), we deposited a nominally 110 nm thick W layer atop the ML structure using a magnetron sputtering process to act as an optical absorption layer. Prior to deposition, a "gentle" ion beam cleaning step was taken to remove organic contamination from the ML surface. The top-most layer of the ML is B₄C, an extremely hard substance, so there is little concern of damage to the underlying ML. This process was performed at the Cornell NanoScale Science & Technology Center (CNF).

The ML samples were selected such that they each have the same overall thickness (nominally 0.45 μm), with a different number of bi-layer periods. The term "bi-layer" is defined as a single period consisting of a W film and a B₄C film. This

choice was made in order to remove any effect of overall thickness in the determination of thermal conductivity. Any change that occurs should be due to the number of layer interfaces present or the thickness of the individual film layers. We note that we would have preferred a larger overall thickness (i.e. $\delta_{ML} \geq 1 \mu m$) in order to have more sensitivity to the film, but this was not possible for the following reasons: 1.) the fabrication of ML samples is costly and time consuming, and 2.) the strain build-up due to lattice mismatch of the W and B₄C layers prevents the fabrication of an arbitrarily large number of layers (common to many ML combinations). The design specifications are listed in Table 3-1.

Table 3-1: W/B₄C multilayer specifications

Property	Sample 2	Sample 3	Sample 4	Sample 5
2-d Design [Å]	15	30	45	60
$N_{periods}$	300	150	100	75
$\delta_{W,meas}$ [Å]	4.3	8	11.2	14.5
$\delta_{B_4C,meas}$ [Å]	10.5	21.7	33.7	46
2-d Calculated [Å]	14.8	29.7	44.9	60.5
δ_{total} [Å]	4440	4455	4490	4537.5

Our method of estimating the thermal conductivity of the ML using PDS measurements does not have the sensitivity required to estimate the properties of each individual layer. In fact, layers at these scales may not even have distinct interfaces due to processes such as molecular diffusion. Instead, what we propose is to estimate the effective thermal conductivity of the entire ML structure as a single film on a Si substrate. In order to do this, it is necessary to have proper estimates for the heat capacity, ρC , since the thermal conductivity appears in a grouping of parameters representing the thermal diffusivity, $k_z/\rho C$, of the film. We will define an effective film density as

$$\rho_{effective} \delta_{ML} = \sum_i \rho_i \delta_i \quad 3.2.$$

We will similarly define an effective specific heat as

$$C_{effective} \delta_{ML} = \sum_i C_i \delta_i \quad 3.3.$$

Although our intent is to determine the thermal conductivity of the ML, it is illustrative to compare the value to an effective thermal conductivity that would result from stacking individual layers of W and B₄C assuming bulk properties and negligible thermal contact resistance at layer interfaces. This effective thermal conductivity comes from

$$\frac{\delta_{ML}}{k_{effective}} = \sum_i \frac{\delta_i}{k_i} \quad 3.4.$$

The bulk properties of W and B₄C evaluated at 300 K [29, 30] are provided in Table 3-2. The effective bulk properties of the ML from Eqs 3.2 - 3.4 are provided in Table 3-3. A schematic of how we treat the ML as an equivalent film is provided in Figure 3-1.

Table 3-2: Bulk properties @ 300 K [29, 30]

Property	W	B ₄ C	Si	Air
$\rho [kg/m^3]$	19300	2520	2330	1.1614
$C [J/kg - K]$	132	921	712	1007
$k [W/m - K]$	174	30	148	0.0263

Table 3-3: Equivalent bulk properties of multilayer samples (Eqs 3.2 – 3.4)

Property	Sample 2	Sample 3	Sample 4	Sample 5
$\rho_{equiv} [kg/m^3]$	7395.3	7039.9	6705.7	6541.7
$C_{equiv} [J/kg - K]$	691.8	708.5	724.2	731.9
$k_{z,equiv} [W/m - K]$	39.5	38.6	37.8	37.4

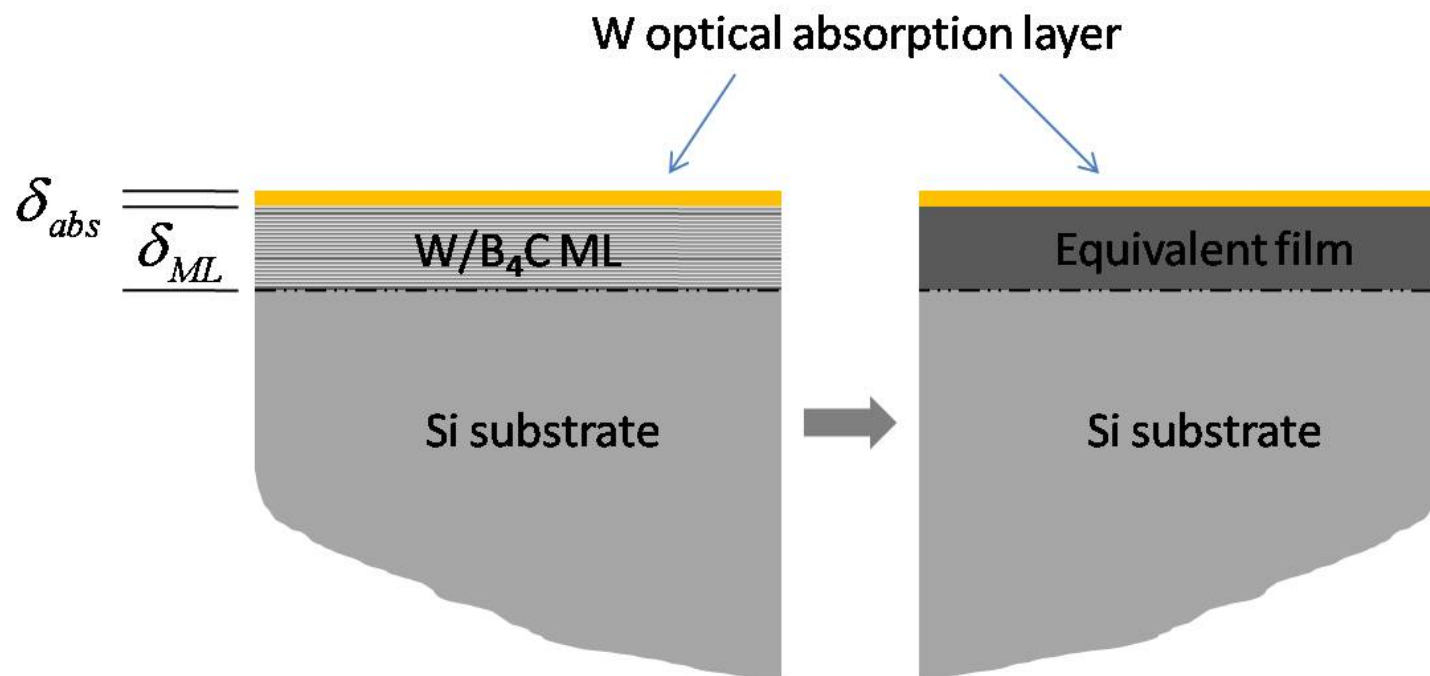


Figure 3-1: Equivalent film representation of a multilayer structure

3. Experimental Results

Our experimental apparatus for bounced-beam, transverse PDS has been described in detail in Chapter 1. Probe beam deflection signals were recorded for each of the four (4) ML samples at modulation frequencies of 1, 2, 4, 8, 16, 32, 64, and 128 kHz with a nominal heating beam power of 50 mW at the first harmonic of these frequencies. The heating beam radius ($1/e^2$) is estimated to be 4.5 μm , and the probe beam radius ($1/e^2$) at its waist was measured to be 23.9 μm . The experiment was operated about an aligned position such that the height of the probe beam above the sample is zero, resulting in negligible probe beam deflections in the direction normal to the surface. Only the tangential components of the probe beam deflection will be used in the current analysis. Pre-processing of the experimental data was performed as outlined in Chapter 2. The estimation of parameters was performed in several steps using the algorithm developed in Chapter 2. Table 3-4 provides a key of model parameters that are fixed/varied in the following cases.

For the first case, the estimation algorithm was implemented using the thermal conductivity of the ML as the only floating parameter (i.e. $\mathbf{s} = [k_{z,ML}]$). The ML was assumed to have an isotropic thermal conductivity (i.e. $k_{r,ML} = k_{z,ML}$), and the thermal contact resistance between the ML and the substrate was assumed to be zero (i.e. $R_{bdry,ML/sub} = 0$). This step was done in order to make the modeled probe beam deflections “sufficiently close” to the measured probe beam deflections such that the residuals become small, a pre-condition to our neglecting the Hessian matrix of the model (refer to Eq 2.9). The “initial guess” values of thermal conductivity ranged from $0.1 \leq k_{z,ML} \leq 1000 \text{ W/m-K}$ by factors of 10 with a diffuse prior uncertainty (i.e. $\sigma_{k_{z,ML}} \rightarrow \infty$). The results of this first step are provided in Tables 3-5 through 3-8, Case 1.

Table 3-4: Summary of fixed and variable parameters

Case	Parameter				
	k_z	R_p	G_{mult}	R_{bdry}	k_r/k_z
1	variable	23.9 μm	1	0	1
2	variable	variable	1	0	1
3	variable	variable	variable	0	1
4	variable	variable	variable	variable	1
5	variable	variable	variable	0	variable

Table 3-5: Results of estimation for W/B₄C (Sample 2)

Parameter	Case 1	Case 2	Case 3	Case 4	Case 5
$k_{z,ML} \left[\frac{W}{m-K} \right]$	1.36 (0.1,1,10,10 0,1000)	1.18 (1.36)	1.35 (1.36)	3.01 (1.36)	1.35 (1.36)
$R_p [\mu m]$		25.6 (23.9)	25.5 (23.9)	25.5 (23.9)	25.5 (23.9)
$G_{mult} [N.D.]$			1.09 (1)	1.08 (1)	1.09 (1)
$R_{bdry,ML/sub} \left[\frac{m^2 - K}{W} \right]$				$10^{-6.73}$ (10^{-6})	
$k_{r,ML} / k_{z,ML} [N.D.]$					0.001 (1)
$CF [N.D.]$	3.77×10^6	2.95×10^6	2.93×10^6	2.91×10^6	2.93×10^6

Table 3-6: Results of estimation for W/B₄C (Sample 3)

Parameter	Case 1	Case 2	Case 3	Case 4	Case 5
$k_{z,ML} \left[\frac{W}{m-K} \right]$	0.79 (0.1,1,10,10 0,1000)	0.71 (0.79)	0.72 (0.79)	1.05 (0.79)	0.72 (0.79)
$R_p [\mu m]$		25.5 (23.9)	25.5 (23.9)	25.5 (23.9)	25.5 (23.9)
$G_{mult} [N.D.]$			1.01 (1)	1.03 (1)	1.01 (1)
$R_{bdry,ML/sub} \left[\frac{m^2 - K}{W} \right]$				$10^{-6.74}$ (10^{-6})	
$k_{r,ML} / k_{z,ML} [N.D.]$					0.001 (1)
$CF [N.D.]$	1.29×10^6	3.75×10^5	3.75×10^5	3.75×10^5	3.75×10^5

Table 3-7: Results of estimation for W/B₄C (Sample 4)

Parameter	Case 1	Case 2	Case 3	Case 4	Case 5
$k_{z,ML} \left[\frac{W}{m-K} \right]$	1.00 (0.1,1,10,10 0,1000)	0.90 (1.00)	0.79 (1.00)	0.82 (1.00)	0.79 (1.00)
$R_p [\mu m]$		25.3 (23.9)	25.3 (23.9)	25.3 (23.9)	25.3 (23.9)
$G_{mult} [N.D.]$			0.90 (1)	0.91 (1)	0.90 (1)
$R_{bdry,ML/sub} \left[\frac{m^2 - K}{W} \right]$				$10^{-7.67}$ (10^{-6})	
$k_{r,ML} / k_{z,ML} [N.D.]$					0.001 (1)
$CF [N.D.]$	7.88×10^5	2.60×10^5	2.42×10^5	2.46×10^5	2.42×10^5

Table 3-8: Results of estimation for W/B₄C (Sample 5)

Parameter	Case 1	Case 2	Case 3	Case 4	Case 5
$k_{z,ML} \left[\frac{W}{m-K} \right]$	0.65 (0.1,1,10,10 0,1000)	0.59 (0.65)	0.51 (0.65)	0.54 (0.65)	0.51 (0.65)
$R_p [\mu m]$		25.1 (23.9)	25.0 (23.9)	25.0 (23.9)	25.0 (23.9)
$G_{mult} [N.D.]$			0.88 (1)	0.89 (1)	0.88 (1)
$R_{bdry,ML/sub} \left[\frac{m^2 - K}{W} \right]$				$10^{-7.38}$ (10^{-6})	
$k_{r,ML} / k_{z,ML} [N.D.]$					0.001 (1)
$CF [N.D.]$	1.59×10^6	5.81×10^5	5.48×10^5	5.46×10^5	2.42×10^5

For each sample, the estimator converged to a unique value of thermal conductivity, regardless of initial guess. We do not hold up these values as being the true values of thermal conductivity for the ML, as other model parameters may not be known with certainty.

For the case 2, the estimation algorithm was run using a parameter vector which included thermal conductivity and probe beam radius (i.e. $\mathbf{s} = [k_{z,ML}, R_p]$). The decision to add probe beam radius is based on our inability to measure its value *in situ*. Although we know the radius at the focused beam waist, the experiment may be aligned such that the waist does not precisely coincide with the center of the thermal field. The differences should be small, but the probe beam deflections are very sensitive to the value of the probe beam radius. The initial guess used for the probe beam radius was 23.9 μm with an *a priori* standard deviation of 10% (i.e. $\sigma_{R_p,0} = 2.39 \mu\text{m}$). The ML was assumed to have an isotropic thermal conductivity (i.e. $k_{r,ML} = k_{z,ML}$), and the thermal contact resistance was assumed to be zero (i.e. $R_{bdry,ML/sub} = 0$). The results of this step are provided in Tables 3-5 through 3-8, Case 2.

For case 3, the estimation algorithm was run using a parameter vector which included thermal conductivity, probe beam radius, and gain multiplier (i.e. $\mathbf{s} = [k_{z,ML}, R_p, G_{mult}]$). The decision to add gain multiplier is based on the fact that we may have imperfect knowledge of model parameters which act as linear multipliers to the probe beam deflection signal (e.g. surface reflectivity, heating beam power, electronic amplification, geometric factors). The initial guess used for the gain multiplier was 1 (non-dimensional), with a diffuse prior uncertainty (i.e. $\sigma_{G_{mult},0} \rightarrow \infty$). In the event of poor convergence, it is not unreasonable to assume a finite prior uncertainty, but we did not wish to overly constrain the estimator. Once again, the ML was assumed to have an isotropic thermal conductivity (i.e. $k_{r,ML} = k_{z,ML}$), and the

thermal contact resistance was assumed to be zero (i.e. $R_{bdry,ML/sub} = 0$). We note that this combination of parameters was successfully used in Chapter 1 to determine the thermal conductivity of bulk standard reference materials. The results of this step are provided in Tables 3-5 through 3-8, Case 3. Furthermore, we have produced plots comparing the measured probe beam deflections to the modeled probe beam deflections for Samples 2-5 in Figures 3-2 through 3-5, respectively. Figures were not produced for the other cases, as they will be visually similar.

For case 4, the estimation algorithm was run using a parameter vector which included thermal conductivity, probe beam radius, gain multiplier, and thermal contact resistance (i.e. $\mathbf{s} = [k_{z,ML}, R_p, G_{mult}, R_{bdry,ML/sub}]$). Our decision to model a concentrated thermal contact resistance between the ML and the substrate may serve to act as an “equivalent” resistance which accounts for the cumulative effect of each of the individual resistances. The initial guess used for thermal contact resistance was 10^{-6} m²-K/W (an arbitrary, but reasonable value) with a diffuse prior uncertainty (i.e. $\sigma_{R_{bdry,ML/sub},0} \rightarrow \infty$). Once again, the ML was assumed to have an isotropic thermal conductivity (i.e. $k_{r,ML} = k_{z,ML}$). The results of this step are provided in Tables 3-5 through 3-8, Case 4.

For the fifth step, the estimation algorithm was run using a parameter vector which included thermal conductivity, probe beam radius, gain multiplier, and anisotropy ratio of the thermal conductivity in the ML (i.e. $\mathbf{s} = [k_{z,ML}, R_p, G_{mult}, k_{r,ML}/k_{z,ML}]$). Each of the layers in the ML may have a different degree of anisotropy. For instance, the metallic W layers may act as effective heat spreaders in the in-plane direction, while experiencing a reduced thermal conductivity in the cross-plane direction. We are not modeling this effect in the individual layers, but rather an “equivalent” anisotropy which accounts for the cumulative effect

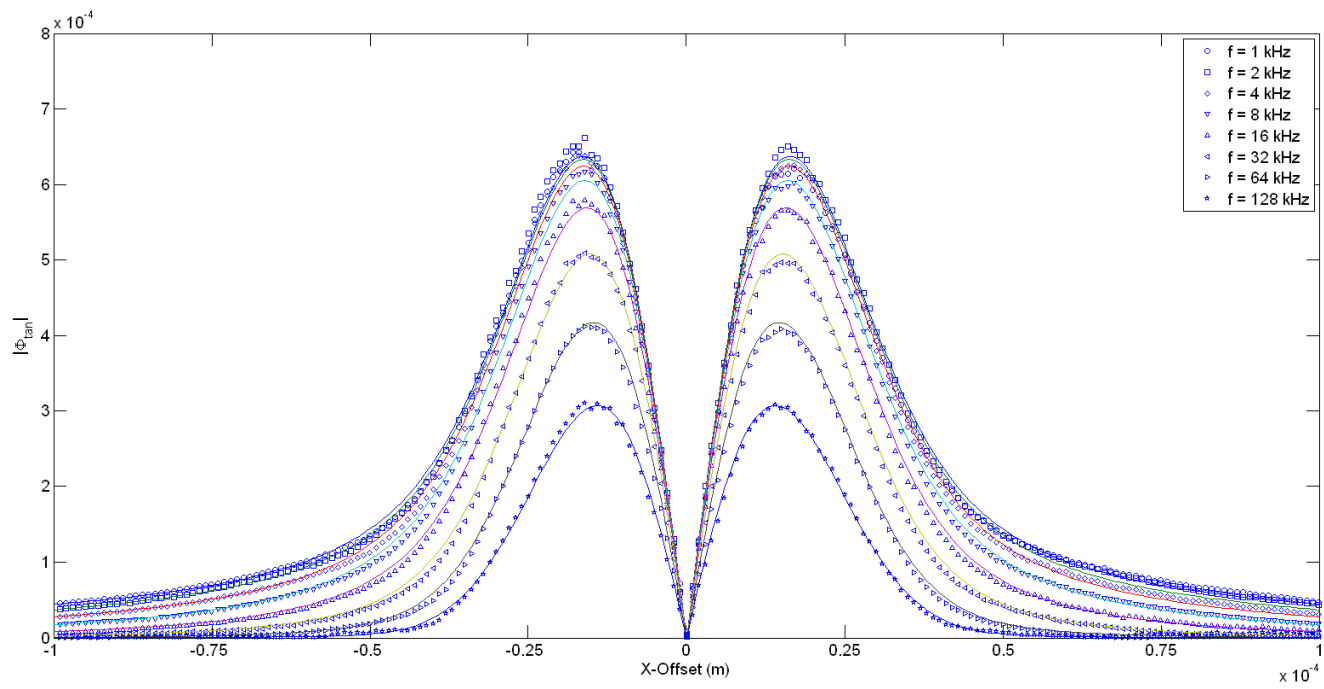


Figure 3-2: Measured and predicted probe beam deflections for Sample 2 (Case 3)

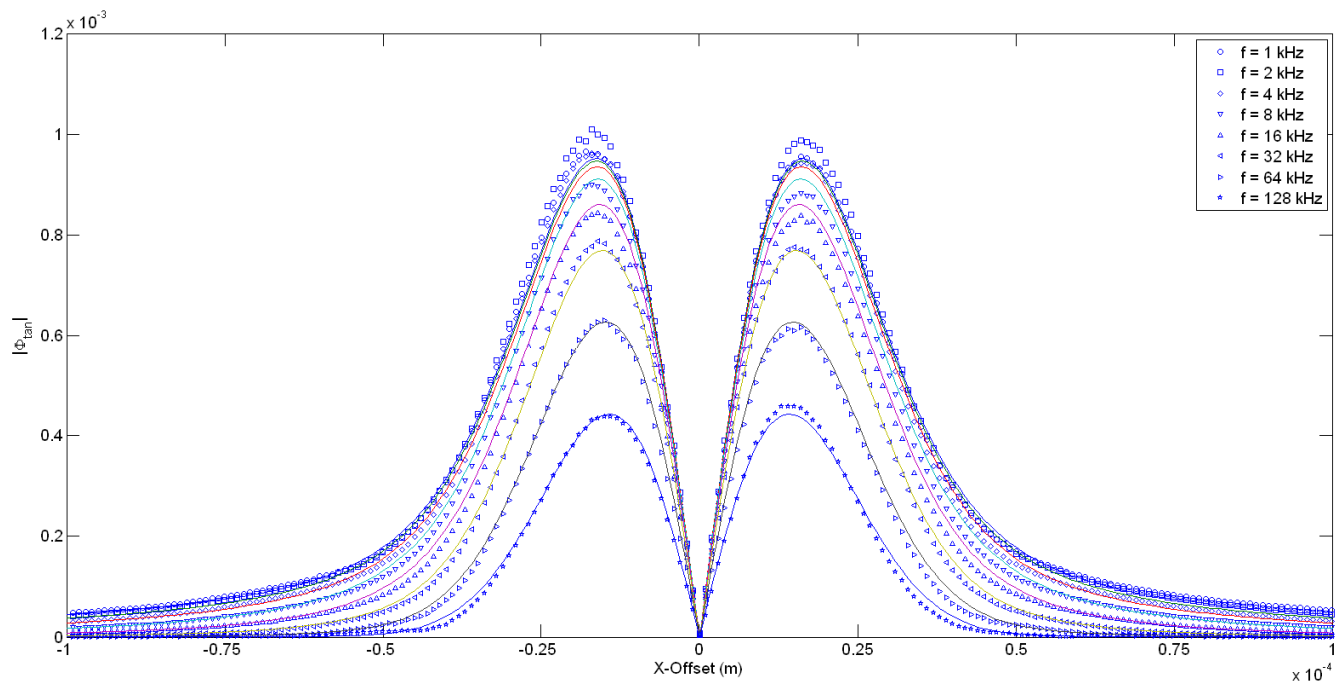


Figure 3-3: Measured and predicted probe beam deflections for Sample 3 (Case 3)

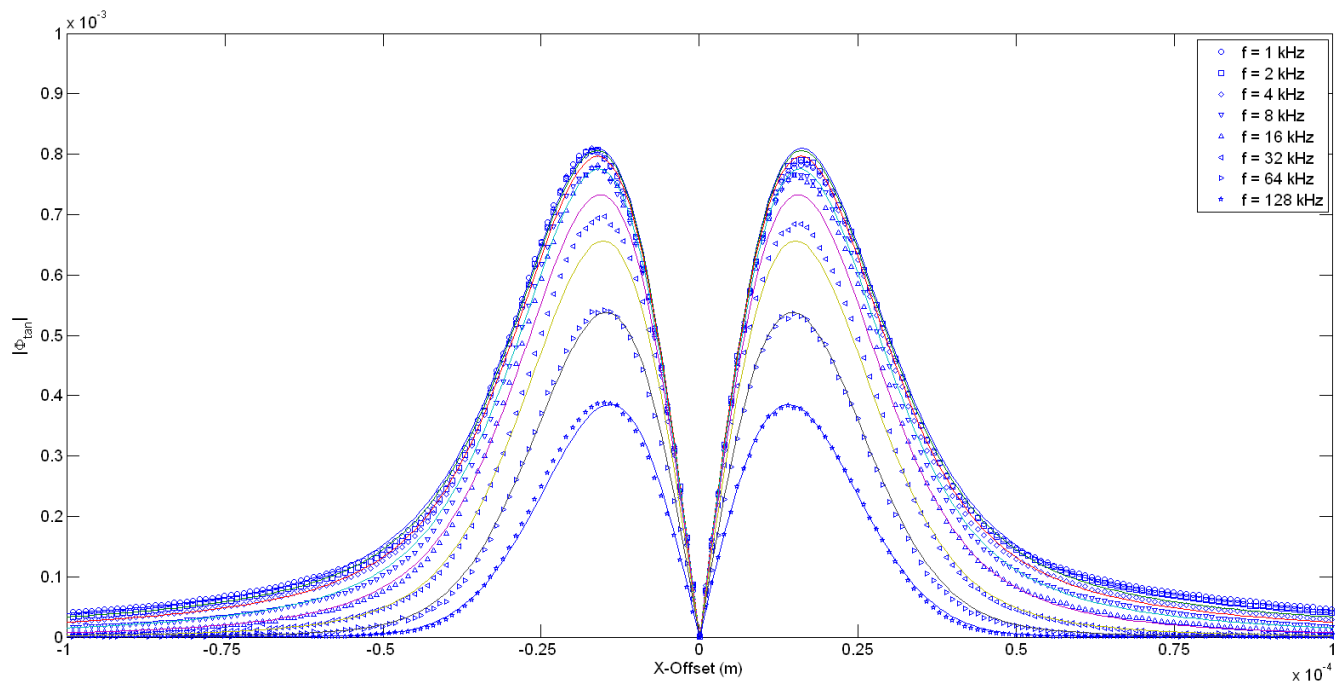


Figure 3-4: Measured and predicted probe beam deflections for Sample 4 (Case 3)

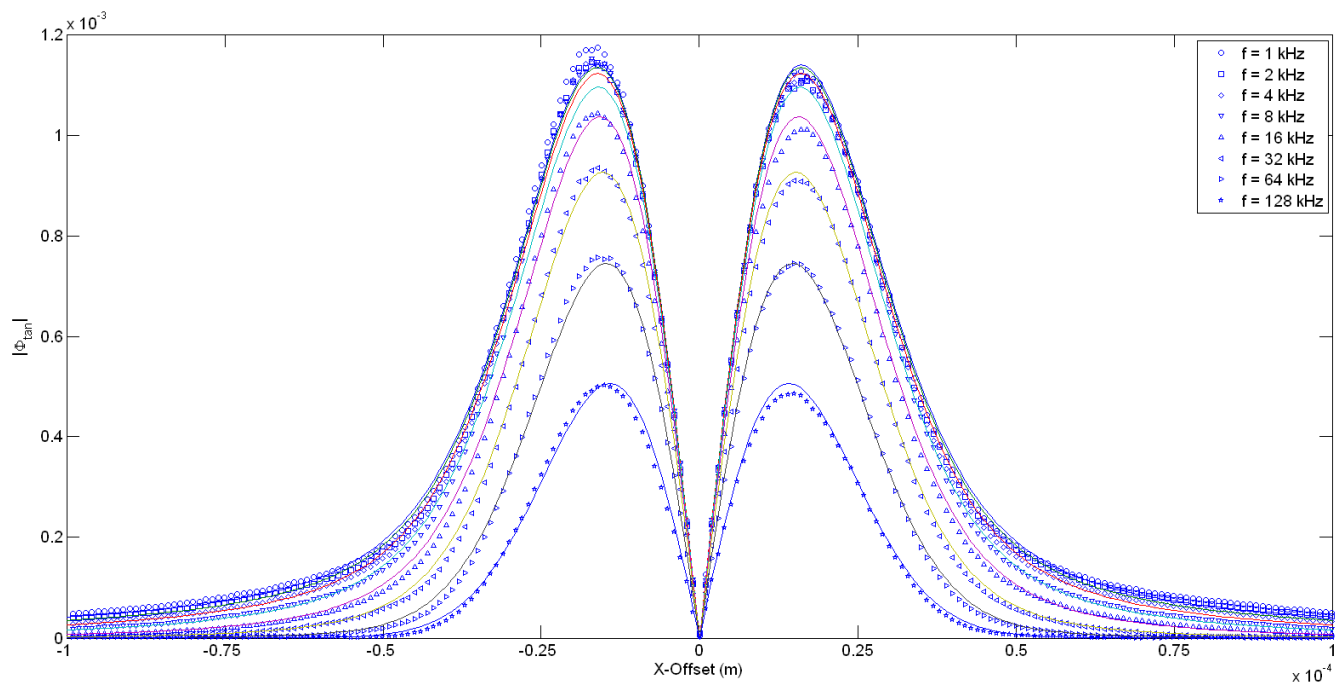


Figure 3-5: Measured and predicted probe beam deflections for Sample 5 (Case 4)

throughout the ML. The initial guess used for anisotropy ratio was 1 (non-dimensional) with a diffuse prior uncertainty (i.e. $\sigma_{k_r,ML}/k_{z,ML,0} \rightarrow \infty$). The thermal contact resistance was again assumed to be zero (i.e. $R_{bdry,ML/sub} = 0$). The results of this step are provided in Tables 3-5 through 3-8, Case 5.

Our original expectation was that we would see a decrease in cross-plane thermal conductivity as the number of periods increases (i.e. as the individual layers become thinner). The results, as summarized in Figure 3-6, indicate this is not the case with our ML samples. Although we obtain values of thermal conductivity which are significantly less than the bulk equivalent calculated by Eq 3.4, the value seems to decrease slightly as the number of periods decreases. This trend has been observed previously in the literature [12, 14, 21], and has been attributed to the formation of dislocations due to strain build-up from lattice mismatch between the constituent layers in the ML. The ensemble average of our four ML samples over five estimation trials produces a thermal conductivity of $k_{z,ML} = 0.97 W/m-K$, which is significantly less than the bulk values of $37.4 \leq k_{z,ML} \leq 39.5 W/m-K$ predicted by Eq 3.4. We believe that this provides strong evidence that there is non-macroscopic thermal behavior in the samples.

One of the features that stands out in Figure 3-6 is the significantly higher thermal conductivity predicted for Sample 2, Case 4, in which the thermal contact resistance was allowed to float. Taking a closer look at this case, we find that the cross-correlation value between cross-plane thermal conductivity and thermal contact resistance is $\rho_{k_z, R_{bdry}} = 0.985$. This indicates that these two parameters have nearly the same effect on our measurements, and it is very difficult for the estimation algorithm to distinguish between the effects of k_z and R_{bdry} . This high degree of correlation is, in fact, the case for many of our Case 4 estimates. We believe that the proper relationship may be in the form of an “equivalent” series resistance given by

$$R_{eq} = \delta_{ML}/k_z + R_{bdry} \quad 3.5$$

Calculations of R_{eq} are provided in Figure 3-7 for each of the estimation trials. Note that the equivalent resistance for Sample 2, Case 4 is comparable to those of the other cases. It also follows that the equivalent resistance across the ML should increase as the number of periods decreases.

We have previously stated that our model has cross-plane thermal conductivity appearing with the heat capacity of the material in the form of thermal diffusivity. Thermal waves are, after all, diffusion processes. In Figure 3-8, we calculate the effective thermal diffusivity based on our estimation results for thermal conductivity and the equivalent values of ρ and C provided in Table 3-3.

For case 5 of each of the ML samples, in which we allow the anisotropy ratio to float, this parameter uniformly hits the user-specified lower bound in our estimation algorithm (i.e. $k_{r,ML}/k_{z,ML} = 0.001$). This indicates that the in-plane thermal conductivity is achieving values which are 1000 times greater than the cross-plane thermal conductivity, which we are estimating as a separate parameter. There is no physical argument that can be made which would explain this behavior. The expectation is that the in-plane thermal conductivity should be close to the bulk thermal conductivity since there are no boundaries (i.e. layer interfaces) and the phonon mfp should be unaffected in that direction. What is actually happening here is that the algorithm has no sensitivity to the anisotropy at this set of model parameters. Virtually any value of in-plane thermal conductivity will produce the same estimate of cross-plane thermal conductivity. Therefore, we are unable to make a claim regarding whether the ML has isotropic or anisotropic thermal conductivity.

We note that in the development of the mathematical model (refer to Eq 1.3 through 1.11), that k_z and k_r appear in several places. At times, they appear in the form of a ratio, which we have referred to as the anisotropy. At other times, k_z

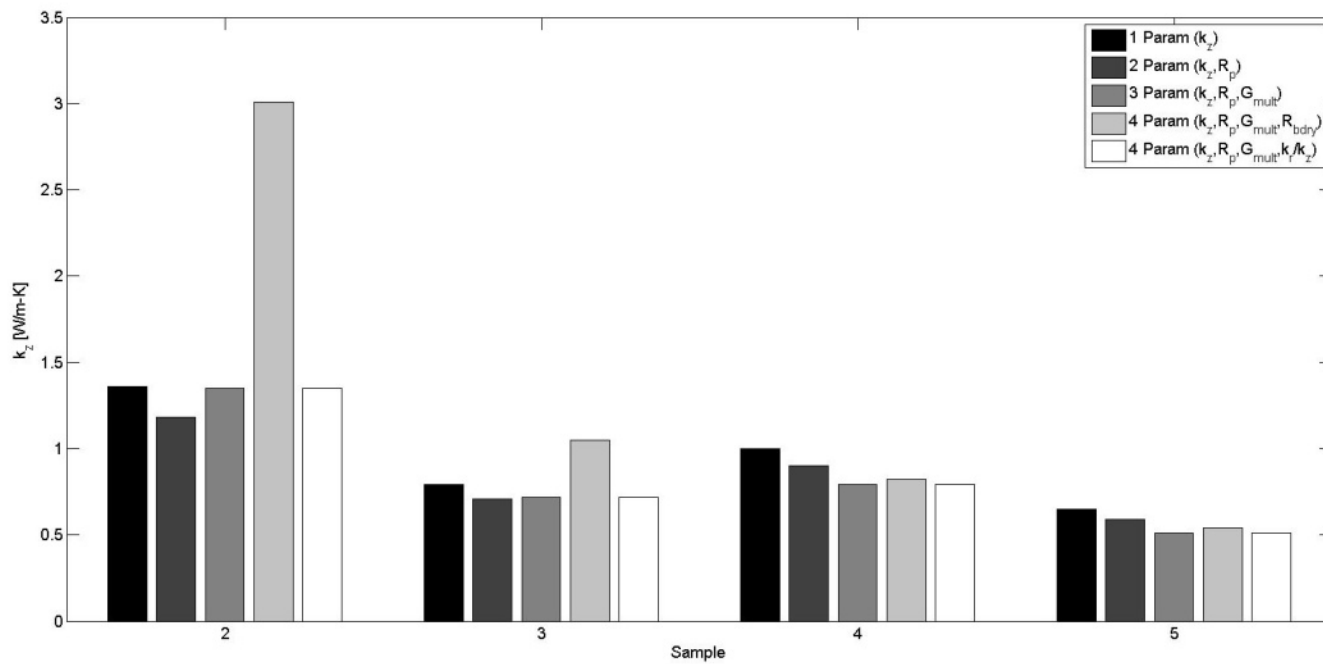


Figure 3-6: Estimation results for cross-plane thermal conductivity of ML samples

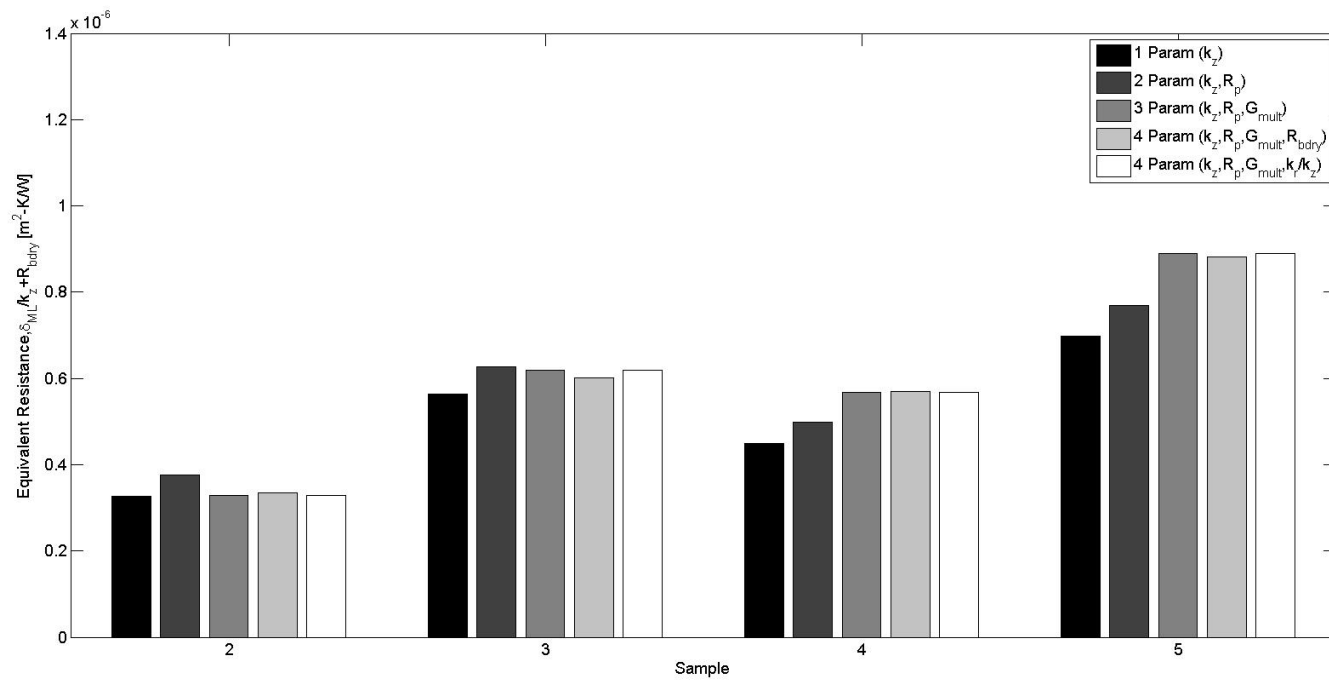


Figure 3-7: Equivalent thermal resistance of ML samples

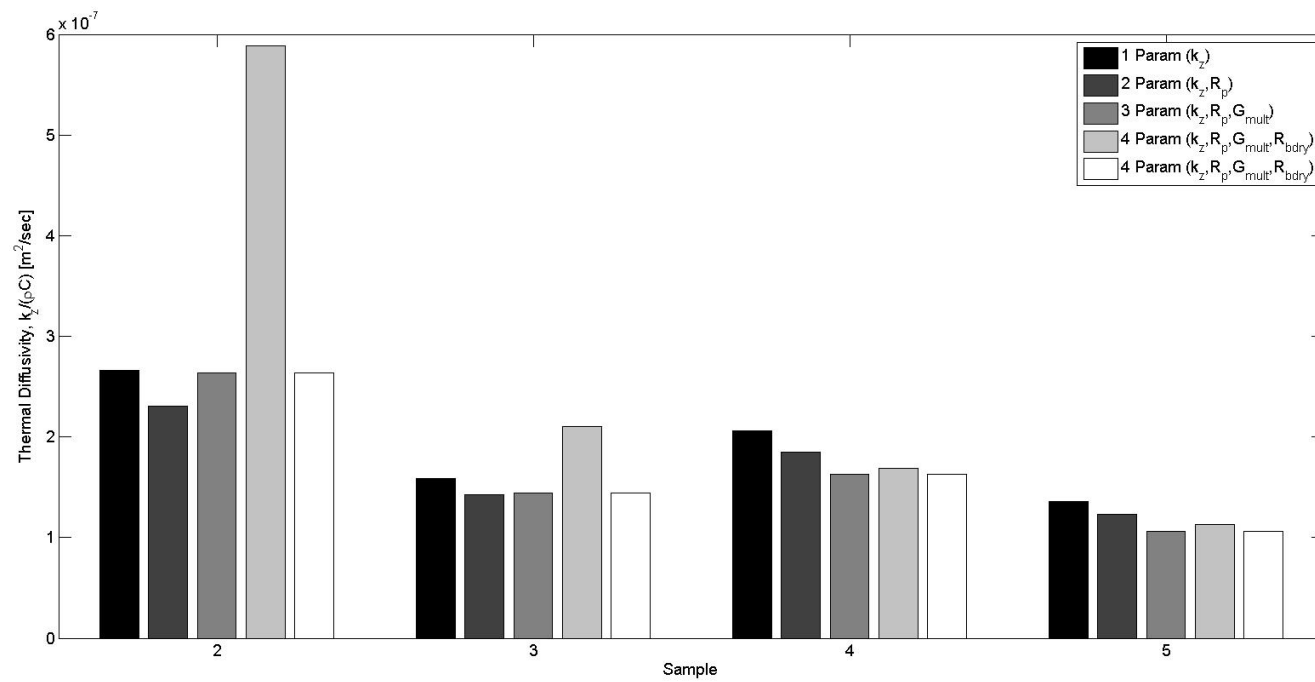


Figure 3-8: Thermal diffusivity of ML samples

appears on its own. k_r , on the other hand, never appears on its own. Due to this, it is possible (as seen in case 5) for us have sensitivity to k_z , but not to k_r or to the ratio of the two. For future work, it would be illustrative to show the Jacobian (Eq 2-7) of the model with respect to k_z , k_r , and k_r/k_z . The relative magnitudes of this quantity will be able to explain insensitivity to one or all of the parameters.

4. Conclusion

The thermal conductivity of a series of W/B4C ML samples has been evaluated using PDS data in a parameter estimation algorithm. Each of the samples has a cross-plane thermal conductivity that is smaller than the bulk value of its constituent layers. The thermal conductivity of these samples decreases slightly as the number of periods in the ML decreases. This was an unanticipated, although previously observed, occurrence. Due to the high degree of correlation between thermal contact resistance and cross-plane thermal conductivity, an effective thermal resistance across the ML was computed and observed to increase and the number of periods in the ML decreased. Results indicate that the measurements are insensitive to the anisotropy ratio of thermal conductivity for these ML samples.

REFERENCES

- [1] A. Kazimirov, D. M. Smilgies, Q. Shen, X. H. Xiao, Q. Hao, E. Fontes, D. H. Bilderback, S. M. Gruner, Y. Platonov, and V. V. Martynov, "Multilayer X-ray optics at CHESS," *Journal of Synchrotron Radiation*, vol. 13, pp. 204-210, 2006.
- [2] P. Revesz, A. Kazimirov, and I. Bazarov, "Optical measurement of thermal deformation of multilayer optics under synchrotron radiation," *Nuclear Instruments & Methods in Physics Research Section a-Accelerators Spectrometers Detectors and Associated Equipment*, vol. 582, pp. 142-145, 2007.
- [3] K. E. Goodson and Y. S. Ju, "Heat conduction in novel electronic films," *Annual Review of Materials Science*, vol. 29, pp. 261-293, 1999.
- [4] D. G. Cahill, W. K. Ford, K. E. Goodson, G. D. Mahan, A. Majumdar, H. J. Maris, R. Merlin, and S. R. Phillpot, "Nanoscale thermal transport," *Journal of Applied Physics*, vol. 93, pp. 793-818, 2003.
- [5] D. G. Cahill, K. Goodson, and A. Majumdar, "Thermometry and Thermal Transport in Micro/Nanoscale Solid-State Devices and Structures," *Journal of Heat Transfer*, vol. 124, pp. 223-241, 2002.
- [6] S. T. Huxtable, A. R. Abramson, and A. Majumdar, "Heat transport in superlattices and nanowires," in *Heat and Fluid Flow in Microscale and Nanoscale Structures*, M. Faghri and B. Sunden, Eds.: WIT Press, 2003.
- [7] R. K. Day, "THERMAL CONDUCTIVITY BY AXIAL FLOW-CUT BAR METHOD ASTM C408," *American Ceramic Society Bulletin*, vol. 45, pp. 753-&, 1966.
- [8] D. G. Cahill, "THERMAL-CONDUCTIVITY MEASUREMENT FROM 30-K TO 750-K - THE 3-OMEGA METHOD," *Review of Scientific Instruments*, vol. 61, pp. 802-808, Feb 1990.
- [9] S. M. Lee and D. G. Cahill, "Heat transport in thin dielectric films," *Journal of Applied Physics*, vol. 81, pp. 2590-2595, 1997.

- [10] S. M. Lee, D. G. Cahill, and T. H. Allen, "Thermal conductivity of sputtered oxide films," *Physical Review B*, vol. 52, pp. 253-257, 1995.
- [11] D. G. Cahill and T. H. Allen, "THERMAL-CONDUCTIVITY OF SPUTTERED AND EVAPORATED SiO₂ AND TiO₂ OPTICAL COATINGS," *Applied Physics Letters*, vol. 65, pp. 309-311, 1994.
- [12] S. M. Lee, D. G. Cahill, and R. Venkatasubramanian, "Thermal conductivity of Si-Ge superlattices," *Applied Physics Letters*, vol. 70, pp. 2957-2959, 1997.
- [13] S. T. Huxtable, A. Majumdar, C. Labounty, G. Zeng, J. Bowers, A. R. Abramson, C. L. Tien, X. Fan, P. Abraham, A. Shakouri, and E. T. Croke, "Nanoscale thermal transport in superlattices," in *2001 International Mechanical Engineering Conference and Exposition*, New York, New York, 2001, pp. 1-6.
- [14] T. Borca-Tasciuc, W. L. Liu, J. L. Liu, T. F. Zeng, D. W. Song, C. D. Moore, G. Chen, K. L. Wang, M. S. Goorsky, T. Radetic, R. Gronsky, T. Koga, and M. S. Dresselhaus, "Thermal conductivity of symmetrically strained Si/Ge superlattices," *Superlattices and Microstructures*, vol. 28, pp. 199-206, 2000.
- [15] T. Borca-Tasciuc, A. R. Kumar, and G. Chen, "Data reduction in 3 omega method for thin-film thermal conductivity determination," *Review of Scientific Instruments*, vol. 72, pp. 2139-2147, 2001.
- [16] G. Chen, C. L. Tien, X. Wu, and J. S. Smith, "THERMAL-DIFFUSIVITY MEASUREMENT OF GaAs/AlGaAs THIN-FILM STRUCTURES," *Journal of Heat Transfer-Transactions of the Asme*, vol. 116, pp. 325-331, 1994.
- [17] O. W. Kading, H. Skurk, and K. E. Goodson, "THERMAL CONDUCTION IN METALLIZED SILICON-DIOXIDE LAYERS ON SILICON," *Applied Physics Letters*, vol. 65, pp. 1629-1631, 1994.
- [18] R. J. Stevens, A. N. Smith, and P. M. Norris, "Measurement of thermal boundary conductance of a series of metal-dielectric interfaces by the transient thermoreflectance technique," *Journal of Heat Transfer-Transactions of the Asme*, vol. 127, pp. 315-322, 2005.

- [19] G. Langer, J. Hartmann, and M. Reichling, "Thermal conductivity of thin metallic films measured by photothermal profile analysis," *Review of Scientific Instruments*, vol. 68, pp. 1510-1513, 1997.
- [20] C. A. Paddock and G. L. Eesley, "TRANSIENT THERMOREFLECTANCE FROM THIN METAL-FILMS," *Journal of Applied Physics*, vol. 60, pp. 285-290, Jul 1986.
- [21] W. S. Capinski, H. J. Maris, T. Ruf, M. Cardona, K. Ploog, and D. S. Katzer, "Thermal-conductivity measurements of GaAs/AlAs superlattices using a picosecond optical pump-and-probe technique," *Physical Review B*, vol. 59, pp. 8105-8113, 1999.
- [22] T. Borca-Tasciuc and G. Chen, "Thin-film thermophysical property characterization by scanning laser thermoelectric microscope," *International Journal of Thermophysics*, vol. 19, pp. 557-567, 1998.
- [23] S. Callard, G. Tallarida, A. Borghesi, and L. Zanotti, "Thermal conductivity of SiO₂ films by scanning thermal microscopy," *Journal of Non-Crystalline Solids*, vol. 245, pp. 203-209, 1999.
- [24] M. Rohde, "PHOTOACOUSTIC CHARACTERIZATION OF THERMAL TRANSPORT-PROPERTIES IN THIN-FILMS AND MICROSTRUCTURES," *Thin Solid Films*, vol. 238, pp. 199-206, 1994.
- [25] P. K. Kuo, L. Wei, R. L. Thomas, and R. W. Pryor, "Thermal wave measurement of diamond films," *Photoacoustic and Photothermal Phenomena II*, vol. 62, pp. 124-126, 1990.
- [26] S. D. George, P. Radhakrishnan, V. P. N. Nampoori, and C. P. G. Vallabhan, "Photothermal deflection measurement on heat transport in GaAs epitaxial layers," *Physical Review B*, vol. 68, 2003.
- [27] E. J. Gonzalez, J. E. Bonevich, G. R. Stafford, G. White, and D. Josell, "Thermal transport through thin films: Mirage technique measurements on aluminum/titanium multilayers," *Journal of Materials Research*, vol. 15, pp. 764-771, 2000.

- [28] J. R. Foley, "Model-based estimation of the anisotropic thermal properties of materials from photothermal deflection spectroscopy data using Bayesian inference," Cornell University, Aug., 2007., 2007, pp. xvii, 353 leaves.
- [29] F. P. Incropera, *Introduction to heat transfer*, 5th ed. Hoboken, N.J.: J. Wiley, 2007.
- [30] H. O. Pierson and Knovel (Firm), "Handbook of refractory carbides and nitrides properties, characteristics, processing, and applications," in *Materials science and process technology series. Electronic materials and process technology* Park Ridge, N.J.: Noyes Publications, 1996, pp. xxii, 340 p.

APPENDIX A

Appendix A: Fourier and Hankel Transformations

We use the following definitions for the forward and inverse Fourier transforms

$$F(\theta_{n,j}) = \tilde{\theta}_{n,j} = \int_{t=-\infty}^{\infty} \theta_{n,j} e^{-i\omega t} dt \quad 1$$

$$F^{-1}(\tilde{\theta}_{n,j}) = \theta_{n,j} = \frac{1}{2\pi} \int_{\omega=-\infty}^{\infty} \tilde{\theta}_{n,j} e^{i\omega t} d\omega \quad 2$$

One of the features of the Fourier transform is the following transformation of time derivatives

$$F\left(\frac{\partial \theta_{n,j}}{\partial t}\right) = i\omega \tilde{\theta}_{n,j} \quad 3$$

We use the following definitions for the forward and inverse Hankel transforms

$$H(\theta_{n,j}) = \hat{\theta}_{n,j} = 2\pi \int_{r=0}^{\infty} r \theta_{n,j} J_0(\kappa r) dr \quad 4$$

$$H^{-1}(\hat{\theta}_{n,j}) = \theta_{n,j} = \frac{1}{2\pi} \int_{\kappa=0}^{\infty} \kappa \hat{\theta}_{n,j} J_0(\kappa r) d\kappa \quad 5$$

One of the features of the Hankel transform is the following transformation of the radial derivatives

$$H\left(\frac{\partial^2 \theta_{n,j}}{\partial r^2} + \frac{1}{r} \frac{\partial \theta_{n,j}}{\partial r}\right) = -\kappa^2 \hat{\theta}_{n,j} \quad 6$$

Fourier and Hankel transformations are linear operators, and may be applied in any order.

$$F(H(\theta_{n,j})) = H(F(\theta_{n,j})) = \tilde{\hat{\theta}}_{n,j} \quad 7$$

The energy equation (Eq 3, Chapter 1) is

$$k_{r,j} \frac{\partial^2 \theta_{n,j}}{\partial r^2} + \frac{k_{r,j}}{r} \frac{\partial \theta_{n,j}}{\partial r} + k_{z,j} \frac{\partial^2 \theta_{n,j}}{\partial z^2} + q_{n,j}''' = \rho_j C_j \frac{\partial \theta_{n,j}}{\partial t} \quad 8$$

Direct application of Eqs 3 and 6 to Eq 8 results in

$$k_{r,j} \left(-\kappa^2 \hat{\theta}_{n,j} \right) + k_{z,j} \frac{\partial^2 \hat{\theta}_{n,j}}{\partial z^2} + \hat{q}_{n,j}''' = \rho_j C_j i \omega \hat{\theta}_{n,j} \quad 9$$

which may be restructured as

$$\frac{\partial^2 \hat{\theta}_{n,j}}{\partial z^2} - \left(\kappa^2 \frac{k_{r,j}}{k_{z,j}} + i \omega \frac{\rho_j C_j}{k_{z,j}} \right) \hat{\theta}_{n,j} = - \frac{\hat{q}_{n,j}'''}{k_{z,j}} \quad 10$$

Since differentiation is now in the z-direction only, we may replace the partial derivatives with ordinary derivatives.

$$\frac{d^2 \hat{\theta}_{n,j}}{dz^2} - \left(\kappa^2 \frac{k_{r,j}}{k_{z,j}} + i \omega \frac{\rho_j C_j}{k_{z,j}} \right) \hat{\theta}_{n,j} = - \frac{\hat{q}_{n,j}'''}{k_{z,j}} \quad 11$$

which is the form given in (Eq 6, Chapter 1).

APPENDIX B

APPENDIX B: Fourier Transformation of a Real-Valued Sinusoidal Function

We will define an arbitrary sinusoidal function to have an amplitude A , circular frequency ω_n , and phase ϕ .

$$f(t) = A \sin(\omega_n t + \phi) \quad 1$$

Expressing the sin in terms of exponentials, one obtains

$$f(t) = A \left(\frac{e^{i(\omega_n t + \phi)} + e^{-i(\omega_n t + \phi)}}{2i} \right) \quad 2$$

This may be expanded as

$$f(t) = A e^{i\phi} \frac{e^{i\omega_n t}}{2i} - A e^{-i\phi} \frac{e^{-i\omega_n t}}{2i} \quad 3$$

The functions $A e^{i\phi}$ and $A e^{-i\phi}$ are, by definition, complex conjugates of each other

$$A e^{-i\phi} = (A e^{i\phi})^* \quad 4$$

Taking the Fourier transform of Eq 3, one obtains

$$\tilde{f}(\omega) = A e^{i\phi} \int_{t=-\infty}^{\infty} \frac{e^{-i(\omega - \omega_n)t}}{2i} dt - A e^{-i\phi} \int_{t=-\infty}^{\infty} \frac{e^{-i(\omega + \omega_n)t}}{2i} dt \quad 5$$

Orthogonality of the exponentials results in

$$\tilde{f}(\omega) = A e^{i\phi} \frac{2\pi}{2i} \delta(\omega - \omega_n) - A e^{-i\phi} \frac{2\pi}{2i} \delta(\omega + \omega_n) \quad 6$$

Because of the Dirac delta function, the only non-zero values of Eq 6 exist at

$$\omega = \pm \omega_n .$$

$$\tilde{f}(\omega_n) = A e^{i\phi} \frac{2\pi}{2i} \delta(\omega - \omega_n) \quad 7$$

$$\tilde{f}(-\omega_n) = -A e^{-i\phi} \frac{2\pi}{2i} \delta(\omega + \omega_n) \quad 8$$

This indicates that

$$\tilde{f}(-\omega_n) = -\tilde{f}(\omega_n)^* \quad 9$$

Therefore, it is only necessary to solve for one of the constituent frequencies (i.e. $\omega = \omega_n$) since the other (i.e. $\omega = -\omega_n$) is the complex conjugate. We will apply this toward the transformed temperature field (i.e. $\hat{\theta}$).

APPENDIX C

APPENDIX C: Probe Beam Deflection Equations

Due to the significant amount of math required to develop the intensity-averaged probe beam deflection equations, much of the work was omitted from Chapter 1. It is provided here in detail. Since the results for the normal component of the deflection closely resemble those for the tangential component, we will concentrate our discussion on the tangential component and note differences when they occur.

The tangential component of the deflection of a single ray from Eq 14 (Chapter 1) is

$$\Phi_{\text{tan},n} = \frac{1}{n_0} \frac{dn}{dT} \int_{y=-\infty}^{\infty} \frac{\partial \theta_{n,j=1}}{\partial x} dy \quad 1$$

Applying Leibniz Rule, we may move the partial derivative outside of the integration.

$$\Phi_{\text{tan},n} = \frac{1}{n_0} \frac{dn}{dT} \frac{\partial}{\partial x} \int_{y=-\infty}^{\infty} \theta_{n,j=1} dy \quad 2$$

From Eq 12 (Chapter 1), the temperature field was reported as

$$\theta_{n,j=1} = \frac{1}{2\pi} \int_{\omega=-\infty}^{\infty} \left[\frac{1}{2\pi} \int_{\kappa=0}^{\infty} \kappa \hat{\theta}_{n,j=1} J_0(\kappa r) d\kappa \right] e^{i\omega t} d\omega \quad 3$$

Inserting Eq 3 into Eq 2

$$\Phi_{\text{tan},n} = \frac{1}{n_0} \frac{dn}{dT} \frac{\partial}{\partial x} \int_{y=-\infty}^{\infty} \frac{1}{2\pi} \int_{\omega=-\infty}^{\infty} \left[\frac{1}{2\pi} \int_{\kappa=0}^{\infty} \kappa \hat{\theta}_{n,j=1} J_0(\kappa r) d\kappa \right] e^{i\omega t} d\omega dy \quad 4$$

Rearranging Eq 4 into a more recognizable form

$$\Phi_{\text{tan},n} = \frac{1}{2\pi} \int_{\omega=-\infty}^{\infty} \left(\frac{1}{n_0} \frac{dn}{dT} \frac{\partial}{\partial x} \int_{y=-\infty}^{\infty} \left[\frac{1}{2\pi} \int_{\kappa=0}^{\infty} \kappa \hat{\theta}_{n,j=1} J_0(\kappa r) d\kappa \right] dy \right) e^{i\omega t} d\omega \quad 5$$

Since the outermost integration in Eq 5 is an inverse Fourier transform (in the $\omega \rightarrow t$ direction), it is reasonable to call

$$\tilde{\Phi}_{\text{tan},n} = \frac{1}{n_0} \frac{dn}{dT} \frac{\partial}{\partial x} \int_{y=-\infty}^{\infty} \left[\frac{1}{2\pi} \int_{\kappa=0}^{\infty} \kappa \hat{\theta}_{n,j=1} J_0(\kappa r) d\kappa \right] dy \quad 6$$

Changing the order of y-integration in Eq 6

$$\tilde{\Phi}_{\tan,n} = \frac{1}{n_0} \frac{dn}{dT} \frac{\partial}{\partial x} \frac{1}{2\pi} \int_{\kappa=0}^{\infty} \kappa \hat{\theta}_{n,j=1} \left[\int_{y=-\infty}^{\infty} J_0(\kappa r) dy \right] d\kappa \quad 7$$

Recognizing that

$$r = \sqrt{x^2 + y^2} \quad 8$$

The integral

$$\int_{y=-\infty}^{\infty} J_0(\kappa \sqrt{x^2 + y^2}) dy = \frac{\cos(\kappa x)}{\kappa} \quad 9$$

which Reduces Eq 7 to

$$\tilde{\Phi}_{\tan,n} = \frac{1}{n_0} \frac{dn}{dT} \frac{\partial}{\partial x} \frac{1}{2\pi} \int_{\kappa=0}^{\infty} \hat{\theta}_{n,j=1} \cos(\kappa x) d\kappa \quad 10$$

The function $\hat{\theta}_{n,j=1}$ has even symmetry with respect to κ , therefore

$$\frac{1}{2\pi} \int_{\kappa=0}^{\infty} \hat{\theta}_{n,j=1} \cos(\kappa x) d\kappa = \frac{1}{2} \left(\frac{1}{2\pi} \int_{\kappa=-\infty}^{\infty} \hat{\theta}_{n,j=1} e^{i\kappa x} d\kappa \right) \quad 11$$

We recognize that Eq 11 contains the inverse Fourier transform of $\hat{\theta}_{n,j=1}$ in the $\kappa \rightarrow x$ (rather than $\omega \rightarrow t$ dimensions).

Eq 10 becomes

$$\tilde{\Phi}_{\tan,n} = \frac{1}{n_0} \frac{dn}{dT} \frac{\partial}{\partial x} \frac{1}{2} \left[\frac{1}{2\pi} \int_{\kappa=-\infty}^{\infty} \hat{\theta}_{n,j=1} e^{i\kappa x} d\kappa \right] \quad 12$$

Carrying through the partial derivative in Eq 12

$$\tilde{\Phi}_{\tan,n} = \frac{1}{n_0} \frac{dn}{dT} \frac{1}{2} \left[\frac{1}{2\pi} \int_{\kappa=-\infty}^{\infty} i\kappa \hat{\theta}_{n,j=1} e^{i\kappa x} d\kappa \right] \quad 13$$

Analogous arguments can be made for the tangential direction, resulting in

$$\tilde{\Phi}_{norm,n} = -\frac{1}{n_0} \frac{dn}{dT} \frac{1}{2} \left[\frac{1}{2\pi} \int_{\kappa=-\infty}^{\infty} \Lambda_{j=1} \hat{\theta}_{n,j=1} e^{i\kappa x} d\kappa \right] \quad 14$$

Eqs 14 and 15 (Chapter 1) become

$$\Phi_{\tan,n} = \frac{1}{2\pi} \int_{\omega=-\infty}^{\infty} \tilde{\Phi}_{\tan,n} e^{i\omega t} d\omega \quad 15$$

$$\Phi_{norm,n} = \frac{1}{2\pi} \int_{\omega=-\infty}^{\infty} \tilde{\Phi}_{norm,n} e^{i\omega t} d\omega \quad 16$$

Eq 16 (Chapter 1) deals with the convolution of the probe beam with the deflection of a single ray.

$$\bar{\Phi}_{\text{norm,tan},n} = \frac{1}{P_p} \int_{z=0}^{\infty} \int_{x=-\infty}^{\infty} I_p \Phi_{\text{norm,tan},n} dx dz \quad 17$$

The integration of the x-direction is a straightforward application of Fourier convolution theory

$$\int_{x=-\infty}^{\infty} I_p \Phi_{\text{norm,tan},n} dx = F^{-1} \left(F \left[I_p \right] F \left[\Phi_{\text{norm,tan},n} \right] \right) \quad 18$$

Where the indicated Fourier transforms are in the $x \rightarrow \kappa$ direction

$$F \left[I_p \right] = \frac{\sqrt{2} P_p}{\sqrt{\pi} R_p} \left(e^{-\frac{2(z-h)^2}{R_p^2}} + e^{-\frac{2(z+h)^2}{R_p^2}} \right) e^{-\frac{\kappa^2 R_p^2}{8}} \quad 19$$

$$F \left[\Phi_{\text{norm,tan},n} \right] = \Phi_{\text{tan},n} = \frac{1}{2\pi} \int_{\omega=-\infty}^{\infty} F \left[\tilde{\Phi}_{\text{norm,tan},n} \right] e^{i\omega t} d\omega \quad 20$$

$$F \left[\tilde{\Phi}_{\text{tan},n} \right] = \frac{1}{n_0} \frac{dn}{dT} \frac{1}{2} i \kappa \hat{\theta}_{n,j=1} \quad 21$$

$$F \left[\tilde{\Phi}_{\text{norm},n} \right] = -\frac{1}{n_0} \frac{dn}{dT} \frac{1}{2} \Lambda_{j=1} \hat{\theta}_{n,j=1} \quad 22$$

From Eq 9 (Chapter 1), the transformed temperature field in the j=1 layer is

$$\hat{\theta}_{n,j=1} = c_{2,n,j=1} e^{-\Lambda_{j=1} \left(z - z_{\text{bot},j} \right) - \frac{\kappa^2 R_h^2}{8}} \quad 23$$

Therefore, Eq 18 becomes

$$F^{-1} \left(F \left[I_p \right] F \left[\Phi_{\text{tan},n} \right] \right) = \frac{1}{2\pi} \int_{\omega=-\infty}^{\infty} \left\{ \frac{1}{n_0} \frac{dn}{dT} \frac{1}{2} \frac{\sqrt{2} P_p}{\sqrt{\pi} R_p} \left(e^{-\frac{2(z-h)^2}{R_p^2}} + e^{-\frac{2(z+h)^2}{R_p^2}} \right) \dots \right. \quad 24$$

$$\left. \left[\frac{1}{2\pi} \int_{\kappa=-\infty}^{\infty} i \kappa c_{2,n,j=1} e^{-\Lambda_{j=1} z - \frac{\kappa^2 (R_n^2 + R_p^2)}{8}} e^{i\kappa x} d\kappa \right] \right\} e^{i\omega t}$$

and

$$F^{-1}\left(F\left[I_p\right]F\left[\Phi_{\text{norm},n}\right]\right)=\frac{1}{2\pi}\int_{\omega=-\infty}^{\infty}\left\{\frac{1}{n_0}\frac{dn}{dT}\frac{1}{2}\frac{\sqrt{2}P_p}{\sqrt{\pi}R_p}\left(e^{\frac{-2(z-h)^2}{R_p^2}}+e^{\frac{-2(z+h)^2}{R_p^2}}\right)\dots\right. \\ \left.\left[\frac{1}{2\pi}\int_{\kappa=-\infty}^{\infty}\Lambda_{j=1}c_{2_{n,j=1}}e^{-\Lambda_{j=1}z-\frac{\kappa^2(R_h^2+R_p^2)}{8}}e^{i\kappa x}d\kappa\right]\right\}e^{i\omega t} \quad 25$$

Incorporating the remaining z -integration in Eq 17, we recover the Eqs 18 and 19 (Chapter 1).

$$\bar{\Phi}_{\text{tan},n}=\frac{1}{2\pi}\int_{\omega=-\infty}^{\infty}\left\{\frac{1}{n_0}\frac{dn}{dT}\frac{1}{2}\int_{z=0}^{\infty}\frac{\sqrt{2}}{\sqrt{\pi}R_p}\left(e^{\frac{-2(z-h)^2}{R_p^2}}+e^{\frac{-2(z+h)^2}{R_p^2}}\right)\dots\right. \\ \left.\left[\frac{1}{2\pi}\int_{\kappa=-\infty}^{\infty}i\kappa c_{2_{n,j=1}}e^{-\Lambda_{j=1}z-\frac{\kappa^2(R_h^2+R_p^2)}{8}}e^{i\kappa x}d\kappa\right]dz\right\}e^{i\omega t}d\omega \quad 26$$

and

$$\bar{\Phi}_{\text{norm},n}=\frac{1}{2\pi}\int_{\omega=-\infty}^{\infty}\left\{\frac{1}{n_0}\frac{dn}{dT}\frac{1}{2}\int_{z=0}^{\infty}\frac{\sqrt{2}}{\sqrt{\pi}R_p}\left(e^{\frac{-2(z-h)^2}{R_p^2}}\pm e^{\frac{-2(z+h)^2}{R_p^2}}\right)\dots\right. \\ \left.\left[\frac{1}{2\pi}\int_{\kappa=-\infty}^{\infty}\Lambda_{j=1}c_{2_{n,j=1}}e^{-\Lambda_{j=1}z-\frac{\kappa^2(R_h^2+R_p^2)}{8}}e^{i\kappa x}d\kappa\right]dz\right\}e^{i\omega t}d\omega \quad 27$$

Note that in Eq 27 we have re-introduced the \pm sign. The rationale for this was discussed in Chapter 1.

APPENDIX D

APPENDIX D: Z-integration of Probe Beam Deflection Equations

In practice, we use a trapezoidal rule numerical integration scheme to solve the z-integration term in Eqs 18 and 19 (Chapter 1). There is an analytical solution to these integrals, but it is not possible using MATLAB.

An integral will be encountered of the form

$$\int_{z=0}^{\infty} e^{-\Lambda_{j=1}z - \frac{2(z \pm h)^2}{R_p^2}} dz = \frac{R_p \sqrt{\pi}}{2\sqrt{2}} e^{-\frac{2h^2}{R_p^2} + Z^2} \operatorname{erfc}(Z) \quad 1$$

where

$$\operatorname{erfc}(Z) = \frac{2}{\sqrt{\pi}} \int_{t=Z}^{\infty} e^{-t^2} dt \quad 2$$

and

$$Z = \frac{R_p \Lambda_{j=1}}{2} \pm \frac{\sqrt{2}h}{R_p} \quad 3$$

Although MATLAB has an ERFC command, it does not accept arguments which are complex-valued. This is because ERFC has a limited radius of convergence in the complex plane. For points outside of this radius, it is necessary to use a technique called “analytic continuation” [1] to obtain a solution for Eq 2.

[1] M. D. Greenberg, *Advanced engineering mathematics*, 2nd ed. Upper Saddle River, N.J.: Prentice Hall, 1998.

APPENDIX E

APPENDIX E: Calibration of Quadrant Photodetector

We have performed a calibration of the quadrant photodetector (QPD) by scanning the probe beam across the face of the QPD and recording the normalized voltage output at each position. The normalization consists of dividing the difference of the voltages from the right and left-hand quadrants by the sum of the voltages from all four quadrants (Figure 1).

$$Sig_{norm}(x) = \frac{V_{(\mathcal{Q}_1+\mathcal{Q}_4)}(x) - V_{(\mathcal{Q}_2+\mathcal{Q}_3)}(x)}{V_{(\mathcal{Q}_1+\mathcal{Q}_2+\mathcal{Q}_3+\mathcal{Q}_4)}} \quad 1$$

The slope of this relationship represents a conversion factor between linear displacements and the normalized signal. From our calibration (Figure 2), the slope is $d(Sig_{norm})/dx = 1000.4 \text{ m}^{-1}$. We are interested, however, in measuring angular displacements rather than linear displacements (Figure 3). The trigonometric relationship which allows us to convert between the two is

$$\tan(d\Phi) = \frac{dx}{l_{QPD}} \quad 2$$

where l_{QPD} is the distance between the heated spot (i.e. where the deflection occurs) and the QPD. In our experiment, this distance is approximately 180 mm. Employing the small angle approximation for tangent, we may re-write Eq 2 as

$$dx \approx l_{QPD} d\Phi \quad 3$$

The normalized signal which would result from an angular deflection is therefore

$$d(Sig_{norm}) = \frac{d(Sig_{norm})}{dx} dx = \frac{d(Sig_{norm})}{dx} l_{QPD} d\Phi \quad 4$$

The gain, or conversion factor between angular deflections and normalized signals is therefore

$$Gain = \frac{d(Sig_{norm})}{d\Phi} = \frac{d(Sig_{norm})}{dx} l_{QPD} \quad 5$$

In our experiment, the gain factor has a value of 180.07 rad^{-1} .

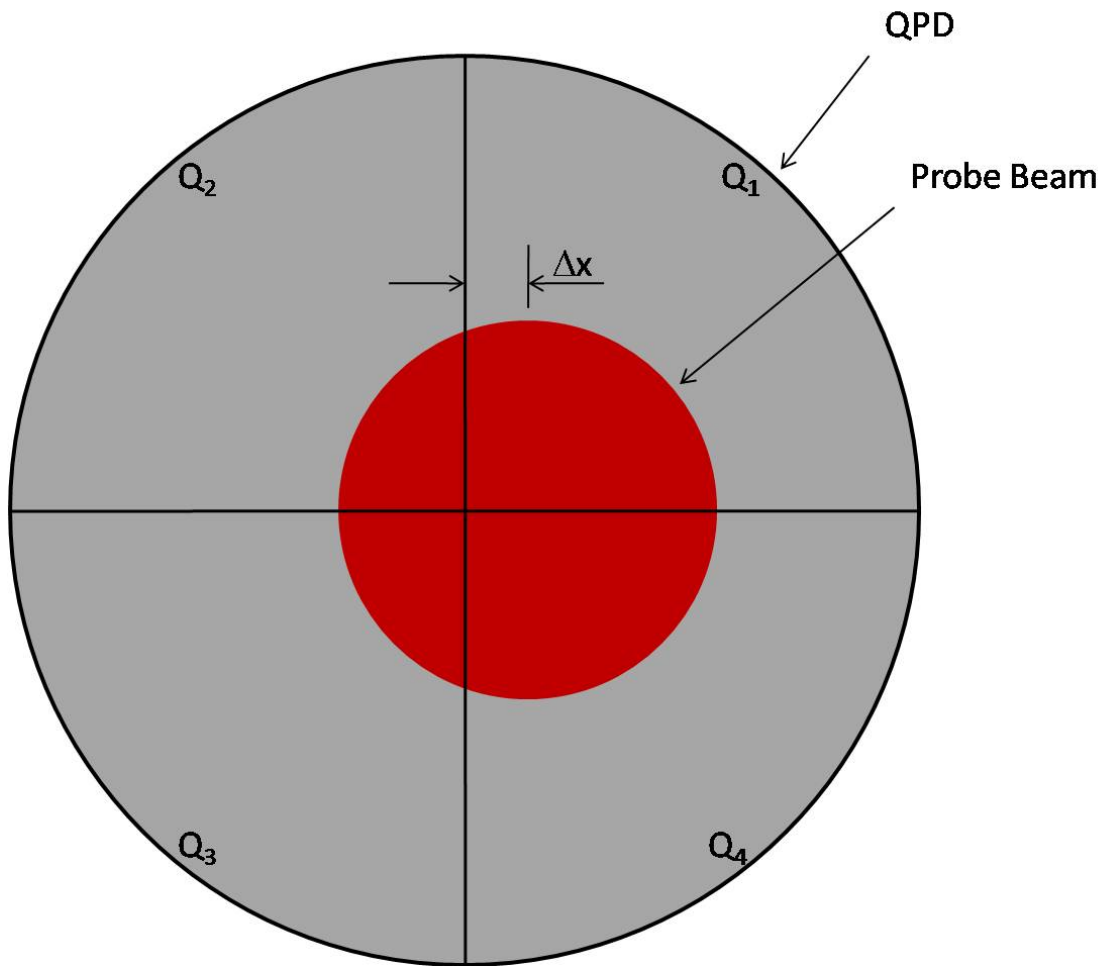


Figure 1: Schematic of quadrant photodetector calibration (front view)

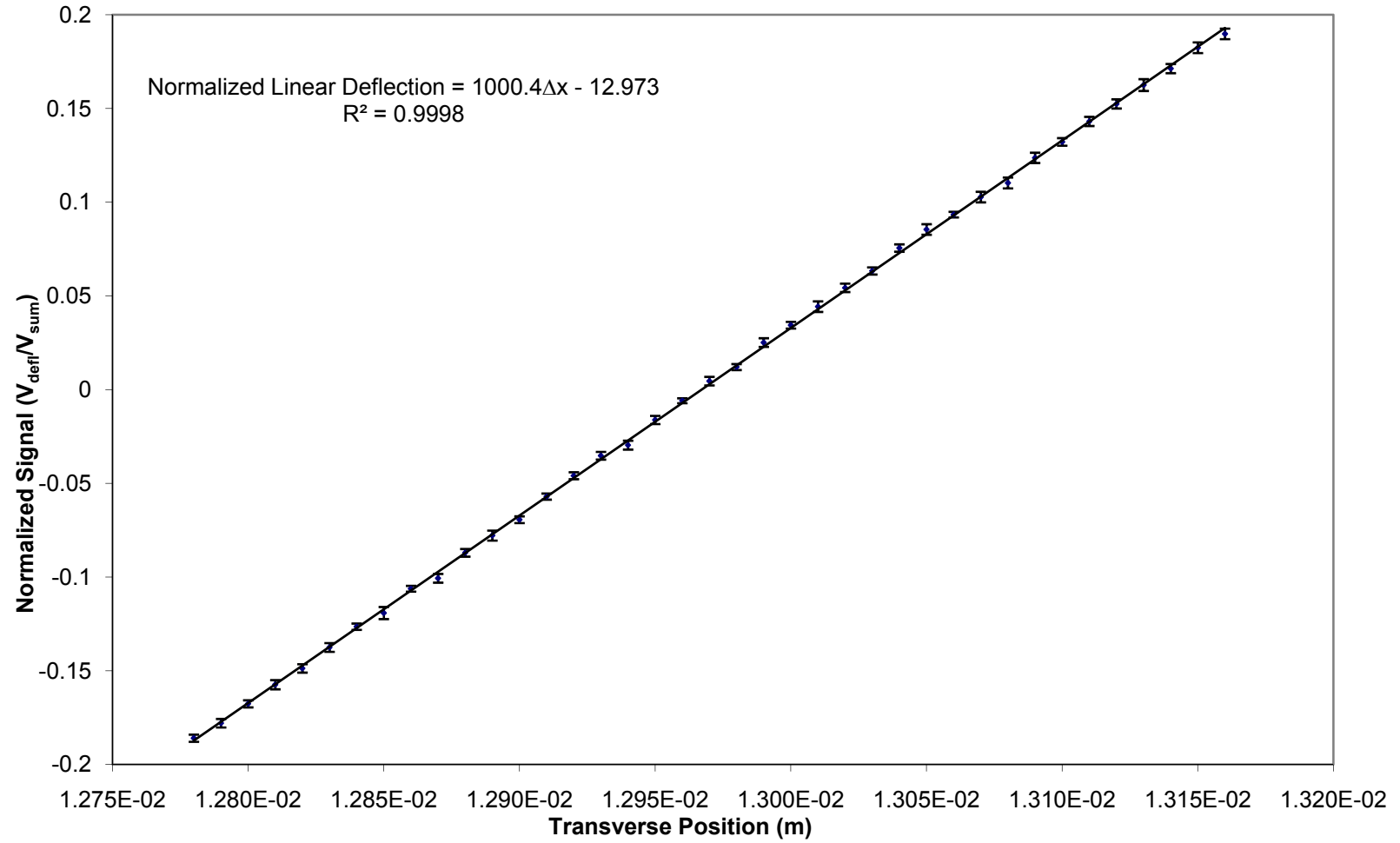


Figure 2: Results of quadrant photodetector calibration

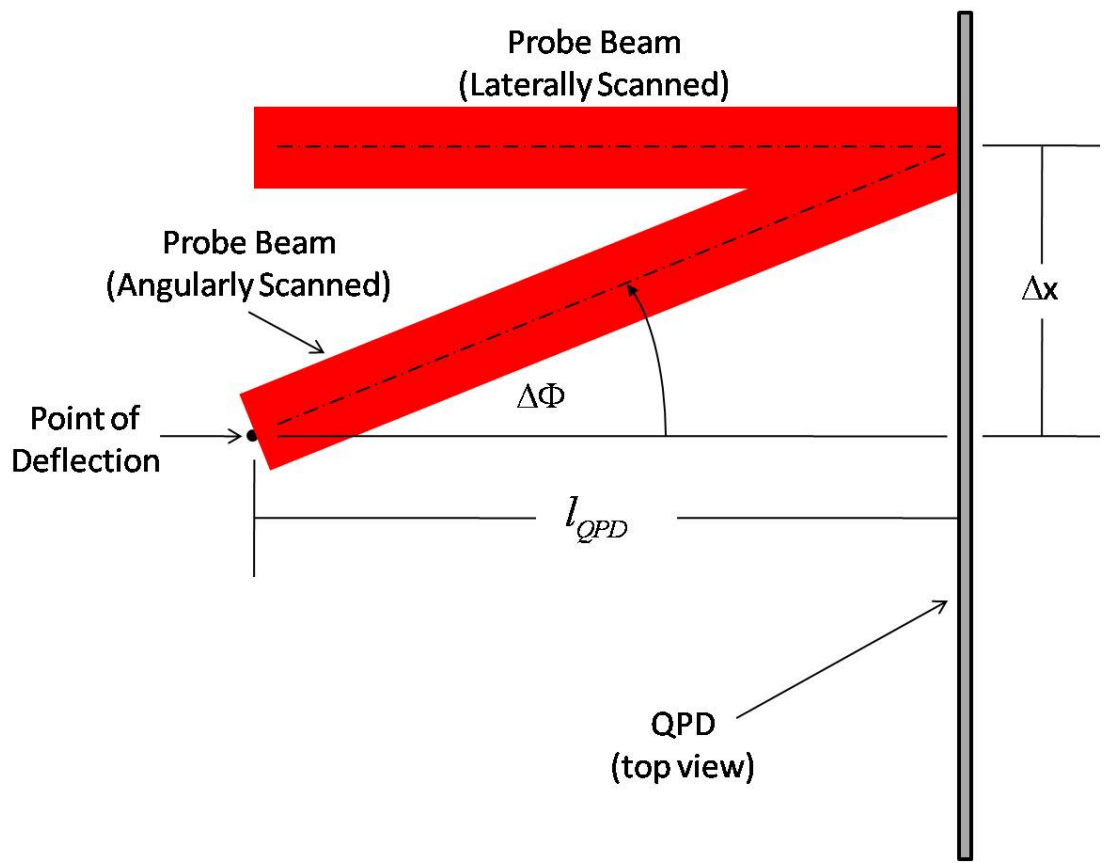


Figure 3: Schematic of quadrant photodetector calibration (top view)

APPENDIX F

APPENDIX F: Relative Probe Beam Size

One of the important features of thermal wave techniques is their ability to confine the thermal probe to small length-scales by increasing the modulation frequency of the applied heat source. This is the primary reason why such techniques are valuable when working with thin films and multilayer structures. One of the issues we have encountered with PDS, however, is that we lose sensitivity to model parameters at very high modulation frequencies. The reason is relatively straight forward, but there is no obvious solution.

The films we are interested in typically have a thickness on the order of 1 μm . Ideally, we would like to operate at sufficiently high frequencies to contain the thermal field inside of the film (Figure 1). This means that the thermal field will also be on the order of 1 μm . Unfortunately, our probe beam has a radius of 23.9 μm , so a large portion of the probe beam will be unaffected by the presence of the thermal field, resulting in a poor signal-to-noise ratio.

It seems evident that one should use a smaller probe beam. There are two major problems with that premise: 1.) it is only possible to focus light to the order of its wavelength, 2.) the shorter the focal length of the lens, the shorter the depth of focus (leading to decreased collimation lengths and increased alignment difficulty). This is in addition to the more practical matter that there may be insufficient physical clearance to accommodate the necessary optics.

Ideally, we would like to encounter a situation where $l_{pd} < \delta_{film}$ and $R_p \ll l_{pd}$. Unfortunately, it does not appear that transverse PDS can handle these conditions simultaneously when dealing with thin films or multilayer structures. Fortunately, this is not a “binary” problem. Loss of sensitivity is gradual rather than instantaneous. We have found that we still have sensitivity to the properties of a film when the thermal penetration depth is larger than the film thickness.

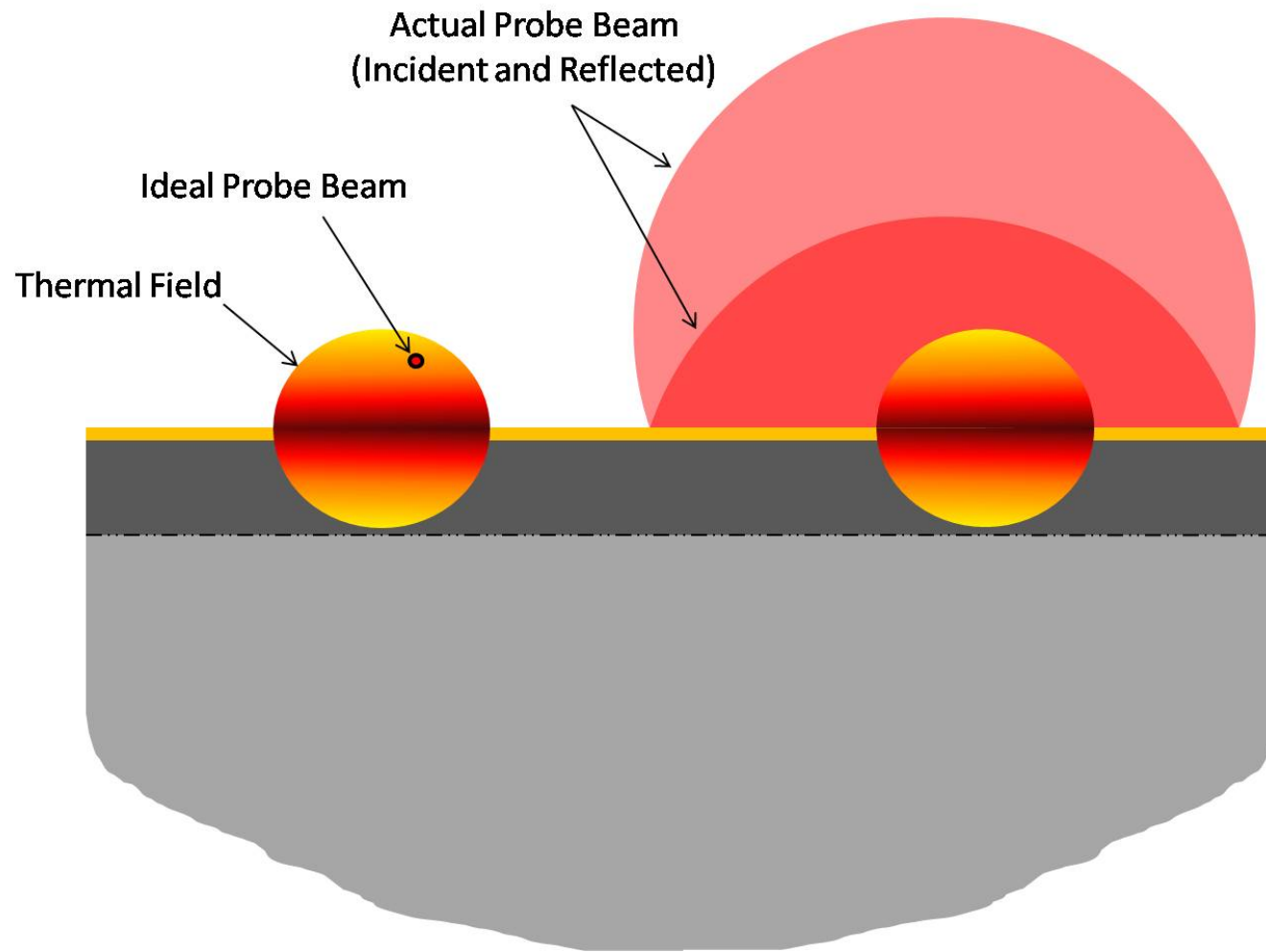


Figure 1: Relative size of film, thermal field, and probe beam

APPENDIX G

APPENDIX G: Probe Beam Collimation

We have assumed that the probe beam is collimated as it passes through the thermal field. In actuality, the probe beam has regions of convergence, collimation, and divergence (Figure 1). The integrals found in Eqs 14 and 15 (Chapter 1) are evaluated from negative infinity to positive infinity in the y-direction. We may break these up into three regions (written for the tangential direction only, but applicable normal direction as well).

$$\Phi_{\tan,n} = \frac{1}{n_0} \frac{dn}{dT} \left(\int_{\text{convergence region}} \frac{\partial \theta_{n,j=1}}{dx} dy + \int_{\text{collimation region}} \frac{\partial \theta_{n,j=1}}{dx} dy + \int_{\text{divergence region}} \frac{\partial \theta_{n,j=1}}{dx} dy \right) \quad 1$$

Our implicit assumption is that there are no temperature gradients in the convergence or divergence regions, such that

$$\int_{\text{convergence region}} \frac{\partial \theta_{n,j=1}}{dx} dy = \int_{\text{divergence region}} \frac{\partial \theta_{n,j=1}}{dx} dy = 0 \quad 2$$

The length of the collimation region may be approximated by the depth of focus, which is given by

$$DOF = \left(\frac{8\lambda}{\pi} \right) \left(\frac{f}{D} \right)^2 \quad 3$$

where λ is the wavelength of the laser, f is the focal length of the lens, and D is the diameter ($1/e^2$) of the light entering the lens. Over this region, the radius increases by a factor of $\sqrt{2}$ over its value at the waist. In other words, the probe beam is never “perfectly” collimated. Using the parameters of our experiment ($f = 25.4$ mm, $\lambda = 632.8$ nm, $D = 0.48$ mm), the DOF is approximately 4.5 mm.

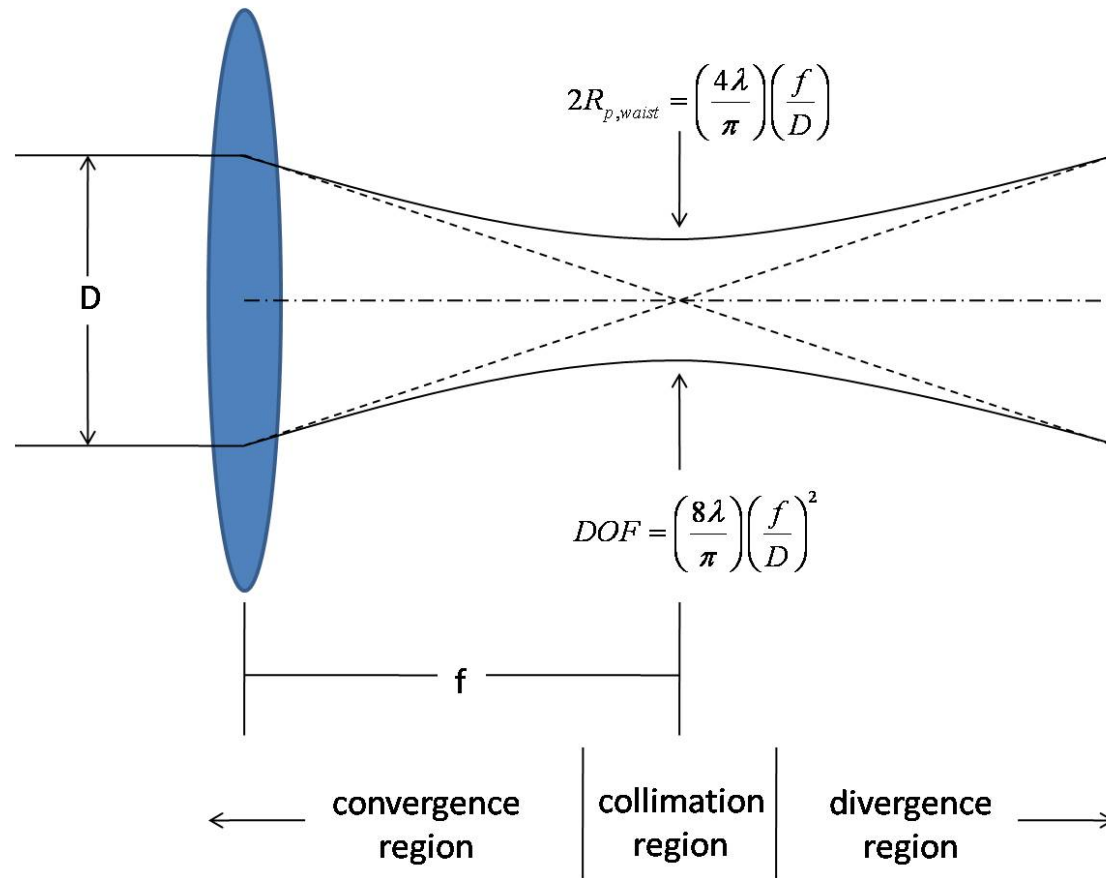


Figure 1: Convergence, collimation, and divergence regions of probe beam

APPENDIX H

APPENDIX H: Analysis of Bulk Materials

Although the focus of our work has been on thin films and multi-layered structures, our techniques are equally valid when applied to bulk materials. Our multi-layer model may be used by setting the number of layers to two (2), where $j = 1$ is the semi-infinite gas phase and $j = 2$ is the semi-infinite bulk solid phase. The estimation algorithm was developed in such a general manner that it may be used for bulk, film-on-substrate, or multi-layer systems. The only minor difference lies in applying the “black box” estimation procedure. We will discuss our previous efforts toward determining the thermal conductivity of NIST SRM8421 and SRM1462.

For a bulk material, we are primarily interested in obtaining the isotropic thermal conductivity. The first step in our procedure is to take an initial step toward reducing the residual difference between the measurements and the model. As with the film, we will select a series of “initial guesses” for thermal conductivity, and allow that parameter to “float” by itself in the estimation algorithm, assuming that all other parameters are known precisely (i.e. $\mathbf{s} = [k_z]$). The initial guesses ranged from 0.1 W/m-K to 1000 W/m-K with a diffuse prior uncertainty. In all cases, the final estimate was 90.94 W/m-K for SRM8421 (Figure 1) and 15.82 W/m-K for SRM1462. Figure 2 shows the cost function for each iteration at each initial guess. We believe that these values represent a global minima in the cost function, but to verify that this is the case we have plotted the cost function for all possible values of k_z (for SRM8421 only) in Figure 3. A minima of the cost function is evident at the same location predicted by the estimation algorithm. Although this procedure is possible for one or two model parameters, the computational time becomes prohibitive and visualization becomes difficult for a larger number of parameters. This is precisely the reason why estimation algorithms are valuable.

We make no claim that the resulting values are the “correct” values for thermal conductivity, as other model parameters may not be known accurately. We have found that letting the probe beam radius and gain act as floating parameters along with thermal conductivity, we are able to achieve better agreement with the data than by letting thermal conductivity float by itself. For the second step of our process, we initialize the estimation algorithm with the value for k_z from the previous step (i.e. $k_z = 90.94$ W/m-K for SRM8421 and $k_z = 15.82$ W/m-K for SRM1462), and *a priori* values for the probe beam radius ($R_p = 23.9$ μm) and gain (gain = 180 rad^{-1}). We note that the single value for gain used here is in lieu of the “gain multiplier” discussed in Chapter 1. Therefore, a final value of gain = 162 rad^{-1} is equivalent to reporting a gain multiplier of $G_{mult} = 162 \text{ rad}^{-1} / 180 \text{ rad}^{-1} = 0.9$. To remind the reader, the gain multiplier was used to account for the effects of uncertainty or imperfect knowledge in any term that is a linear multiplier of the probe beam deflection signal. The results of this 3-parameter estimation have previously been given in Chapter 1, Table 2, Case 3.

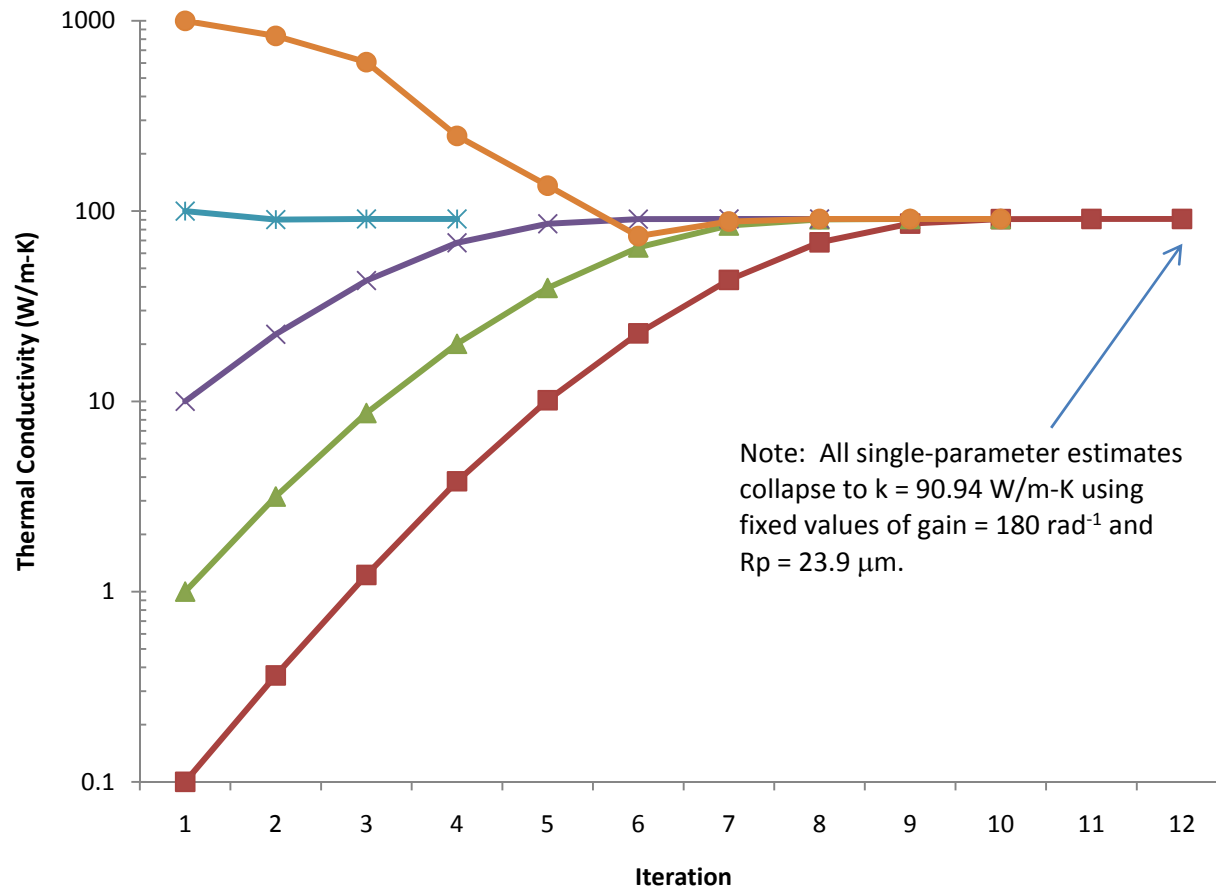


Figure 1: Results of estimation algorithm for SRM8421 with several initial guesses for thermal conductivity in a one-parameter (k_z) fit

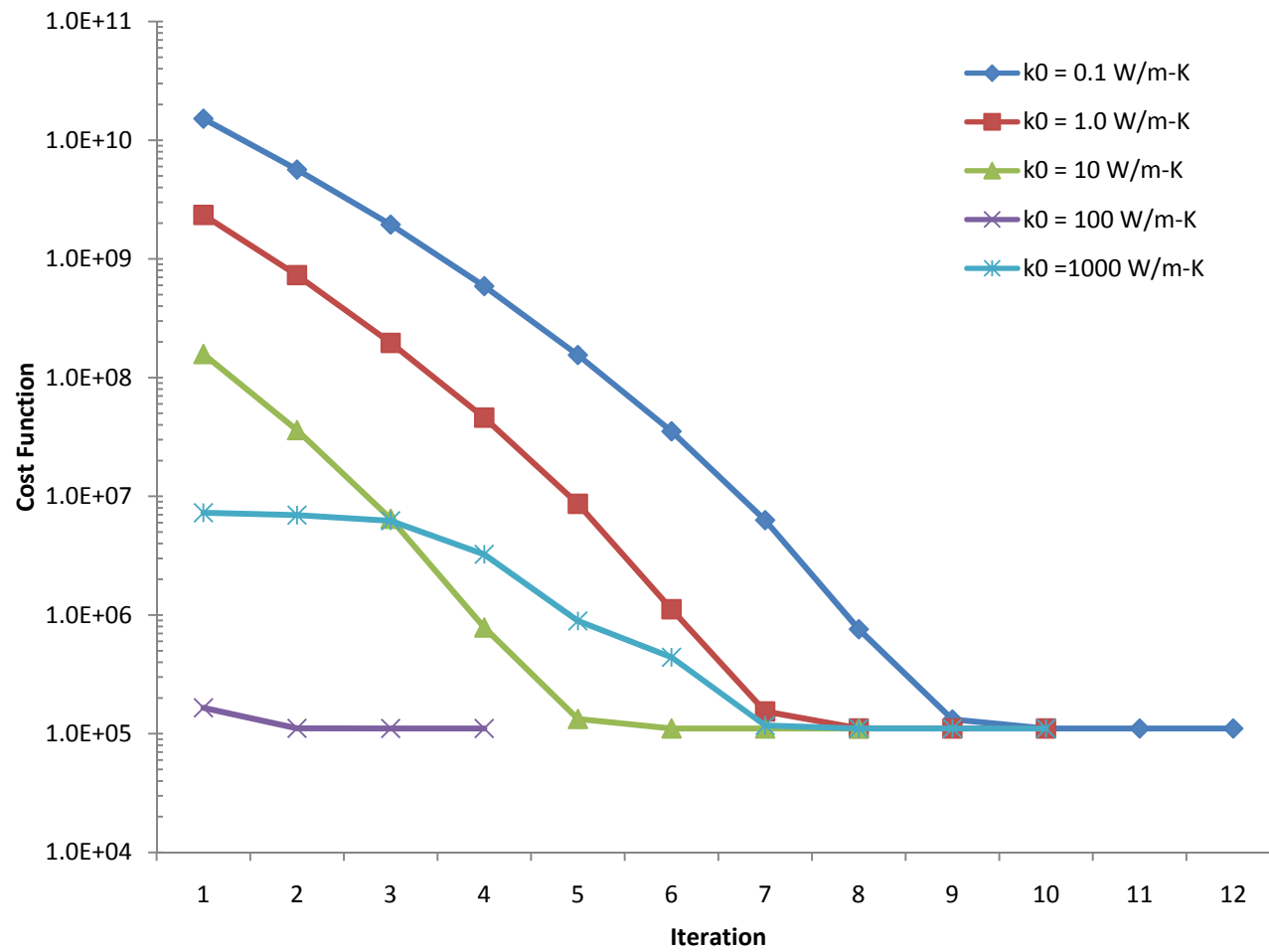


Figure 2: Cost function for estimation of SRM8421 with several initial guesses for thermal conductivity in a one-parameter (k_z) fit

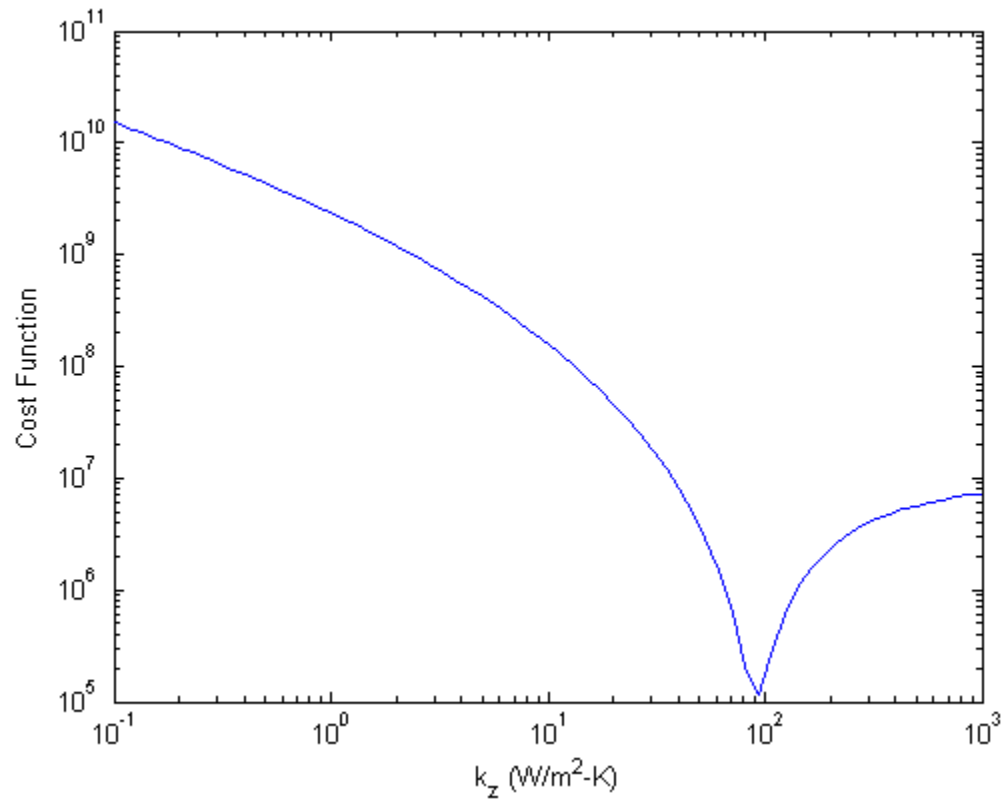


Figure 3: Evaluation of cost function at all values of thermal conductivity for SRM8421 with all other model parameters fixed.

APPENDIX I
PHOTOGRAPHS OF EXPERIMENTAL APPARATUS



Figure 1: Photograph of PDS apparatus



Figure 2: Heating beam and probe beam intersecting at sample surface

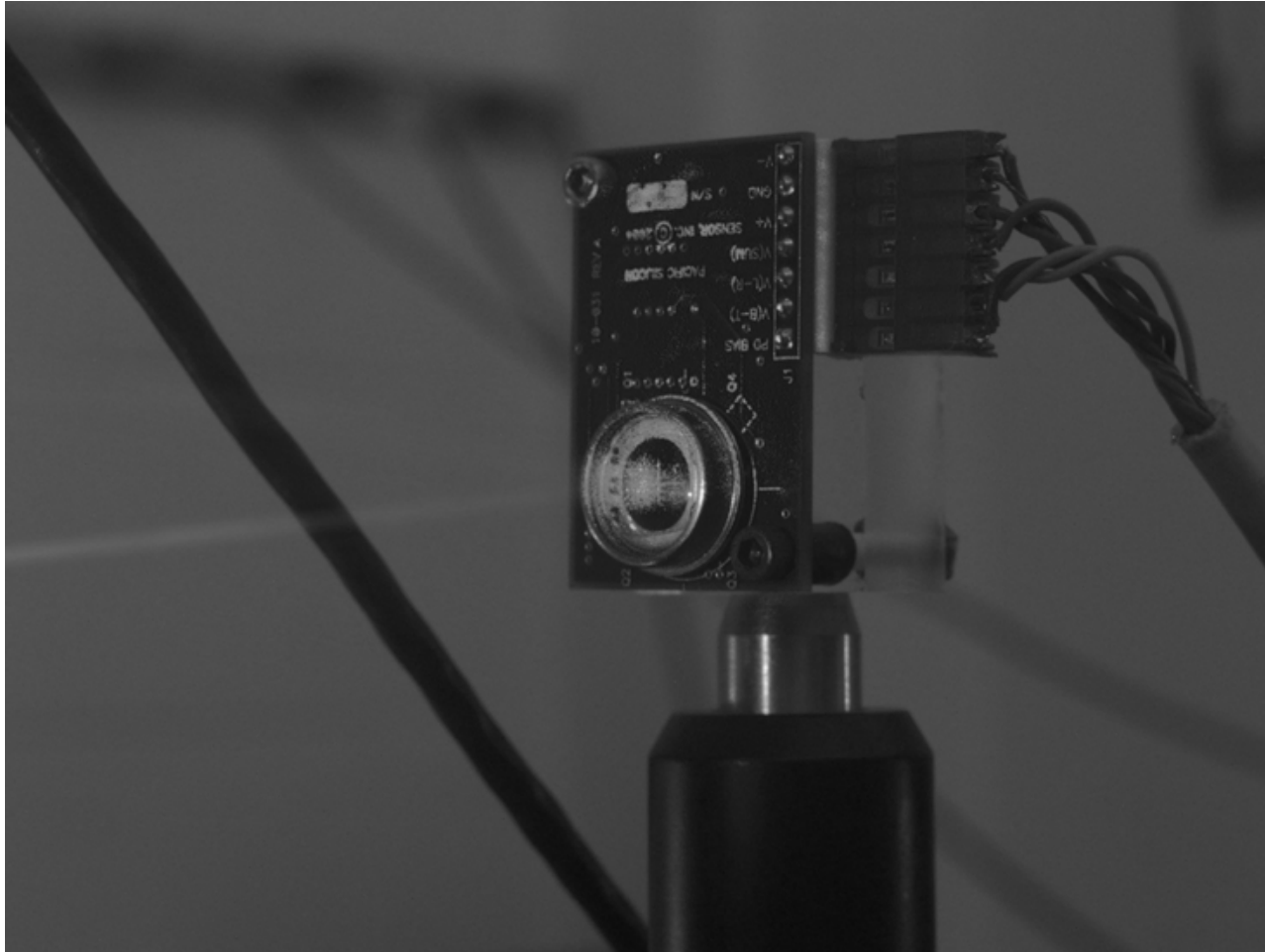


Figure 3: Probe beam striking face of quadrant photodetector

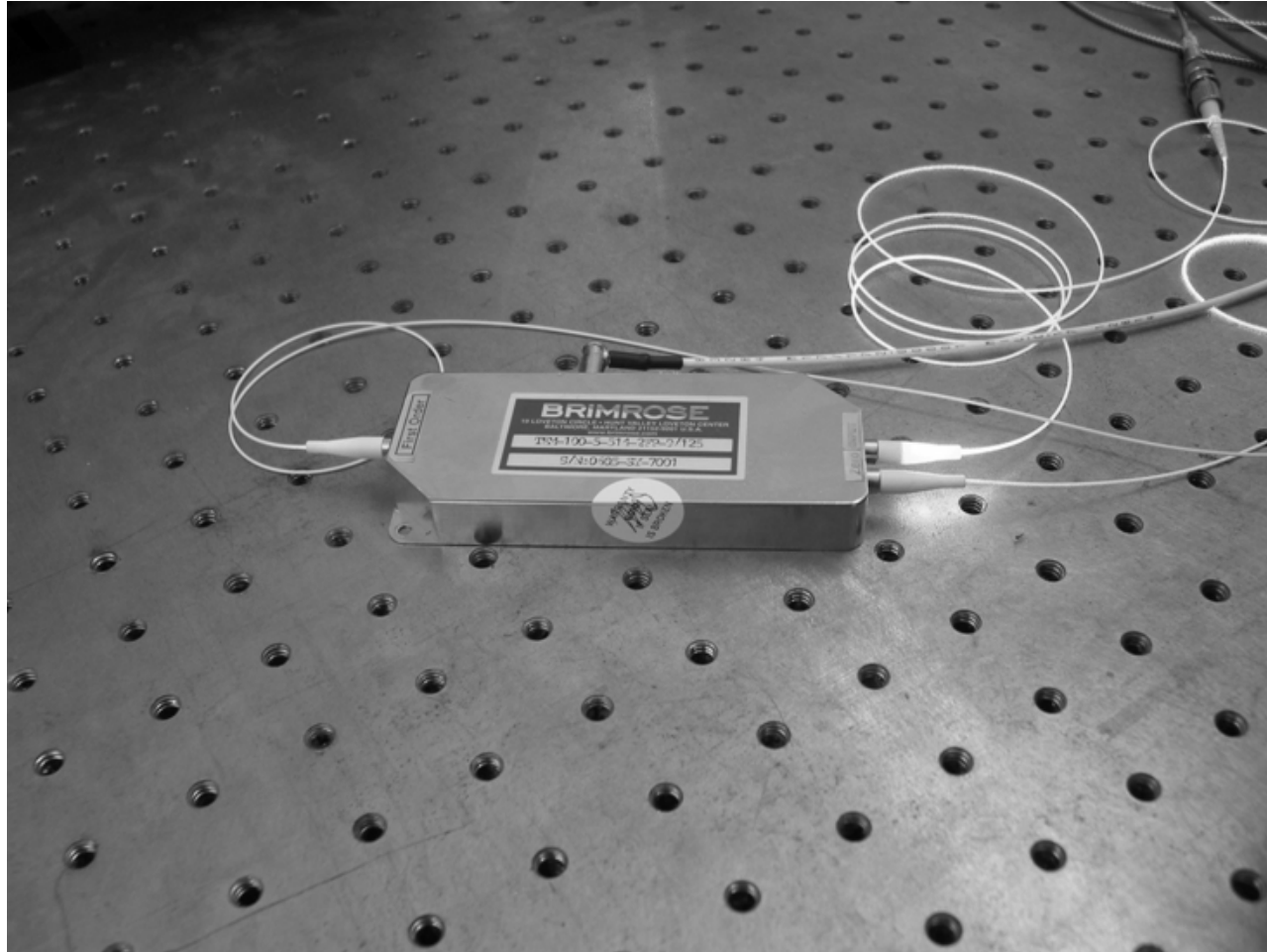


Figure 4: Brimrose acousto-optic modulator

APPENDIX J

COMPUTER CODES

(Note: The following MATLAB codes have been used by the author and are intended for informational purposes only.)

```

P0 = Ph; % Computes the optical power of the n-th harmonic of a square wave.

[Ptop,Pbot] = PDSpower(P0,Rh,refind,alpha,delta);

% Define physical/spatial frequency extent of problem

N = 1024; % Number of data points in both frequency and spatial domain. Fastest when N is a power of 2

xmax = 0.5e-3; % Maximum distance from center that signal is expected
xvec = linspace(-xmax,xmax,N+1);
xvec = xvec(1:end-1);
deltax = xvec(2)-xvec(1);

% Determine spatial circular frequency

kappamax = pi/deltax;
deltakappa = 2*kappamax/N;
kappavec = (-kappamax:deltakappa:kappamax-deltakappa);

stackedoutput = [];
stackedxvec = [];

for ii = 1:length(freqs)
    freq = freqs(ii);
    omegan = 2*pi*freq;

%     h = waitbar(0,'Calculating coefficients');

    for jj = 1:length(kappavec)

        kappa = kappavec(jj);
        lambda = sqrt(krat*kappa^2+i*omegan*rho.*Cp./kz);
        lambdaair(jj) = lambda(1);
        coeffvec(:,jj) = PDScoeff(kz,Rbdry,lambda,alpha,delta,Ptop,Pbot,Rh,kappa);
%         waitbar(jj/length(kappavec));

    end

%     close(h);

c2air = coeffvec(1,:);

zvec = linspace(0,height+2*Rp);

```

```

hinc = height;
hrefl = -height;

for zz = 1:length(zvec)

    phibarnorm(zz,:) = ifftshift(-1/n0*dndT*1/2*sqrt(2/pi)
/Rp*ifft(fftshift(lambdaair.*c2air.*...
    (exp(-lambdaair*zvec(zz)-kappavec.^2.*(Rh^2+Rp^2)/8-2*
(zvec(zz)-hinc)^2/Rp^2)-exp(-lambdaair*zvec(zz)-kappavec.^2.*
(Rh^2+Rp^2)/8-2*(zvec(zz)-hrefl)^2/Rp^2))))*(deltakappa*N/(2*pi));

    phibartan(zz,:) = ifftshift(i/n0*dndT*1/2*sqrt(2/pi)/Rp*ifft
(fftshift(kappavec.*c2air.*...
    (exp(-lambdaair*zvec(zz)-kappavec.^2.*(Rh^2+Rp^2)/8-2*
(zvec(zz)-hinc)^2/Rp^2)+exp(-lambdaair*zvec(zz)-kappavec.^2.*
(Rh^2+Rp^2)/8-2*(zvec(zz)-hrefl)^2/Rp^2))))*(deltakappa*N/(2*pi));

%       plot(kappavec,abs(phibartan));
%       pause(0.05);
end

phibarnorm = trapz(zvec,phibarnorm,1);
phibartan = trapz(zvec,phibartan,1);

%% Null phase of tangential deflections

fitresults = fit(real(phibartan(1,N/2-2:N/2+2)'),imag(phibartan
(1,N/2-2:N/2+2)'),'poly1');
ctrslope = fitresults.p1;
ctrangle = atan(ctrslope);

phibartan = phibartan*exp(i*ctrangle);
phibarnorm = phibarnorm*exp(i*ctrangle);

%%

signormRMS = gain*gmult*phibarnorm;
sigtanRMS = gain*gmult*phibartan;

% This portion of the code plots the PDS signals

% xmaxplot = 0.2e-3; % Maximum x-coordinate for plotting purposes

```

```

%
% subplot(2,2,1:2)
% plot(xvec,real(sigtanRMS),xvec,imag(sigtanRMS),xvec,real(
(signormRMS),xvec,imag(signormRMS))
% xlabel('X-Offset Position (m)')
% ylabel('Complex Signal (V_{RMS})')
% legend('\Re(V_{tan})','\Im(V_{tan})','\Re(V_{norm})','\Im(V_
{norm})')
% xlim([-xmaxplot,xmaxplot])
%
% subplot(2,2,3)
% plot(xvec,abs(sigtanRMS),xvec,abs(signormRMS))
% xlabel('X-Offset Position (m)')
% ylabel('Signal Magnitude (V_{RMS})')
% legend('|V_{tan}|','|V_{norm}|')
% xlim([-xmaxplot,xmaxplot])
%
%
% subplot(2,2,4)
% plot(xvec,angle(sigtanRMS),xvec,angle(signormRMS))
% xlabel('X-Offset Position (m)')
% ylabel('Signal Phase (Rad)')
% legend('Phase(V_{tan})','Phase(V_{norm})')

% This portion of the code prepares the results as useable output
to be
% stored in an EXCEL spreadsheet.

outputarray = [real(sigtanRMS'),imag(sigtanRMS'),abs(sigtanRMS'),
angle(sigtanRMS'),...
real(signormRMS'),imag(signormRMS'),abs(signormRMS'),angle
(signormRMS')];

xstep = 1e-6;
xvecinterp = (-xmax:xstep:xmax-xstep);

outputarray = interp1(xvec,outputarray,xvecinterp,'linear',0);

stackedoutput = [stackedoutput;outputarray];
stackedxvec = [stackedxvec;xvecinterp];

end

saveflag = 0;

if saveflag == 1;

```

```
[filename,pathname] = uiputfile('*.pds');
%   xlswrite([pathname,filename],[xvecinterp',outputarray])
   xlswrite([pathname,filename],[stackedxvec,stackedoutput]);

end
```

```
clear all; close all; clc;
format short e;

%% load data file

[filename,pathname] = uigetfile('*.*xls*', 'Please Select Data File');
datafilename = [pathname,filename];
dataarray = xlsread(datafilename,1);

%% assemble data file

dataxvec = repmat(dataarray(:,1),2,1)*10^-3;
% datavec = [dataarray(:,4);dataarray(:,5);dataarray(:,2);dataarray(:,3)];
datavec = [-dataarray(:,4);dataarray(:,5)];
noisevec = [dataarray(:,8);dataarray(:,9)];

% dataxvec = repmat(dataarray(:,1),2,1);
% datavec = [dataarray(:,2);dataarray(:,3)];
% noisevec = [dataarray(:,6);dataarray(:,7)];

%% simulate PDS signals

[filename,pathname] = uigetfile('*.*xls*', 'Select PDS Configuration File');
configfilename = [pathname,filename];

maxiterations = inputdlg('Iterations','Input number of iterations',1,{'20'});
maxiterations = str2num(maxiterations{1,1});

estarray = xlsread(configfilename,'Estimation','C7:G14');
% noiselevel = xlsread(configfilename,'Estimation','B16');
paramvec0 = estarray(:,1);
paramvec = paramvec0;
stdvec0 = estarray(:,2);
infovec0 = 1./(stdvec0).^2;
minboundvec = estarray(:,3);
maxboundvec = estarray(:,4);
minchange = estarray(:,5);

PDSconfig_excel;
PDSmodifyparameters;
PDSstackedfrequency;
modeloutput = stackedoutput;
```

```

modelxvec = repmat(stackedxvec,2,1);
% modelvec = [modeloutput(:,1);modeloutput(:,2);modeloutput(:,5);
modeloutput(:,6)];
modelvec = [modeloutput(:,1);modeloutput(:,2)];

plot(modelxvec,modelvec,dataxvec,datavec)
pause(1.0);

%% Estimation

infomat0 = diag(infovec0);
noisevec = 1./noisevec.^2;
noisemat = spdiags(noisevec,0,length(modelvec),length(modelvec));
numparams = length(paramvec0);

residualvec = datavec-modelvec;

residualvec0 = paramvec-paramvec0;

costfunc(1) = 1/2*
(residualvec'*noisemat*residualvec+residualvec0'*infomat0'*residualve
c0)

lambdalm = 1e-3; % Initialize Levenburg-Marquardt parameter
iterindex = 2;
iterflag = 0;

while iterflag == 0;

    % compute jacobian

    for kk = 1:numparams

        paramvec(:,iterindex) = paramvec(:,iterindex-1);
        paramvec(kk,iterindex) = 1.01*paramvec(kk,iterindex);

        PDSmodifyparameters;
        PDSstackedfrequency;
        perturboutput = stackedoutput;

        dmoddparam = (perturboutput-modeloutput)/(0.01*paramvec(kk,
iterindex-1));
        %          jacobian(:,kk) = [dmoddparam(:,1);dmoddparam(:,2);
dmoddparam(:,5);dmoddparam(:,6)];

```

```

        jacobian(:,kk) = [dmoddparam(:,1);dmoddparam(:,2)];

end

scalemat = diag(max(jacobian));

%     [jacobianrows,jacobiancols] = size(jacobian);
%     for ii = 1:jacobiancols
%         scalevec(ii) = norm(jacobian(:,ii));
%     end
%     scalemat = diag(scalevec);

residualvec0bar = scalemat*residualvec0;
jacobianbar = jacobian*inv(scalemat);
infomat0bar = inv(scalemat)*infomat0*inv(scalemat);
residualvec0bar = scalemat*residualvec0;

lmflag = 0;
while lmflag == 0;

%         stepvecbar = inv(jacobianbar'*noisemat*jacobianbar +
infomat0bar + lambdalm*inv(scalemat)*inv(scalemat))*...
%         (jacobianbar'*noisemat*residualvec -
infomat0bar*residualvec0);
        stepvecbar = inv(jacobianbar'*noisemat*jacobianbar +
infomat0bar + lambdalm*inv(scalemat)*inv(scalemat))*...
        (jacobianbar'*noisemat*residualvec -
infomat0bar*residualvec0bar);
        stepvec = inv(scalemat)*stepvecbar

        underminchange = abs(stepvec) < minchange;

        if sum(underminchange) == length(stepvec)
            iterflag = 1;
            lmflag = 1;
            disp('All paramters are under minimum change')
        end

        newparamvec = paramvec(:,iterindex-1) + stepvec;

        underminbound = newparamvec < minboundvec;
        underminboundindex = find(underminbound);
        newparamvec(underminboundindex) = minboundvec
(underminboundindex);

```

```

overmaxbound = newparamvec > maxboundvec;
overmaxboundindex = find(overmaxbound);
newparamvec(overmaxboundindex) = maxboundvec
(overmaxboundindex);

if sum([underminboundindex;overmaxboundindex])~=0;
    disp('One or more parameters may have hit bound')
end

paramvec(:,iterindex) = newparamvec;
PDSmodifyparameters;
PDSstackedfrequency;
modeloutput = stackedoutput;
modelxvec = repmat(stackedxvec,2,1);
%     modelvec = [modeloutput(:,1);modeloutput(:,2);
modeloutput(:,5);modeloutput(:,6)];
modelvec = [modeloutput(:,1);modeloutput(:,2)];

plot(modelxvec,modelvec,dataxvec,datavec,'r+','MarkerSize',
2);
legend('Model','Data')
title('Estimation Results')
xlabel('X-Offset (m)')
ylabel('Deflection Signal (V)')
pause(0.1)

residualvec_post = datavec-modelvec;
residualvec0_post = paramvec(:,iterindex)-paramvec0;

costfunc(iterindex) = 1/2*
(residualvec_post'*noisemat*residualvec_post+residualvec0_post'*infor
at0'*residualvec0_post);

if costfunc(iterindex) >= costfunc(iterindex-1);
    lambdalm = 10*lambdalm;
    disp(sprintf('Increasing Lambda = %0.1e',lambdalm))
    if lambdalm >= 10^100
        lmflag = 1;
        iterflag = 1;
        disp('Levenburg Marquardt unable to reduce cost
function')
    end
else if costfunc(iterindex) <= costfunc(iterindex-1);
    lambdalm = 0.1*lambdalm;
    residualvec = residualvec_post;
    residualvec0 = residualvec0_post;

```

```

                                %           lambdaalm = 1e-3;
                                %           paramvec(:,iterindex) =
newparamvec;
                                lmflag = 1;
                                iterindex = iterindex + 1;
                                end
                                end % end of checking cost function
                                end % end of the levenburg-marquardt adjustment

                                %           xlswrite(configfilename,[dataxvec,datavec,modelxvec,
modelvec],'GraphData','A3');

                                if iterindex == maxiterations;
                                    iterflag = 1;
                                end

                                disp(sprintf('Iteration number %0d',iterindex-1))
                                disp(sprintf('Cost fuction = %0.3f',costfunc(end)))
                                disp(' Parameter Step Size')
                                disp([paramvec(:,end),stepvec])

                                end % end of parameter estimation

                                %% Measures of Goodness

                                MSE = inv(scalemat)*inv
(jacobianbar'*noisemat*jacobianbar+infomat0bar)*inv(scalemat)

                                sigmaparam = sqrt(diag(MSE))

                                for ii = 1:numparams
                                    for jj = 1:numparams

                                        PDScorr(ii,jj) = MSE(ii,jj)/sqrt(MSE(ii,ii)*MSE(jj,jj));
                                    end
                                end

                                disp('Parameter Mean Standard Deviation')
                                format short e;
                                disp([paramvec(:,end),sigmaparam])
                                disp(sprintf('Cost Function = %0.4e',costfunc(end)))

                                %% File output

                                xlswrite(configfilename,MSE,'PostProcessing','B3');
                                xlswrite(configfilename,sigmaparam,'PostProcessing','B14');

```

```
xlswrite(configfilename,PDScorr,'PostProcessing','B26');  
xlswrite(configfilename,costfunc,'PostProcessing','L3');  
xlswrite(configfilename,paramvec,'PostProcessing','M3');
```

```

function [coeffvec] = PDScoeff(kz,Rbdry,lambda,alpha,delta,Ptop,Pbot,
Rh,kappa)

% This program will generate the transformed temperature coefficients
% (c1,c2) for each layer in the system.
%
% INPUTS:
% kz = vector of thermal conductivity [W/m-K]
% lambda = vector of complex t.p.d. [1/m]
% alpha = vector of optical absorption coefficient [1/m]
% delta = vector of layer thickness [m]
% Ptop = vector of optical power at top of layer [W]
% Pbot = vector of optical power at bottom of layer [W]
% Rh = 1/e^2 heating beam radius [m]
% kappa = spatial circular frequency [1/m]
%
% OUTPUTS:
% coeffvec = vector of transformed temperature coefficients of form
%           [c(2,1);c(1,2);c(2,2);...;c(1,n-1);c(2,n-1);c(1,n)]
%
warning on all

numlayers = length(kz);
coeffmat = spalloc(2*(numlayers-1),2*(numlayers-1),4);

if numlayers == 2

    coeffmat(1,1) = -kz(1)*lambda(1);
    coeffmat(1,2) = -kz(2)*lambda(2);

    coeffmat(2,1) = -Rbdry(1)*kz(1)*lambda(1)-1;
    coeffmat(2,2) = 1;

    constvec(1,1) = (alpha(2)^2/(lambda(2)^2-alpha(2)^2)*(Ptop(2))-
...
    alpha(1)^2/(lambda(1)^2-alpha(1)^2)*(-Pbot(1)))*...
    exp(-kappa^2*Rh^2/8);

    constvec(2,1) = (1/kz(1)*alpha(1)/(lambda(1)^2-alpha(1)^2)*(-Pbot
(1))-...
    1/kz(2)*alpha(2)/(lambda(2)^2-alpha(2)^2)*(Ptop(2)))*...
    exp(-kappa^2*Rh^2/8);

else

```

```

for jj = 1:numlayers-1

    if jj == 1

        coeffmat(2*jj-1,2*jj-1) = -kz(jj)*lambda(jj);
        coeffmat(2*jj-1,2*jj) = -kz(jj+1)*lambda(jj+1);
        coeffmat(2*jj-1,2*jj+1) = kz(jj+1)*lambda(jj+1)*exp(-
lambda(jj+1)*delta(jj+1));

        coeffmat(2*jj,2*jj-1) = (-Rbdry(jj)*kz(jj)*lambda(jj)-1);
        coeffmat(2*jj,2*jj) = 1;
        coeffmat(2*jj,2*jj+1) = exp(-lambda(jj+1)*delta(jj+1));

        constvec(2*jj-1,1) = (alpha(jj+1)^2/(lambda(jj+1)^2-alpha
(jj+1)^2)*...
        (Ptop(jj+1)-Pbot(jj+1)*exp(-alpha(jj+1)*delta(jj+1)))
-...
        alpha(jj)^2/(lambda(jj)^2-alpha(jj)^2)*...
        (-Pbot(jj))*...
        exp(-kappa^2*Rh^2/8);

        constvec(2*jj,1) = (1/kz(jj)*alpha(jj)/(lambda(jj)^2-
alpha(jj)^2)*...
        (1-Rbdry(jj)*kz(jj)*alpha(jj))*...
        (-Pbot(jj))-...
        1/kz(jj+1)*alpha(jj+1)/(lambda(jj+1)^2-alpha(jj+1)^2)
*...
        (Ptop(jj+1)+Pbot(jj+1)*exp(-alpha(jj+1)*delta
(jj+1))))*...
        exp(-kappa^2*Rh^2/8);

    else if jj == numlayers-1

        coeffmat(2*jj-1,2*jj-2) = kz(jj)*lambda(jj)*exp(-
lambda(jj)*delta(jj));
        coeffmat(2*jj-1,2*jj-1) = -kz(jj)*lambda(jj);
        coeffmat(2*jj-1,2*jj) = -kz(jj+1)*lambda(jj+1);

        coeffmat(2*jj,2*jj-2) = (Rbdry(jj)*kz(jj)*lambda(jj)
-1)*exp(-lambda(jj)*delta(jj));
        coeffmat(2*jj,2*jj-1) = (-Rbdry(jj)*kz(jj)*lambda(jj)
-1);

        coeffmat(2*jj,2*jj) = 1;

        constvec(2*jj-1,1) = (alpha(jj+1)^2/(lambda(jj+1)^2-

```

```

alpha(jj+1)^2)*...
    (Ptop(jj+1))-...
    alpha(jj)^2/(lambda(jj)^2-alpha(jj)^2)*...
    (Ptop(jj)*exp(-alpha(jj)*delta(jj))-Pbot(jj)))
*...
    exp(-kappa^2*Rh^2/8);

    constvec(2*jj,1) = (1/kz(jj)*alpha(jj)/(lambda(jj)^2-
alpha(jj)^2)*...
    (1-Rbdry(jj)*kz(jj)*alpha(jj))*...
    (Ptop(jj)*exp(-alpha(jj)*delta(jj))-Pbot(jj))-...
    1/kz(jj+1)*alpha(jj+1)/(lambda(jj+1)^2-alpha
(jj+1)^2)*...
    (Ptop(jj+1)))*)...
    exp(-kappa^2*Rh^2/8);

else

    coeffmat(2*jj-1,2*jj-2) = kz(jj)*lambda(jj)*exp(-
lambda(jj)*delta(jj));
    coeffmat(2*jj-1,2*jj-1) = -kz(jj)*lambda(jj);
    coeffmat(2*jj-1,2*jj) = -kz(jj+1)*lambda(jj+1);
    coeffmat(2*jj-1,2*jj+1) = kz(jj+1)*lambda(jj+1)*exp(-
lambda(jj+1)*delta(jj+1));

    coeffmat(2*jj,2*jj-2) = (Rbdry(jj)*kz(jj)*lambda(jj)
-1)*exp(-lambda(jj)*delta(jj));
    coeffmat(2*jj,2*jj-1) = (-Rbdry(jj)*kz(jj)*lambda(jj)
-1);

    coeffmat(2*jj,2*jj) = 1;
    coeffmat(2*jj,2*jj+1) = exp(-lambda(jj+1)*delta
(jj+1));

    constvec(2*jj-1,1) = (alpha(jj+1)^2/(lambda(jj+1)^2-
alpha(jj+1)^2)*...
    (Ptop(jj+1)-Pbot(jj+1)*exp(-alpha(jj+1)*delta
(jj+1)))-...
    alpha(jj)^2/(lambda(jj)^2-alpha(jj)^2)*...
    (Ptop(jj)*exp(-alpha(jj)*delta(jj))-Pbot(jj)))
*...
    exp(-kappa^2*Rh^2/8);

    constvec(2*jj,1) = (1/kz(jj)*alpha(jj)/(lambda(jj)^2-
alpha(jj)^2)*...
    (1-Rbdry(jj)*kz(jj)*alpha(jj))*...
    (Ptop(jj)*exp(-alpha(jj)*delta(jj))-Pbot(jj))-...

```

```
1/kz(jj+1)*alpha(jj+1)/(lambda(jj+1)^2-alpha
(jj+1)^2)*...
(Ptop(jj+1)+Pbot(jj+1)*exp(-alpha(jj+1)*delta
(jj+1))))*...
exp(-kappa^2*Rh^2/8);

        end
    end
end
end
```

```
coeffvec = conj(coeffmat)\constvec; % modified on 7/8/08 for
temperature field plotting
```

```
% coeffmat = conj(coeffmat);
% invcoeffmat = inv(coeffmat);
% % [lcoeffmat,ucoeffmat]=lu(coeffmat);
% % invcoeffmat = inv(ucoeffmat)*inv(lcoeffmat);
% coeffvec = invcoeffmat * constvec;
```

```

% This file allows for the modification of parameters in an
estimation
% scheme. The input is a vector of parameters that must correspond
to
% elements in the configuration file.
%
% For example: To modify the heating beam radius, element paramvec
(1) will
% be the current estimate of the radius. In the configuration file
below,
% you must enter Rh = paramvec(1) in its appropriate location.
%
% It is suggested that you comment out the original entry in the
% configuration file rather than overwriting it.

% Constants

gasprops = xlsread(configfilename,'Materials','A6:H6');
absprops = xlsread(configfilename,'Materials','A12:I12');
perprops = xlsread(configfilename,'Materials','A19:I20');
subprops = xlsread(configfilename,'Materials','A27:G27');
hbeamprops = xlsread(configfilename,'Lasers','A6:C6');
pbeamprops = xlsread(configfilename,'Lasers','A11:D11');
qpdprops = xlsread(configfilename,'Lasers','A16:C16');
freqs = xlsread(configfilename,'Lasers','A20:A30');

n0 = gasprops(5); % n of air at 20C
dndT = gasprops(8); % dn/dT for air near 20C

% Experimental Configuration

lambdah = hbeamprops(1); % Wavelength of heating beam [m]
Ph = hbeamprops(2); % Power of heating beam [W, Peak]
Rh = hbeamprops(3); % 1/e^2 radius of heating beam at z = 0 [m]

lambdap = pbeamprops(1); % Wavelength of probe beam [m]
Pp = pbeamprops(2); % Power of probe beam [W]
Rp = pbeamprops(3); % 30e-6; % 1/e^2 radius of probe beam at y = 0
[m]
height = pbeamprops(4); % Height of probe beam above sample [m]

dispgain = qpdprops(1); % I-V Gain of QPD circuitry [V/A]
lQPD = qpdprops(2); % Distance from y = 0 to QPD [m]
gain = qpdprops(3);
gmult = 1; % added here in lieu of EXCEL file

```

```

% Layer Configuration

kzair = gasprops(1); % Thermal conductivity of air in z-direction [W/m-K]
kratair = gasprops(2); % kr/kz of air
rhoair = gasprops(3); % Density of air [kg/m^3]
Cpair = gasprops(4); % Specific heat of air [J/kg-K]
refindair = gasprops(5)+i*gasprops(6); % Complex refractive index of air @ 514nm
alphaair = gasprops(7); % Absorption coefficient of air [1/m]

kzsub = subprops(1); % Thermal conductivity of substrate in z-direction [W/m-K]
kratsub = subprops(2); % kr/kz of substrate
rhosub = subprops(3); % Density of substrate [kg/m^3]
Cpsub = subprops(4); % Specific heat of substrate [J/kg-K]
refindsub = subprops(5)+i*subprops(6); % Complex refractive index of substrate @ 514nm
alphasub = subprops(7); % Absorption coefficient of air [1/m]

absflag = xlsread(configfilename,'Materials','B13'); % On/Off flag for absorbing layer
kzabs = absprops(1); % Thermal conductivity of absorbing layer in z-direction [W/m-K]
kratabs = absprops(2); % kr/kz of absorbing layer
rhoabs = absprops(3); % Density of absorbing layer [kg/m^3]
Cpabs = absprops(4); % Specific heat of absorbing layer [J/kg-K]
refindabs = absprops(5)+i*absprops(6); % Complex refractive index of substrate @ 514nm
alphaabs = absprops(7); % Absorption coefficient of absorbing layer [1/m]
deltaabs = absprops(9); % Thickness of absorbing layer [m]
Rbdryabs = absprops(8); % Thermal resistance at bottom of absorbing layer [m^2-K/W]

[numperlayers,junk] = size(perprops);
for npl = 1:numperlayers;

kzper(npl) = perprops(npl,1); % Thermal conductivity of a single period in z-direction [W/m-K]
kratper(npl) = perprops(npl,2); % kr/kz of single period
rhoaper(npl) = perprops(npl,3); % Density of single period [kg/m^3]
Cpper(npl) = perprops(npl,4); % Specific heat of single period [J/kg-K]
refindper(npl) = perprops(npl,5)+i*perprops(npl,6); % Complex refractive index of single period @ 514nm

```

```

alphaper(npl) = perprops(npl,7); % Absorption coefficient of single
period [1/m]
deltaper(npl) = perprops(npl,9); % Thickness of layers in a single
period [m]
Rbdryper(npl) = perprops(npl,8); % Thermal resistance at bottom of
layers in a single period [m^2-K/W]

end

nummer = xlsread(configfilename,'Materials','B21'); % Number of
periods in multilayer

% Assemble output arrays

if absflag == 1

    kz = [kzair,kzabs, repmat(kzper,1,numper),kzsub];
    krat = [kratair,kratabs, repmat(kratper,1,numper),kratsub];
    rho = [rhoair,rhoabs, repmat(rhoper,1,numper),rhosub];
    Cp = [Cpair,Cpabs, repmat(Cpper,1,numper),Cpsub];
    refind = [refindair,refindabs, repmat(refindper,1,numper),
refindsub];
    alpha = [alphaair,alphaabs, repmat(alphaper,1,numper),alphasub];
    Rbdry = [0,Rbdryabs, repmat(Rbdryper,1,numper),0];
    delta = [inf,deltaabs, repmat(deltaper,1,numper),inf];
    ztop = [inf,0,-cumsum(delta(2:end))];
    zbot = [0,-cumsum(delta(2:end)),-inf];

else

    kz = [kzair, repmat(kzper,1,numper),kzsub];
    krat = [kratair, repmat(kratper,1,numper),kratsub];
    rho = [rhoair, repmat(rhoper,1,numper),rhosub];
    Cp = [Cpair, repmat(Cpper,1,numper),Cpsub];
    refind = [refindair, repmat(refindper,1,numper),refindsub];
    alpha = [alphaair, repmat(alphaper,1,numper),alphasub];
    Rbdry = [0, repmat(Rbdryper,1,numper),0];
    delta = [inf, repmat(deltaper,1,numper),inf];
    ztop = [inf,0,-cumsum(delta(2:end))];
    zbot = [0,-cumsum(delta(2:end)),-inf];

end
end

```

```
% Use this template to modify PDS model parameters. For instance, in
the
% scenario below, the 3rd parameter in the parameter vector will be
the
% probe beam radius.

% kz(3) = paramvec(1,end);
% gain = paramvec(2,end);
% Rp = paramvec(3,end);
% Rbdry(3) = paramvec(4,end);
% krat(3) = paramvec(5,end);
% Rh = paramvec(6,end);
```

```
clear all;
close all;
clc;

deflvec = [];
noisevec = [];
positionvec = [];
outputarray = [];

xmin = -0.5e-3;
xmax = 0.5e-3;
deltax = 1.0e-6;
posvec = (xmin:deltax:xmax-deltax)';
posvec = posvec*10^3;

%% Load Data
%%%%%%%%%%%%%%%%%%%%%%%%%%%%%%%%%%%%%%%%%%%%%%%%%%%%%%%%%%%%%%%%%%%%%%%%
% Load data files and extract data %
%%%%%%%%%%%%%%%%%%%%%%%%%%%%%%%%%%%%%%%%%%%%%%%%%%%%%%%%%%%%%%%%%%%%%%%%

[filename,pathname]=uigetfile('Please choose data file to
condition');
filename = strcat(pathname,filename);

PDSdata = xlsread(filename,-1);
xpos = PDSdata(:,2);

%% Find copies of x
%%%%%%%%%%%%%%%%%%%%%%%%%%%%%%%%%%%%%%%%%%%%%%%%%%%%%%%%%%%%%%%%%%%%%%%%
% Find non-distinct values of x (copies) %
%%%%%%%%%%%%%%%%%%%%%%%%%%%%%%%%%%%%%%%%%%%%%%%%%%%%%%%%%%%%%%%%%%%%%%%%

delx = diff(xpos);
uniquevals = find(delx ~= 0);

xpos = PDSdata(uniquevals,2);
ypos = PDSdata(uniquevals,3);
zpos = PDSdata(uniquevals,1);
renorm = PDSdata(uniquevals,6);
imnorm = PDSdata(uniquevals,7);
retan = PDSdata(uniquevals,4);
imtan = PDSdata(uniquevals,5);

%% Find dropped points
%%%%%%%%%%%%%%%%%%%%%%%%%%%%%%%%%%%%%%%%%%%%%%%%%%%%%%%%%%%%%%%%%%%%%%%%
% Find dropped (=0) data points (copies) %
```

```

%%%%%%%%%%%%%%%%%%%%%%%%%%%%%%%%%%%%%%%%%%%%%%%%%%%%%%%%%%%%%%%%%%%%%%%%
[droprow,dropcol] = find([renorm,imnorm,retan,imtan]==0);
droprow = unique(droprow);
[xpos,ps] = removerows(xpos,droprow);
[ypos,ps] = removerows(ypos,droprow);
[zpos,ps] = removerows(zpos,droprow);
[renorm,ps] = removerows(renorm,droprow);
[imnorm,ps] = removerows(imnorm,droprow);
[retan,ps] = removerows(retan,droprow);
[imtan,ps] = removerows(imtan,droprow);

%% Plot Raw Data
%%%%%%%%%%%%%%%%%%%%%%%%%%%%%%%%%%%%%%%%%%%%%%%%%%%%%%%%%%%%%%%%%%%%%%%%
% Plot raw data %
%%%%%%%%%%%%%%%%%%%%%%%%%%%%%%%%%%%%%%%%%%%%%%%%%%%%%%%%%%%%%%%%%%%%%%%%

figure(1)
plot(xpos,abs(renorm+i*imnorm),xpos,abs(retan+i*imtan))
title('Experimental PDS Data')
xlabel('X-Offset Position [m]')
ylabel('Deflection Signal [V]')
legend('| \Phi_{norm} |', '| \Phi_{tan} |')
xlim([xpos(1),xpos(end)]);

%% Subtract Mean
%%%%%%%%%%%%%%%%%%%%%%%%%%%%%%%%%%%%%%%%%%%%%%%%%%%%%%%%%%%%%%%%%%%%%%%%
% Subtract offset voltages and estimate noise %
%%%%%%%%%%%%%%%%%%%%%%%%%%%%%%%%%%%%%%%%%%%%%%%%%%%%%%%%%%%%%%%%%%%%%%%%

waitforbuttonpress;
point1=get(gca,'CurrentPoint');
rbbox;
point2=get(gca,'CurrentPoint');

offsetind = find(xpos>=point1(1) & xpos<=point2(1));

retan_offset = mean(retan(offsetind));
retan_noise = std(retan(offsetind));

imtan_offset = mean(imtan(offsetind));
imtan_noise = std(imtan(offsetind));

renorm_offset = mean(renorm(offsetind));
renorm_noise = std(renorm(offsetind));

```

```

imnorm_offset = mean(imnorm(offsetind));
imnorm_noise = std(imnorm(offsetind));

% numendpts = 250;
%
% retan_offset = mean([retan(1:numendpts);retan(end-numendpts:end)]);
% retan_noise = std([retan(1:numendpts);retan(end-numendpts:end)]);
%
% imtan_offset = mean([imtan(1:numendpts);imtan(end-numendpts:end)]);
% imtan_noise = std([imtan(1:numendpts);imtan(end-numendpts:end)]);
%
% renorm_offset = mean([renorm(1:numendpts);renorm(end-numendpts:
end)]);
% renorm_noise = std([renorm(1:numendpts);renorm(end-numendpts:
end)]);
%
% imnorm_offset = mean([imnorm(1:numendpts);imnorm(end-numendpts:
end)]);
% imnorm_noise = std([imnorm(1:numendpts);imnorm(end-numendpts:
end)]);

%%%%%%%%%%%%%%%%%%%%%%%%%%%%%%%%%%%%%%%%%%%%%%%%%%%%%%%%%%%%%%%%%%%%%%%%
% Subtract offset voltages
%%%%%%%%%%%%%%%%%%%%%%%%%%%%%%%%%%%%%%%%%%%%%%%%%%%%%%%%%%%%%%%%%%%%%%%%

retan = retan-retan_offset;
imtan = imtan-imtan_offset;
renorm = renorm-renorm_offset;
imnorm = imnorm-imnorm_offset;

%%%%%%%%%%%%%%%%%%%%%%%%%%%%%%%%%%%%%%%%%%%%%%%%%%%%%%%%%%%%%%%%%%%%%%%%
% Plot data with offset subtracted
%%%%%%%%%%%%%%%%%%%%%%%%%%%%%%%%%%%%%%%%%%%%%%%%%%%%%%%%%%%%%%%%%%%%%%%%

figure(1)
plot(xpos,abs(renorm+i*imnorm),xpos,abs(retan+i*imtan))
title('Offsets Removed')
xlabel('X-Offset Position [m]')
ylabel('Deflection Signal [V]')
legend('| \Phi_{norm} |', '| \Phi_{tan} |')
xlim([xpos(1),xpos(end)]);

%% Rotate QPD Coordinates
%%%%%%%%%%%%%%%%%%%%%%%%%%%%%%%%%%%%%%%%%%%%%%%%%%%%%%%%%%%%%%%%%%%%%%%%
% Rotate photodetector to properly separate norm/tan channels %
%%%%%%%%%%%%%%%%%%%%%%%%%%%%%%%%%%%%%%%%%%%%%%%%%%%%%%%%%%%%%%%%%%%%%%%%

```

```

index = 1;

recompdefl = retan + i*renorm;
imcompdefl = imtan + i*imnorm;

ctrindex = 1250;

for thetadeg = -15:0.5:15

    thetarad(index) = thetadeg*pi/180;

    recompdeflrot = recompdefl*exp(i*thetarad(index));
    imcompdeflrot = imcompdefl*exp(i*thetarad(index));

    magtandeflrot = (real(recompdeflrot).^2+real(imcompdeflrot).^2).^(1/2);
    magnormdeflrot = (imag(recompdeflrot).^2+imag(imcompdeflrot).^2).^(1/2);

    [leftmax,leftmaxpos] = max(magtandeflrot(1:ctrindex));
    [rightmax,rightmaxpos] = max(magtandeflrot(ctrindex:end));
    deltasig(index) = rightmax-leftmax;

    norm_magnormdefl(index) = norm(magnormdeflrot);

    plot(xpos,magtandeflrot,xpos,magnormdeflrot)
    legend(sprintf('Angle = %0.2f',thetadeg))
    pause(0.1);

    index = index+1;
end

plot(thetarad*180/pi,deltasig,'o')
pause;

% rotationline = polyfit(thetarad,deltasig,1);
% alignangle = roots(rotationline);

[min_norm,min_index] = min(norm_magnormdefl);
alignangle = thetarad(min_index);

recompdeflrot = recompdefl*exp(i*alignangle);
imcompdeflrot = imcompdefl*exp(i*alignangle);

retan = real(recompdeflrot);

```

```

imtan = real(imcompdeflrot);
renorm = imag(recompdeflrot);
imnorm = imag(imcompdeflrot);

%% Determine x-offset
%%%%%%%%%%%%%%%%%%%%%%%%%%%%%%%%%%%%%%%%%%%%%%%%%%%%%%%%%%%%%%%%%%%%%%%%
% Determine X-Offset %
%%%%%%%%%%%%%%%%%%%%%%%%%%%%%%%%%%%%%%%%%%%%%%%%%%%%%%%%%%%%%%%%%%%%%%%%

figure(2)
plot(xpos,retan,'*','MarkerSize',3)
xlim([-0.1,0.1])
title('Box central points to determine x-offset')
waitforbuttonpress;
point1=get(gca,'CurrentPoint');
rbbox;
point2=get(gca,'CurrentPoint');
outliers = excludedata(xpos,retan,'box',[point1(1) point2(1) point1(2) point2(2)]);
opts = fitoptions('Exclude',outliers);
fitresult = fit(xpos,retan,'polyl1',opts);
xoffset = -fitresult.p2/fitresult.p1;

xpos = xpos - xoffset;

%% Interpolate positions
%%%%%%%%%%%%%%%%%%%%%%%%%%%%%%%%%%%%%%%%%%%%%%%%%%%%%%%%%%%%%%%%%%%%%%%%
% Interpolate points to desired x-positions %
%%%%%%%%%%%%%%%%%%%%%%%%%%%%%%%%%%%%%%%%%%%%%%%%%%%%%%%%%%%%%%%%%%%%%%%%

retan = interp1(xpos,retan,posvec,'cubic',0);
imtan = interp1(xpos,imtan,posvec,'cubic',0);
renorm = interp1(xpos,renorm,posvec,'cubic',0);
imnorm = interp1(xpos,imnorm,posvec,'cubic',0);

%% Null tangential
%%%%%%%%%%%%%%%%%%%%%%%%%%%%%%%%%%%%%%%%%%%%%%%%%%%%%%%%%%%%%%%%%%%%%%%%
% Null phase of tangential channel %
%%%%%%%%%%%%%%%%%%%%%%%%%%%%%%%%%%%%%%%%%%%%%%%%%%%%%%%%%%%%%%%%%%%%%%%%
figure(2)
plot(posvec,[retan,imtan],'*','MarkerSize',3)
xlim([-0.1,0.1])
title('Identify linear points near center')

waitforbuttonpress;
point1=get(gca,'CurrentPoint');
```

```

rbbbox;
point2=get(gca,'CurrentPoint');
outliers = excludedata(posvec,retan,'box',[point1(1) point2(1) point1(2) point2(2)]);
opts = fitoptions('Exclude',outliers);
fitresult = fit(retan,imtan,'poly1',opts);
ctrslope = fitresult.p1;
ctrangle = atan(ctrslope);

% ctrangle = 0; % this was added to remove nullification

phitan = (retan + i*imtan)*exp(-i*ctrangle);
phinorm = (renorm + i*imnorm)*(-i*ctrangle);

figure(3)
plot(phitan,'r*','MarkerSize',3)
title('Phase Space Deflections')
xlabel('\Re(\Phi_{tan})')
ylabel('\Im(\Phi_{tan})')
legend('Original','Rotated')

retan = real(phitan);
imtan = imag(phitan);
renorm = real(phinorm);
imnorm = imag(phinorm);

figure(4)
plot(posvec,abs(renorm+i*imnorm),posvec,abs(retan+i*imtan))
title('Conditioned PDS Data Set')
xlabel('X-Offset Position [m]')
ylabel('Deflection Signal [V]')
legend('| \Phi_{norm} |', '| \Phi_{tan} |')

figure(5)
plot(posvec,renorm,'b*',posvec,imnorm,'ro',posvec,retan,'gs',posvec,imtan,'kd','MarkerSize',3)
title('Conditioned PDS Data Set')
xlabel('X-Offset Position [m]')
ylabel('Deflection Signal [V]')
legend('\Re(\Phi_{norm})','\Im(\Phi_{norm})','\Re(\Phi_{tan})','\Im(\Phi_{tan})')

revnormbut = questdlg('Reverse phase of normal channel?','Normal Channel','No')

if strcmp(revnormbut,'Yes')==1

```

```

        renorm = -renorm;
        imnorm = -imnorm;
    end

    revtanbut = questdlg('Reverse phase of tangential
channel?', 'Tangential Channel', 'No');

    if strcmp(revtanbut, 'Yes')==1
        retan = -retan;
        imtan = -imtan;
    end

    close all;

    figure(5)
    plot(posvec, renorm, 'b*', posvec, imnorm, 'ro', posvec, retan, 'gs', posvec,
    imtan, 'kd', 'MarkerSize', 3)
    title('Conditioned PDS Data Set')
    xlabel('X-Offset Position [m]')
    ylabel('Deflection Signal [V]')
    legend('\Re(\Phi_{norm})', '\Im(\Phi_{norm})', '\Re(\Phi_{tan})', '\Im
(\Phi_{tan})')

    deflarray = [renorm, imnorm, retan, imtan];

    noisearray = [repmat(renorm_noise, length(posvec), 1), ...
        repmat(imnorm_noise, length(posvec), 1), ...
        repmat(retan_noise, length(posvec), 1), ...
        repmat(imtan_noise, length(posvec), 1)];

    % ypos = repmat(ypos(1), size(posvec));
    % zpos = repmat(zpos(1), size(posvec));

    %% File output

    outputarray = [posvec, deflarray, noisearray];

    [savefilename, savepathname] = uiputfile('Save conditioned data as');
    savefilename = strcat(savepathname, savefilename);
    xlswrite(savefilename, outputarray)
    % fid = fopen(savefilename, 'w');
    % fprintf(fid, '%0.6e\t%0.6e\t%0.6e\t%0.6e\t%0.6e\t%0.6e\t%0.6e\t%0.6e\t%0.6e\t%0.6e\n', outputarray');
    % fclose(fid);

```

	A	B	C	D	E	F	G	H	I
1	Material Property Datasheet								
2									
3	Gas Properties								
4	k_z	k_r/k_z	ρ	C_p	n	k	α	dn/dT	
5	W/m ² -K		kg/m ³	J/kg-K			m ⁻¹	K ⁻¹	
6	0.02588	1	1.164	1007	1	0	0.00E+00	-9.13E-07	
7									
8									
9	Absorbing Layer Properties								
10	k_z	k_r/k_z	ρ	C_p	n	k	α	R_{bdry}	δ
11	W/m ² -K		kg/m ³	J/kg-K			m ⁻¹	m ² -K/W	m
12	174	1	19300	132	3.38	2.68	6.55E+07	0	1.10E-07
13	Use absorpt	1							
14									
15									
16	Multilayer Properties								
17	k_z	k_r/k_z	ρ	C_p	n	k	α	R_{bdry}	δ
18	W/m ² -K		kg/m ³	J/kg-K			m ⁻¹	m ² -K/W	m
19	148	1	2330	712	1	0	0.00E+00	1.00E+00	2.29E-04
20									
21	Number of	1							
22									
23									
24	Substrate Properties								
25	k_z	k_r/k_z	ρ	C_p	n	k	α		
26	W/m ² -K		kg/m ³	J/kg-K			m ⁻¹		
27	148	1	2330	712	1	0	0.00E+00		

	A	B	C	D	E
1	<u>Optical Setup</u>				
2					
3	Heating Beam				
4	λ_h	P_h	R_h		
5	m	W	m		
6	5.15E-07	0.05	4.50E-06		
7					
8	Probe Beam				
9	λ_p	P_p	$R_p(y=0)$	height	
10	m	W	m	m	
11	6.33E-07	0.0008	2.39E-05	0	
12					
13	Quadrant Photodiode				
14	Disp Gain	I_{QPD}	Total Gain		
15	V/m	m	V/rad		
16	1000.4	1.80E-01	1.80E+02		
17					
18	Frequency				
19	Hz				
20	1000				
21	2000				
22	4000				
23	8000				
24	16000				
25	32000				
26	64000				
27	128000				
28					
29					

	A	B	C	D	E	F	G	H
1	Estimation Setup							
2								
3	Estimation Parameters							
4								
5			a priori distribution		bounds		min change	
6	Parameter #	Description	μ_0	σ_0	Min	Max		
7	1	kz	9.98E+01	1.00E+307	0.01	10000	1.00E-03	
8	2	gain	1.80E+02	1.00E+307	1.00E+00	1.00E+04	1.00E-03	
9	3	Rp	2.39E-05	2.39E-06	1.00E-06	1.00E-03	1.00E-09	
10	4	Cp	7.12E+02	7.12E+01	1.00E+02	1.00E+04	1.00E-03	
11	5							
12	6							
13	7							
14	8							
15								
16	noiselevel	5.00E-06 V						
17								
18								
19	note: inf is 1e307							
20								
21								
22								
23								
24								
25								
26								
27								
28								